Technical Report
TR-18-01
April 2018

Key master variables affecting the mobility of Ni, Pu, Tc and U in the near field of the SFR repository

Main experimental findings and PA implications of the PhD thesis

Jordi Bruno
Maria Rosa González-Siso
Lara Duro
Xavier Gaona
Marcus Altmaier

SVENSK KÄRNBRÄNSLEHANTERING AB

SWEDISH NUCLEAR FUEL
AND WASTE MANAGEMENT CO

Box 3091, SE-169 03 Solna
Phone +46 8 459 84 00
skb.se

SVENSK KÄRNBRÄNSLEHANTERING

ISSN 1404-0344
SKB TR-18-01
ID 1615504
April 2018

Key master variables affecting the mobility of Ni, Pu, Tc and U in the near field of the SFR repository

Main experimental findings and PA implications of the PhD thesis

Jordi Bruno, Maria Rosa González-Siso, Lara Duro
Amphos[21] Consulting S.L.

Xavier Gaona, Marcus Altmaier
Karlsruhe Insitute of Technology (KIT-INE)

Keywords: Nickel, Sorption, Redox, Iron, Magnetite.

Abstract

In the last five years, we have been investigating a number of key processes controlling the mobility and fate of Ni, a critical radionuclide in the near-field of the SFR repository. In addition, we have performed some studies concerning the interaction of U, Pu and Tc with the products of the anaerobic corrosion of iron under various reducing conditions. The work has been performed as a PhD thesis of Maria Rosa González-Siso and in close collaboration with KIT-INE.

The objective of this PhD thesis has been the experimental determination as well as the thermodynamic modelling of these key processes for the evolution of the near field of the SFR repository.

Namely:

1. To investigate the thermodynamics of the Fe(II) / Fe_3O_4(cr) redox system and to determine the solubility equilibria of Fe_3O_4(cr) under high pH and strongly reducing conditions.
2. To study the effect of these redox conditions on the redox state and mobility of key redox sensitive radionuclides like Pu, U and Tc.
3. To determine the solubility of Ni(II) under the alkaline/reducing conditions imposed by the magnetite/Fe(II), including the effect of isocarboxilic acid (ISA) a key product of the cellulose degradation under alkaline/reducing conditions.
4. To determine the sorption processes of Ni(II) on cement, in the presence of ISA and under the alkaline/reducing conditions of the system.

The outcomes of this thesis for the Safety Assessment of the SFR repository are presented and discussed. These are namelly:

- The predicted redox evolution of the near field of the repository due to the anaerobic corrosion of the steel components as documented in Duro et al. (2014) has been confirmed by the experimental data collected in the pH, Eh space of concern.
- In the presence of magnetite and Fe(II) the Eh values obtained in the pH range of interest (10–13) are in the order of −600 mV and the Fe(II) data in this range is well represented by the equilibrium solubility of Fe_3O_4(cr).
- The value of the solubility constant of magnetite derived in the present study from solubility experiments at $T = 22$ °C is significantly higher than values available in current thermodynamic databases, derived from high-temperature thermochemical studies and they should give a more realistic representation of the behaviour of magnetite under SFR conditions.
- The pH and Eh space imposed by the anaerobic corrosion of iron in the presence of cement controls the redox state and solubility of key radionuclides as U, Pu and Tc. The extent of the electron-transfer reactions and the resulting radionuclide solubility depends very much on the alkalinity of the system.
- In the presence of magnetite and under slightly alkaline conditions (pH around 8) most of the radionuclide concentrations are under 10^{-8} molar, except in the case of Pu. In this case the presence of Pu(III) enhances the concentration up to 10^{-6} molar.
- At the alkaline conditions expected in the cementitious repository, pH=12.8, only Pu concentrations are below 10^{-8} molar. Aqueous Tc(IV), although apparently reduced, is stabilised due to the formation of Tc(IV) anionic hydroxo species and the measured concentrations are in the 10^{-6} molar range. Uranium(VI) is not reduced by magnetite at pH=12.8 and the resulting concentrations are in the 10^{-5} molar range.
- All these observations would indicate that kinetics of these redox reactions would be relatively slow, particularly at higher pH values. As we already indicated in Bruno (1997) the characteristic reaction times for such multielectron transfer processes are in the range of 10 to 1 000 years, which have to be compared to the expected groundwater residence times in the SFR repository which are in the range of thousands of years. Kinetic modelling is underway to pinpoint these important issues in order to quantification QUANTIFY these processes under SFR conditions.

- Concerning the speciation and mobility of Ni(II) under SFR conditions, these are the main PA implications:
  - The solubility constant for β-$Ni(OH)_2$(s) has been determined to be log $K°_{s,0}$ = 12.10 ± 0.11.
  - The main hydrolysis equilibria have been established, the main hydrolysis species under SFR conditions is $Ni(OH)_2$(aq) with a formation constant log β_{11}= −19.7 ± 0.04. There is no evidence for the formation of anionic hydroxo species up to pH=13.
  - Under the presence of ISA the following species and equilibrium constants have been determined.
    - Ni(OH)ISA (aq) with log β_{111}= −6.5 ± 0.3,
    - $Ni(OH)_2ISA^-$ with log β_{121}= −17.6 ± 0.5,
    - $Ni(OH)_3ISA^{2-}$ with log β_{131}= −31.0 ± 0.7.
- Concerning the sorption of Ni(II) in the presence of cement and ISA these are the main implications:
  - The sorption of ^{63}Ni onto the cement is clearly reduced in the presence of ISA, in spite of the fact that there is a sizeable amount of ^{58}Ni both in the cement and the contacting water.
  - There seems to be no kinetic effect of the order of addition of the various components: cement, Ni(II) and ISA on the $^*R_d$. Only at very high ISA levels (0.1 M) there seems to be some kinetic effect but the data are not sufficient to discern the extent.
  - Detailed modelling work has resulted on a thermodynamic model to account for the effect of ISA on the sorption of ^{63}Ni onto cement. The dependence of the $^*R_d$ of ^{63}Ni onto cement in the presence of background amounts of ^{58}Ni and ISA has been calculated and the subsequent *SRF's have been established based upon the aqueous themodynamic model determined in this work. *SRF values range from 2 to 40 in the ISA concentration range: 10^{-3} to 10^{-1} M
  - The speciation scheme of Ni(II) in the presence of ISA proposed in this work explains the decrease of the extent of sorption of Ni(II) onto cement and in the presence of ISA. Independent sorption data can also be reasonably explained by the present Ni(II)-ISA-cement speciation scheme. This gives additional confidence on the results obtained.

Sammanfattning

Under de senaste fem åren har vi undersökt ett antal viktiga processer som påverkar uttransporten av Ni, en kritisk radionuklid för SFR-förvaret. Dessutom har vi utfört studier angående interaktionen mellan U, Pu och Tc med korrosionsprodukter från anaerob korrosion av järn under olika reducerande förhållanden. Arbetet har utförts som ett doktorsarbete av Maria Rosa González-Siso i nära samarbete med KIT-INE.

Syftet har varit att genom experimentella studier och termodynamisk modellering bestämma hur olika processer påverkar uttransporten av radionuklider i SFR-förvaret.

Nämligen:

1. Att undersöka termodynamiken för Fe(II)/Fe_3O_4(cr) redoxsystemet och därigenom bestämma löslighetsjämviktema av Fe_3O_4(cr) under högt pH och kraftigt reducerande förhållanden.
2. Att studera effekten av dessa redox-förhållanden på oxidationstillståndet och rörligheten för viktiga redox-känsliga radionuklider som Pu, U och Tc.
3. Att bestämma lösligheten av Ni(II) under alkaliska och de reducerande förhållanden som uppstår i närvaro av magnetit/Fe(II). I denna miljö inkludera effekten av isosackarinsyra (ISA), en produkt av cellulosanedbrytning under alkaliska förhållanden.
4. Att bestämma sorptionsprocesserna av Ni(II) på cement, i närvaro av ISA, under alkaliska och reducerande förhållanden.

För redox-betingelserna, oxidationstillståndet och lösligheten är de viktigaste slutsatserna från studierna följande:

- Den förutsagda redox-utvecklingen i närzonen som följd av korrosion av stålkomponenter vilket presenteras i Duro et al. (2014) har bekräftats med experimentella data inom det pH-, Eh-område som förväntas råda.
- I närvaro av magnetit och Fe(II) erhålls Eh-värden runt −600 mV inom det studerade pH intervallet (10–13). Den erhållna datan för Fe(II) i detta intervall representeras väl av löslighetsjämvikten för Fe_3O_4(cr).
- Värdet på löslighetskonstanten för magnetit som erhållits från denna studie via löslighetsbestämningar vid 22 °C är mycket högre än de värden som återfinns i termodynamiska databaser, termodynamiska experiment vid hög temperatur. De nu erhållna resultaten representerar de förhållanden som förväntas råda i SFR-förvaret på ett mer realistiskt vis.
- De pH och Eh betingelser som råder i förvaret kontrollerar redoxtillståndet och lösligheten hos viktiga radionuklider som U, Pu och Tc. Omfattningen av redoxreaktioner och lösligheten av radionukliderna beror väsentligt på systemets alkalitet.
- I närvaro av magnetit och förhöjt pH (pH runt 8) blir koncentrationen av radionuklider i vattenfasen under 10^{-8} molar, förutom för Pu. För Pu bidrar Pu(III) specier till ökad löslighet och lösligheten blir 10^{-6} molar
- Vid de alkaliska betingelser (pH=12,8) som råder i närvaro av cementmineraler är koncentrationen av Pu i vattenfasen under 10^{-8} molar. Löst Tc(IV), i reducerad form, stabiliseras på grund av anjoniska Tc(IV) hydroxispecier och den uppmätta koncentrationen i vattenfasen är runt 10^{-6} molar. Uran(VI) reduceras inte i närvaro av magnetit vid pH=12,8 vilket medför koncentrationer runt 10^{-5} molar i vattenfasen.
- Alla dessa observationer indikerar att kinetiken av redoxreaktionerna är relativt långsam, speciellt vid högre pH, som redan beskrivits i Bruno (1997). Karakteristiska reaktionstider för multielektronöverföringsprocesser är i storleksordningen 10 till 1 000 år. Detta ska jämföras med grundvattenomsättningestiderna i SFR vilka är i storleksordningen 1 000-tals år. För närvarande pågår modelleringsarbete där kinetiken inkluderas. Syftet med dessa modelleringar är att undersöka kinetikens betydelse för de processer som pågår i SFR efter förslutning.

- För specieringen och lösligheten av Ni(II) i närvaro av ISA är det viktigaste slutsatserna från studierna följande:
  - Löslighetskonstanten för β-$Ni(OH)_2$(s) har bestämts till $K°_{s,0} = 12.10 \pm 0.11$.
  - Den huvudsakliga hydrolysjämvikten har bestämts till att vara Ni(OH)2(aq) med en bildningskonstant på log b11= −19.7 ± 0.04. Det finns inga bevis för bildningen av anjoniska hydroxispecier vid pH upp till 13.
  - I närvaro av ISA har följande specier och jämviktskonstanter bestämts
    - Ni(OH)ISA (aq) med log $\beta_{111} = -6.5 \pm 0.3$,
    - $Ni(OH)_2ISA^-$ med log $\beta_{121} = -17.6 \pm 0.5$,
    - $Ni(OH)_3ISA^{2-}$ med log $\beta_{131} = -31.0 \pm 0.7$.
- För sorptionen av Ni(II) i närvaro av cement och ISA är de viktigaste följderna för säkerhetsanalysen:
  - Sorptionen av ^{63}Ni på cement reduceras i närvaro av ISA, trots att det finns betydande mängder ^{58}Ni både i cementen och i vattenfasen.
  - Det verkar inte finnas någon kinetisk effekt på grund av tillsatsorningen av de olika komponenterna: cement, Ni(II) och ISA på $^*R_d$. Bara vid väldigt höga ISA koncentrationer (0,1 M) verkar det finnas en kinetisk effekt. Tillräckligt med data finns inte för att utröna omfattningen.
  - Utförda modelleringar har resulterat i en termodynamisk modell. Modellen kan beskriva effekterna på ^{63}Ni sorption på cement i närvaro av ISA. Sorptionspåverkan i närvaro av bakgrundmängder utav ^{58}Ni och ISA, har beräknats och resulterat i *SRFer baserade på den framtagna modellen. Föreslagna SRFer sträcker sig mellan 2 till 40 för ISA koncentrationer mellan 10^{-3} till 10^{-1} M beräknat med data erhållna från denna studie.
  - Den föreslagna specieringen av Ni(II) i närvaro av ISA förklarar sorptionsminskningen av Ni(II) på cement. Oberoende sorptionsdata kan också på ett rimligt sätt förklaras med den föreslagna Ni(II)-ISA-cement specieringen vilket ger ytterligare förtroende för de erhållna resultaten.

Contents

1 Introduction

Low and intermediate nuclear waste from power production is mainly contained in iron and steel containers imbedded in cement and/or steel parts directly imbedded in cement. In the case of the SFR repositories located at Forsmark, they are placed in caverns and in one silo under the Baltic sea at some 60-100 metres depth in the rock. For a complete description of the repository system and their expected properties at closure the reader is referred for instance to the Engineered Barrier Process Report of the Safety Assessment PSU (SKB-TR-14). The overall result of this is that any potential groundwater intrusion in the repository will interact with the cement materials as well as the steel parts and the steel containers and this has clear implications in defining the master variables of the system and consequently the behaviour of key radionuclides potentially being released from the waste containers.

There have been a number of model studies which have helped to develop an understanding of the chemical evolution in the SFR repository due to concrete degradation (Höglund 2001, Cronstand 2007). These concrete degradation models build on the large amount of information derived from so called cement leaching experiments where different amounts of cement are put in contact with aqueous solutions of varying composition and the chemical evolution of the system is followed as a function of the various mineral phases formed and dissolved as degradation proceeds. The general consensus is that cement degradation proceeds through a number of stages which have been mainly defined as the following ones:

Stage 1. During the initial stage of degradation of cement, the pore water composition is dominated by the presence of the alkali hydroxides, mainly Na^+ and K^+. This results in high alkalinity fluids due to the high solubility of the alkaline hydroxides resulting on a pH close to 13. The dissolution of the alkali hydroxides is somewhat retarded by the interaction of the hydroxides with either the CSH phases and/or the ballast (Lagerblad and Trägårdh 1994), resulting on a gradual decrease rather than a stepwise one as previously suggested (Atkins and Glasser 1992, Atkins et al. 1992).

Stage 2. As the alkaline hydroxides are being dissolved, the cement/pore water system is buffered by the solubility of portlandite, $Ca(OH)_2(s)$ and the resulting pH equals to 12.5. This is assumed to be quite a stable stage in the initial degradation of cement and it has been considered in our study as one of the main conditions of this master variable.

Stage 3. As decalcification of cement proceeds, the so called CSH phases are being formed, and the cement/pore water system is controlled by hydrated calcium silicate phases of varying composition and decreasing Ca/silicate ratio. This implies that the resulting pH is buffered around pH=10 and therefore this also constitutes and important value for this master variable in our subsequent studies. The dissolution of these CSH phases is not congruent and depending on the chemical environment a number of secondary phases can build resulting in passivation (due to carbonation and subsequent calcite formation) but also in the deterioration of the mechanical properties of cement (i.e. as a result of ettringite formation in the presence sulphate).

Stage 4. Is the final stage on the alteration of the cement materials, when the chemical characteristics of the pore water are those which are similar to the intruding (Forsmark) groundwaters with pH values around 8.

While, the large amount of cement materials will certainly control the evolution of the alkalinity of the near field at the SFR repository system, the control of the redox conditions will be the result of the interaction of the large amount of steel in the system with the intruding groundwaters. There is a large body of investigations which have dealt with the corrosion of steel under anoxic conditions (see for instance, Smart et al. 2001, Bildstein 2006). The main outcome is that the process controlling the redox evolution of the system is given by the following reaction:

$$3\ Fe(s) + 4\ H_2O \rightarrow Fe_3O_4(s) + 4\ H_2(g) \qquad (1\text{-}1)$$

Which indicates that the corrosion of steel under anoxic conditions proceeds with the consumption of water and the formation of magnetite and hydrogen. The expected redox evolution of the SFR

repository has been modelled by taking into consideration all the potential electron transfer processes, including the anaerobic corrosion of iron as the main one, but also taking into consideration other redox processes, like the oxidation of the aluminium and zinc content and the degradation of the organic content in SFR (including cellulose degradation which we will discuss in the following section), see SKB TR 12-12 (Duro et al. 2012).

The overall outcome of this work is conceptualised in the following Figure 1-1, where the redox ladder of SFR at pH=12.5 is presented.

It is quite clear that the chemical evolution of the near field will impact on the solubility and speciation of key radionuclides with consequences on their migration under repository conditions. As an example, the calculated aqueous speciation of some relevant redox-sensitive radionuclides is given in the following predominance diagrams as presented in SKB TR-12-12 (Duro et al. 2012). These diagrams are calculated based on the state of the art of the thermodynamic database at the time of the report and their validation is one of the potential outcomes of the present work.

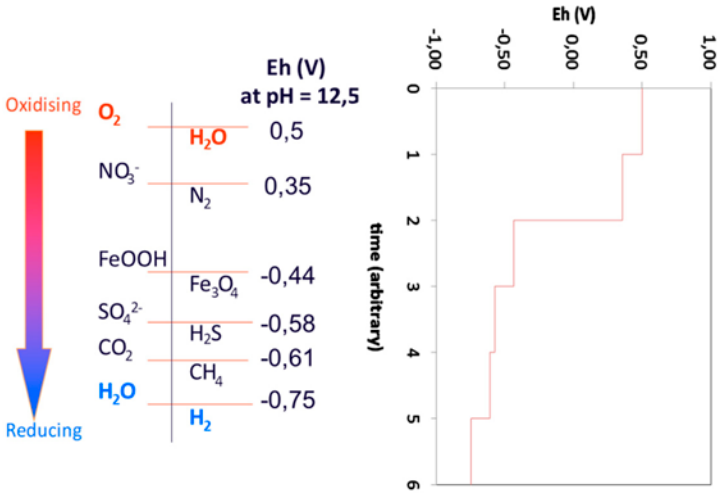

Figure 1-1. *Redox evolution of SFR at pH=12.5 (equilibrium with portlandite).*

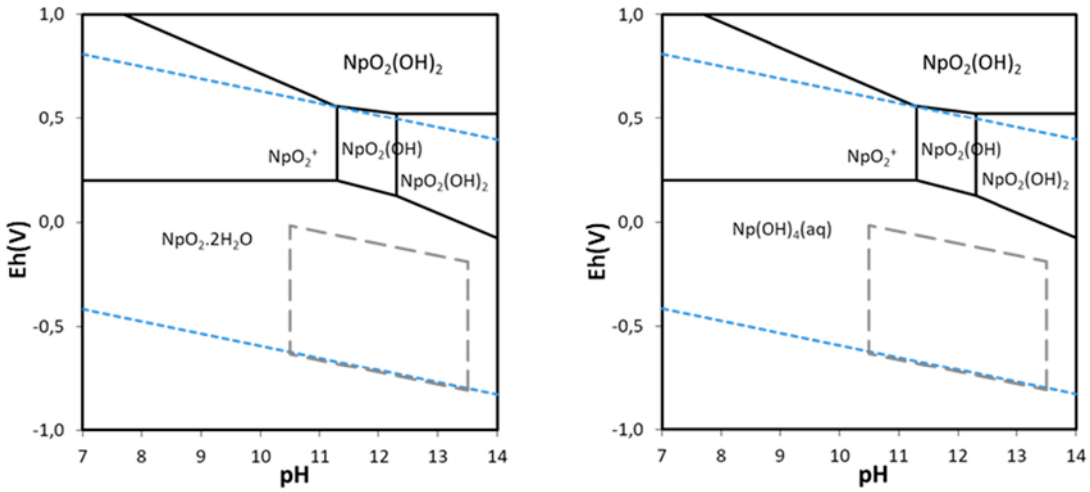

Figure 1-2. *Solid (left) and aqueous (right) predominant speciation of Np in the SFR (redox and pH) space encircled by the dashed insert.*

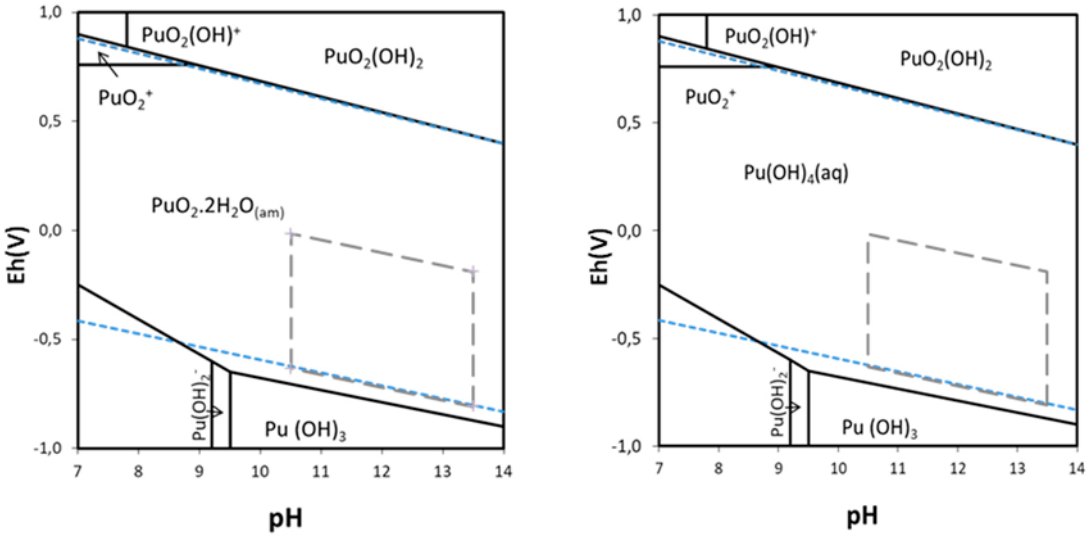

Figure 1-3. *Solid and aqueous speciation of Pu in the SFR (redox and pH) space encircled by the dashed insert.*

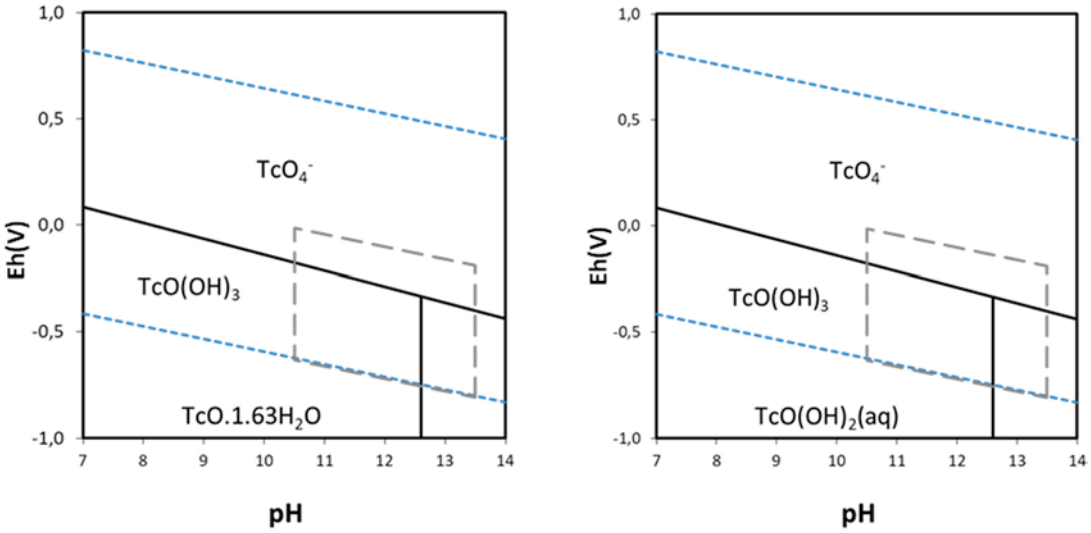

Figure 1-4. *Solid (a) and aqueous (b) speciation of Tc in the SFR (redox and pH) encircled by the dashed insert.*

In addition to the master variables, pH and Eh, the concentration of complexing ligands may also increase the solubility and consequently radionuclide migration. One particularly relevant process in this context is related to the degradation of the large amounts of cellulose present in the SFR repository. This is a process that has been largely studied and the main conclusion for this study is that under high alkalinity conditions the degradation of cellulose is mainly chemical and it produces isosaccharinic acids (ISA) (Glaus et al. 1999). The degradation is kinetically controlled with characteristic reaction times in the range of thousand years (Glaus and Van Loon 2008). ISA is a strong complexing agent and may consequently increase the solubility of selected radionuclides.

In this context, SKB decided to initiate a PhD which would help to bring precise and quantitative information, on a number of issues related to the effect of the SFR pH and Eh conditions on the solubility and speciation of uranium, plutonium and technetium as well as the combined effect of these Eh, pH conditions and the expected ISA concentrations on the mobility of ^{59}Ni a relevant radionuclide in the PSU safety assessment.

2 Objectives

The objective of this work has been the experimental determination as well as the thermodynamic modelling of some key processes for the evolution of the near field of the SFR repository.

Namely:

1. To investigate the thermodynamics of the Fe(II)/Fe_3O_4(s) redox system and to determine the solubility equilibria of Fe_3O_4(s) under high pH and strongly reducing conditions.
2. To study the effect of these redox conditions on the redox state and mobility of key redox sensitive radionuclides like Pu, U and Tc.
3. To determine the solubility of Ni(II) under the alkaline/reducing conditions imposed by the magnetite/Fe(II), including the effect of isosaccharinic acid (ISA) a key product of the cellulose degradation under alkaline/reducing conditions.
4. To determine the sorption processes of Ni(II) on cement, in the presence of ISA and under the alkaline/reducing conditions of the system.

We will first make an account of the main experimental and modelling investigations and in a later stage we will discuss the PA implications of these findings.

3 Experimental studies

In this section we will present the main experimental and modelling aspects concerning the systems investigated:

These are:

1. Redox chemistry and solubility of Fe in reducing alkaline to hyperalkaline conditions: Fe(0)–Fe_3O_4–Fe(II)(aq) system.
2. Study of the redox state of Pu, U and Tc under highly alkaline conditions and in the presence of iron and its anaerobic corrosion products.
3. Thermodynamic model of Ni(II) solubility, hydrolysis and complex formation with ISA.
4. Uptake of Ni(II) by cement in the presence of ISA.

3.1 Study of the redox chemistry and solubility of Fe in reducing alkaline to hyperalkaline conditions: Fe(0)-Fe_3O_4-Fe(II)aq system

3.1.1 Introduction

As previously presented, the anoxic corrosion of Fe is expected to generate highly reducing conditions in low and intermediate nuclear waste repositories. At the same time the presence of cementitious materials will impose highly alkaline pH conditions to the contacting water. These master variables conditions will impact the chemical behaviour of the redox sensitive radionuclides. An appropriate knowledge of the evolution of the chemical boundary conditions is essential to establish reliable models for radionuclide migration. Key uncertainties remain on the consequences of these chemical conditions developed in the presence of iron-bearing and cementitious materials. Magnetite (Fe_3O_4) has been identified as one of the main products resulting from the anoxic corrosion of metallic iron and steel (Smart et al. 2001, Bildstein 2006, Duro et al. 2014). The knowledge on the thermodynamics of the iron system under reducing and highly alkaline conditions is rather limited. As a consequence, the NEA–TDB does not select any neutral or anionic hydrolysis species of Fe(II) and Fe(III) (Lemire et al. 2013), which are expected to dominate the aqueous chemistry of iron under reducing and hyperalkaline conditions. Hence, we decided to study the solubility of well-characterised crystalline magnetite under reducing conditions and at varying pH.

3.1.2 Experimental

All experiments were performed at $T = (22 \pm 2)$ °C under inert gas (Ar) atmosphere in gloveboxes (with $O_2 < 5$ ppm). Batch solubility experiments were performed at undersaturation conditions with α-Fe_3O_4(cr) prepared hydrothermally following the procedure described by Schwertmann and Cornell (2000). In the undersaturation approach, a solid phase previously synthesized is equilibrated with a matrix solution of given pH_m, E_h and ionic strength. This approach decreases the risk of colloid formation, which occurs often when approaching solubility phenomena from oversaturation conditions. In the latter case, solubility phenomena are studied with a solid phase precipitated in-situ from a highly concentrated metal (Fe in this case) solution. Although undersaturation and oversaturation approaches should lead to the same result / solubility after sufficiently long equilibration times, kinetics and colloids formation often hinder the attainment of equilibrium conditions in oversaturation studies. Thus, undersaturation conditions represent the most reliable solubility approach to derive thermodynamic properties of a given system, and have been accordingly favored in this study.

A total of 32 independent batch samples were prepared using 30 mg α-Fe_3O_4(cr) in 20 mL per experiment. Samples were performed within $8 \leq pH_m \leq 13$ (with $pH_m = -\log [H^+]$) in 0.1 M NaCl–NaOH solutions. Four different redox systems were defined:

- S1. α-Fe_3O_4(cr)
- S2. α-Fe_3O_4(cr) + 15 mg Fe(0) that bracketed (pe + pH_m) from −1 to +3
- S3. α-Fe_3O_4(cr) + 0.01 M Sn(II) that bracketed (pe + pH_m) from −1 to +1
- S4. α-Fe_3O_4(cr) + 0.01 M $Na_2S_2O_4$ that bracketed (pe + pH_m) from −1 to 0

Samples were stored under Ar atmosphere and regularly shaked manually. [Fe], pH_m and E_h were monitored at regular time intervals for up to 480 days. The apparent electron activity (pe = -$\log a_{e^-}$) was calculated from pe = 16.9 E_h [V], according to the equation $E_h = -\frac{RT\ln 10}{F}\log a_e$-. Dissolved [Fe]$_{tot}$ was measured by ICP–MS after ultrafiltration (10 kD filters, Pall Life Sciences) involving a centrifugation step at 4020 *g* inside the glovebox. ICP–MS measurements were performed using a Sector Field ICP–MS (Thermo X-Serie II) at medium and high resolution mode.

The experimental details are as follows:

- 30 mg magnetite per sample were placed in contact with the solutions. The magnetite was prepared at 80 °C. The characterization of the solid obtained gave the following results:
  - (29 ± 5) % Fe(II) as quantified by XPS.
  - Particle size: 60–120 nm as quantified by SEM, Rietveld analysis of XRD data and AFM measurements.

The stability field of water varies monotonically with (pe + pH) according with the corresponding oxidation and reduction reactions:

$$0.5H_2O(l) \Leftrightarrow 0.25O_2(g) + H^+ + e^- \quad (3\text{-}1)$$

$$H^+ + e^- \Leftrightarrow 0.5H_2(g) \quad (3\text{-}2)$$

With the equilibrium constants $\log K°(1) = 0.25 \log P(O_2(g)) - pH - pe - 0.5 \log a_w = -20.77$ and $\log K°(2) = 0.5 \log P(H_2(g)) + pH + pe = 0$. Accordingly, the term (pe + pH) (or rather (pe + pH_m, using H^+ concentration instead of activity) is favored along this report to design the redox conditions of a given system.

3.1.3 Results and discussion

pH_m *and* E_h *measurements*

Figure 3-1 shows experimental measurements of pH_m and E_h for all of the samples evaluated in the redox systems S1, S2, S3 and S4. Experimental data are plotted in the predominance diagram of Fe aqueous species (left) and solid compounds (right), as calculated with thermodynamic data selected in ThermoChimie TDB (Giffaut et al. 2014, Grivé et al. 2015).

The experimentally measured data in Figure 3-1 show that the system S1 clearly gives the highest pe values of all the evaluated systems, $+3 \le (pe + pH_m) \le +5$. Moreover, the redox conditions in the system S2 vary from (pe + pH_m) ≈ –1 (at $8 \le pH_m \le 9$) to (pe + pH_m) ≈ +3 (at $12 \le pH_m \le 13$). Hence, the presence of Fe(0) promotes very reducing conditions at $pH_m \approx 9$ (close / at the border of water reduction[1]), but results only in moderate reducing E_h values at $pH_m = 12.8$. This observation is consistent with previous results reported by Yalçıntaş et al. (2015). The increase of (pe + pH_m) occurring in hyperalkaline systems is expectedly due to the passivation of the surface of Fe(0) and corresponding formation of corrosion products. Indeed, E_h values measured for Fe_3O_4(cr) in the absence of Fe(0) at $pH_m = 12.8$ are in excellent agreement with the values obtained in the presence of Fe(0). The possible passivation of the surface of Fe(0) is further supported by XPS and SEM-EDS data provided in the Appendix (see Table A1-1 and Figure A1-4).

Very low and reproducible E_h values with $0 \le (pe + pH_m) \le +2$ are measured for magnetite system in the presence of Sn(II). These values are consistent with previous investigations using Sn(II) (in the absence of magnetite) (Yalçıntaş et al. 2016, Tasi et al. 2018). Even lower values ($pe + pH_m \le 0$) are obtained for the samples buffered with $Na_2S_2O_4$ (S4, blue points in Figure 4-1). Gas bubbles were observed in some of the samples of this system, thus indicating the formation of H_2(g).

[1] The formation of gas bubbles (H_2) was observed in several samples of the S2 system at $pH_m \le 10$.

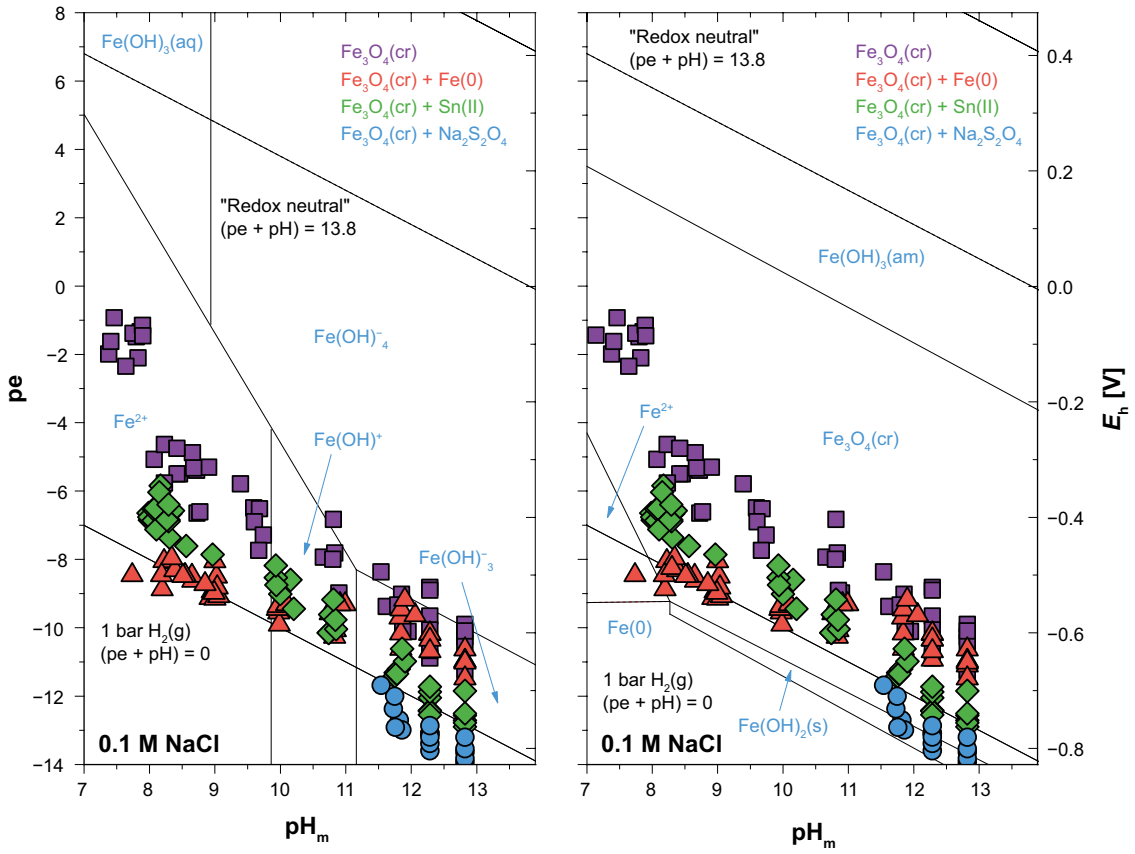

Figure 3-1. *Pourbaix diagrams of Fe aqueous species (left) and solid compounds (right) calculated at I = 0.1 M NaCl with thermodynamic data selected in ThermoChimie TDB (Giffaut et al. 2014, Grivé et al. 2015). Purple squares correspond to S1. α-Fe_3O_4(cr) system; red triangles to S2. α-Fe_3O_4(cr) + Fe(0) system; green diamonds to S3. α-Fe_3O_4(cr) + $SnCl_2$ system and blue circles to S4. α-Fe_3O_4(cr) + $Na_2S_2O_4$ system. All calculations performed at* $[Fe]_{tot}$ *= 0.001 M.*

Solubility of α-Fe_3O_4(cr) in different reducing systems

The experimentally measured solubility of α-Fe_3O_4(cr) in the four different reducing systems S1. α-Fe_3O_4(cr); S2. α-Fe_3O_4(cr) + Fe(0); S3. α-Fe_3O_4(cr) + $SnCl_2$ and S4. α-Fe_3O_4(cr) + $Na_2S_2O_4$, are shown in Figure 3-2. The figure includes only data above the detection limit (1×10^{-8} M, calculated as 3 standard deviations of the blank). As visual aid, the figure includes thermodynamic calculations for the solubility of Fe_3O_4 (cr) at (pe + pH) = 4 (red line, lower solubility) and (pe + pH) = 0 (black line, higher solubility). Thermodynamic calculations were performed using the thermodynamic data selection for Fe in ThermoChimie TDB (Giffaut et al. 2014, Grivé et al. 2015).

A significant decrease in the solubility with a log $[Fe]_{aq}$ vs. pH_m slope of –2 / –3 within $8 \leq pH_m \leq 9.5$ is observed in the experimental data shown in Figure 3-2 for the systems S1, S2 and S3. Furthermore, in the same pH-region of the three different systems, the solubility significantly increases with decreasing E_h following the sequence:

S2.Fe_3O_4+Fe(0) system > S3.Fe_3O_4+$SnCl_2$ system >> S1.Fe_3O_4 system

The pure magnetite systems give higher E_h values throughout the complete pH-range evaluated, (pe+pH) ~ +4 (see Figure 3-1). In both, pH-E_h and solubility measurements performed for this system is possible to observe a significant data dispersion. This is attributed to the "less-buffered" redox conditions applying to this system (absence of other strong reducing agents such as Fe(0), Sn(II) or $Na_2S_2O_4$). Because of this observation, experimental data collected for pure magnetite has not been considered to extract thermodynamic data, and instead has been only used to validate the thermodynamic model derived from the other, less scattered systems.

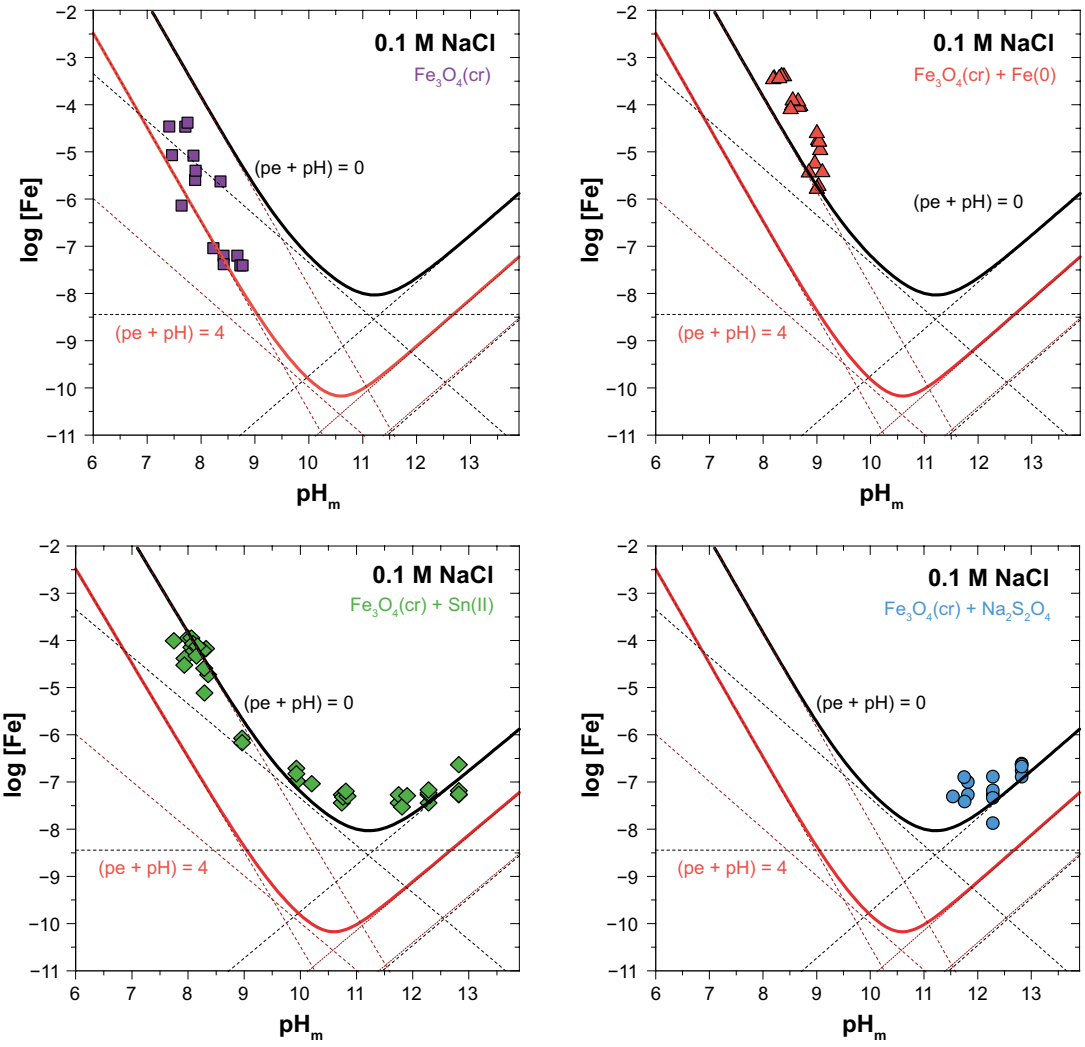

Figure 3-2. *Experimental solubility data of α-Fe_3O_4 determined in the present work in 0.1M NaCl-NaOH solutions for the four systems: purple squares correspond to S1. α-Fe_3O_4(cr) system; red triangles to S2. α-Fe_3O_4(cr) + Fe(0) system; green diamonds to S3. α-Fe_3O_4(cr) + $SnCl_2$ system and blue circles to S4. α-Fe_3O_4(cr) + $Na_2S_2O_4$ system. Solid lines: Fe_3O_4(cr) solubility calculated with ThermoChimie TDB (Giffaut et al. 2014) for pe+pH = 0 (black) and pe+pH = +4 (red). Calculations at I=0.*

Figure 3-2 shows that the aqueous iron concentration above pH_m ~10 remain below 10^{-7} M and show relatively large dispersion, but it is consistent with the formation of negatively-charged Fe(II) hydrolysis species above pH_m ~11.5. The presence of magnetite in all samples for the 4 systems, S1.α-Fe_3O_4(cr), S2.α Fe_3O_4(cr)+Fe(0), S3.α-Fe_3O_4(cr)+$SnCl_2$ and S4.α-Fe_3O_4(cr)+$Na_2S_2O_4$ system is confirmed by XRD (see Appendix 1). However, we note that the ratio Fe(II):Fe(III) in magnetite as quantified by XPS was slightly altered in the more reducing systems: the (29 ± 5) % Fe(II) content in the original magnetite material was increased at pH_m = 12.8 to (34 ± 5) % and (32 ± 5) % in the presence of Sn(II) and $Na_2S_2O_4$, respectively.

Thermodynamic interpretation of α-Fe_3O_4(cr) solubility

Solubility data of Fe_3O_4(cr) obtained in different reducing systems in combination with experimental pH_m and E_h values are used in this section to derive the solubility product of magnetite as well as hydrolysis constants of Fe. Because of the complexity imposed by the possible co-existence of Fe(II) and Fe(III) species in the aqueous phase, we have only considered in this thermodynamic interpretation those systems with very reducing conditions, where we can safely assume (according to the current thermodynamic data available) the predominance of Fe(II) aqueous species (see Figure 3-1):

- Fe_3O_4(cr) + Fe(0) systems at $pH_m < 11$.
- Fe_3O_4(cr) + Sn(II) systems within the complete pH_m-range investigated ($8 \le pH_m \le 13$).
- Fe_3O_4(cr) + $Na_2S_2O_4$ systems at $pH_m \ge 11.5$.

Thermodynamic data derived in the present work has been compared with the following literature and thermodynamic databases:

- Solubility studies with Fe_3O_4(cr) under reducing conditions at elevated temperatures ($T \ge 50$ °C) (Sweeton and Baes 1970, Kanert et al. 1976, Tremaine and LeBlanc 1980, Ziemniak et al. 1995, Palmer et al. 1997).
- Solubility study with „$Fe(OH)_2$(s)“ at $T = 25$ °C (Gayer and Woontner 1956).
- Thermodynamic databases and thermodynamic compilations:
  - Baes and Mesmer (1976).
  - Chivot (2004).
  - PSI-NAGRA TDB (Hummel et al. 2002, Thoenen et al. 2014).
  - NEA TDB (Lemire et al. 2013).
  - Thermochimie TDB (Giffaut et al. 2014, Grivé et al. 2015).

Thermodynamic data derived in the present work

Solubility data determined in the systems described above have been interpreted according with the solubility equilibria (4) to (7):

$$0.33\ Fe_3O_4(cr) + 2.67\ H^+ + 0.67\ e^- \Leftrightarrow Fe^{2+} + 1.33\ H_2O(l) \quad (3\text{-}3)$$

with $\log\ {}^*K^\circ_{s,0} = \log [Fe^{2+}] + 2.67\ pH_m + 0.67\ pe + 1.33 \log a_w + \log \gamma_{Fe}2+ - 2.67 \log \gamma_H+$

$$0.33\ Fe_3O_4(cr) + 1.67\ H^+ + 0.67\ e^- \Leftrightarrow Fe(OH)^+ + 0.33\ H_2O(l) \quad (3\text{-}4)$$

with $\log\ {}^*K^\circ_{s,1} = \log [Fe(OH)^+] + 1.67\ pH_m + 0.67\ pe + 0.33 \log a_w + \log \gamma_{Fe(OH)}+ - 1.67 \log \gamma_H+$

$$0.33\ Fe_3O_4(cr) + 0.67\ H^+ + 0.67\ H_2O(l) + 0.67\ e^- \Leftrightarrow Fe(OH)_2(aq) \quad (3\text{-}5)$$

with $\log\ {}^*K^\circ_{s,2} = \log [Fe(OH)_2(aq)] + 0.67\ pH_m + 0.67\ pe - 0.67 \log a_w - 0.67 \log \gamma_H+$

$$0.33\ Fe_3O_4(cr) + 1.67\ H_2O(l) + 0.67\ e^- \Leftrightarrow Fe(OH)_3^- + 0.33\ H^+ \quad (3\text{-}6)$$

with $\log\ {}^*K^\circ_{s,3} = \log [Fe(OH)_3^-] - 0.33\ pH_m + 0.67\ pe - 1.67 \log a_w + \log \gamma_{Fe(OH)3}- + 0.33 \log \gamma_H+$

A simultaneous fit of the three datasets described above considering equilibrium reactions (3-3) to (3-6) was attempted without success because of the excessive number of fitting parameters (log ${}^*K^\circ_{s,0}$, log ${}^*K^\circ_{s,1}$, log ${}^*K^\circ_{s,2}$ and log ${}^*K^\circ_{s,3}$) and variables (log $[Fe]_{tot}$, pH_m and pe). Accordingly, the following approach was used in the fit of the experimental solubility data:

- Experimental solubility datasets obtained in {Fe_3O_4(cr) + Fe(0)} and {Fe_3O_4(cr) + Sn(II)} systems with $pH_m \le 9$ follow a slope of ≈ –2. The slope analysis in log [M] vs. pH_m diagrams where M is a redox-sensitive metal depends not only on pH_m but also on pe. Provided that the relation $pe = A + B\ pH_m$ has a slope of $B \approx -1$ for both {Fe_3O_4(cr) + Fe(0)} and {Fe_3O_4(cr) + Sn(II)} systems in the pH_m-region under discussion, a slope of –2 is consistent with the solubility equilibrium between Fe_3O_4(cr) and Fe^{2+}. The predominance of Fe^{2+} in these (pe + pH_m) conditions is also predicted according with previous thermodynamic data. Both datasets have been fitted according with reaction (1) and corresponding log ${}^*K^\circ_{s,0}$.
- The solubility of Fe_3O_4(cr) above $pH_m \approx 11$ shows a systematic increase both in Sn(II) and $Na_2S_2O_4$ systems. Such increase can only be explained by the formation of anionic hydrolysis species of Fe ($Fe^{II}(OH)_3^-$ or $Fe^{III}(OH)_4^-$). As indicated above, our working hypothesis is that Fe(II) aqueous species are predominant in the very reducing conditions investigated in this study, and thus this dataset has been fitted according with reaction (4) (predominance of $Fe^{II}(OH)_3^-$) and corresponding log ${}^*K^\circ_{s,3}$. We note that the predominance of $Fe^{II}(OH)_3^-$ rather than $Fe^{III}(OH)_4^-$ in the very reducing conditions of our study is also predicted with currently available thermodynamic data.

- Solubility data in $\{Fe_3O_4(cr) + Sn(II)\}$ systems with $10 \leq pH_m \leq 11$ have been fitted according with reaction (2) and corresponding log $*K°_{s,1}$. The slope in this pH_m-region is close to ≈ -1. This slope is consistent with the predominance of $FeOH^+$ in the aqueous phase, as also suggested with currently available thermodynamic data. The fit of the experimental data has considered the contribution of Fe^{2+} according with log $*K°_{s,0}$ determined in the present work.
- Experimental solubility datasets obtained in $\{Fe_3O_4(cr) + Sn(II)\}$ and $\{Fe_3O_4(cr) + Na_2S_2O_4\}$ systems with with $11.5 \leq pH_m \leq 11.9$ have been fitted according with reaction (3) and corresponding log $*K°_{s,2}$. The predominance of the neutral species $Fe(OH)_2(aq)$ is consistent with the pH_m-independent solubility observed in this pH_m-region for the $\{Fe_3O_4(cr) + Sn(II)\}$ system.

The fit of the solubility datasets indicated above has resulted in the following equilibrium constants:

log $*K°_{s,0} = (12.9 \pm 0.4)$.

log $*K°_{s,1} = (4.1 \pm 0.3)$.

log $*K°_{s,2} = -(7.5 \pm 0.6)$.

log $*K°_{s,3} = -(19.9 \pm 0.3)$.

Activity coefficients required for the determination of log $*K°_{s,x}$ in equations (3-3) to (3-6) have been calculated using the SIT approach (Ciavatta 1980). SIT ion interaction coefficients required for Fe(II) species have been either taken from Lemire et al. (2013) or estimated using the approach described by Hummel (2009):

$\varepsilon(Fe^{2+}, Cl^-) = (0.17 \pm 0.01)$ kg · mol^{-1} (Lemire et al. 2013).

$\varepsilon(FeOH^+, Cl^-) = (0.05 \pm 0.10)$ kg · mol^{-1} (estimated according with Hummel 2009).

$\varepsilon(Fe(OH)_2(aq), Na^+/Cl^-) = 0$ kg · mol^{-1} (by definition in SIT).

$\varepsilon(Fe(OH)_3^-, Na^+) = -(0.05 \pm 0.10)$ kg · mol^{-1} (estimated according with Hummel 2009).

We have to take into consideration that under the relatively low ionic strength of the current study most of the non-ideality behaviour is captured by the Debye-Hückle function and that the impact of the estimated interaction coefficients is rather limited.

Figure 3-3 shows a comparison of experimental solubility data determined in $\{Fe_3O_4(cr) + Fe(0)\}$, $\{Fe_3O_4(cr) + Sn(II)\}$ and $\{Fe_3O_4(cr) + Na_2S_2O_4\}$ systems with thermodynamic calculations using the model described above. These solubility plots represent only two dimensions (log $[Fe]_{tot}$ vs. pH_m), whereas solubility is also depending upon pe, and should accordingly be only considered as a qualitative view of the agreement of the model with experimental data. The value of $(pe + pH_m)$ in $\{Fe_3O_4(cr) + Sn(II)\}$ systems varies along the pH_m series, and thus thermodynamic calculations have been performed using pe values calculated with the expression $pe = 3.8 - 1.3\ pH_m$. This expression has been obtained by the linear fit of pe *vs*. pH_m in Figure 3-1.

A more accurate comparison of experimental data (as log $[Fe]_{calc}$, x axis) *vs.* model calculations (as log $[Fe]_{exp}$, y axis) is given in Figure 3-4, where experimental pH_m and pe values have been considered in combination with log $*K°_{s,x}$ (with x = 0–3) determined in the present work for the calculation of $[Fe]_{calc}$ according with equation (3-7). As discussed above, the very reducing conditions imposed by Fe(0), Sn(II) and $Na_2S_2O_4$ allow disregarding the formation (in significant proportions) of Fe(III) aqueous species, which are accordingly omitted in equation (3-7).

$$[Fe]_{tot} = [Fe^{2+}] + [FeOH^+] + [Fe(OH)_2(aq)] + [Fe(OH)_3^-] \quad (3\text{-}7)$$

Figure 3-3 and Figure 3-4 show that solubility calculations using thermodynamic data derived in the present work from solubility experiments with $Fe_3O_4(cr)$ satisfactorily explain experimental observations obtained in the presence of three different reducing systems: Fe(0), Sn(II) and $Na_2S_2O_4$. The good agreement with experimental data obtained in such a different reducing systems provides further confidence on the thermodynamic data derived in the present solubility study.

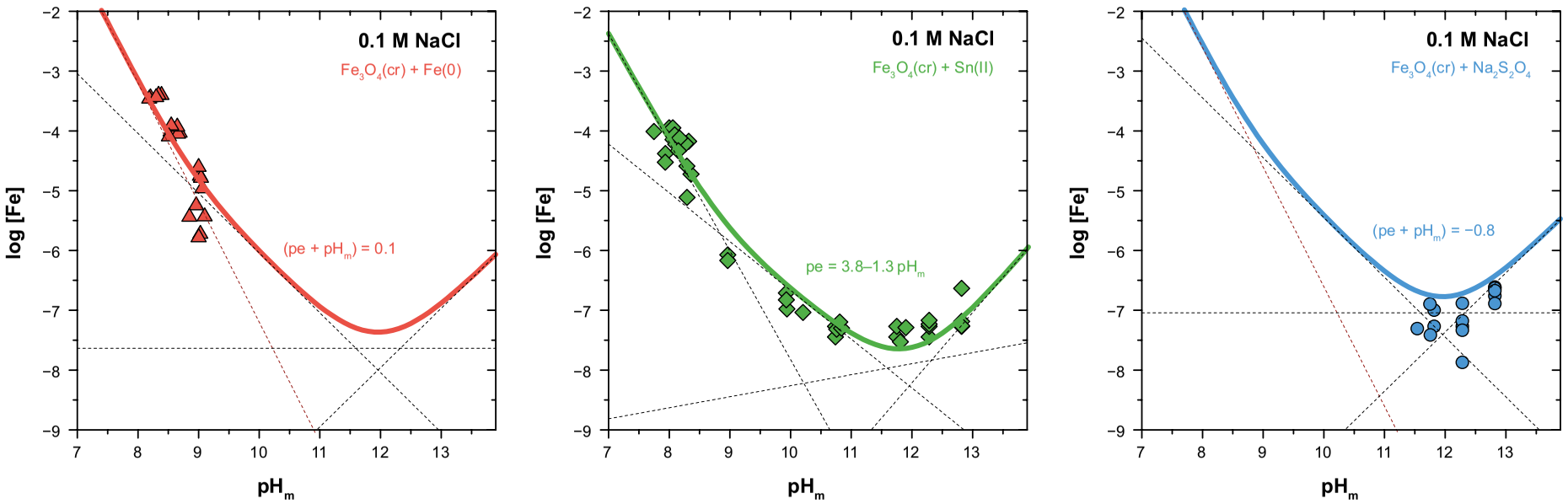

Figure 3-3. *Experimental solubility data for Fe_3O_4(cr) determined in the present work in different reducing systems: a. Fe(0); b. Sn(II); c. $Na_2S_2O_4$. Thick solid lines correspond to the solubility of Fe_3O_4(cr) calculated thermodynamic data derived in the present work and the following ($pe + pH_m$) values: a. 0.1; b. $pe = 3.8 \times pH_m$ (see text); c. −0.8.*

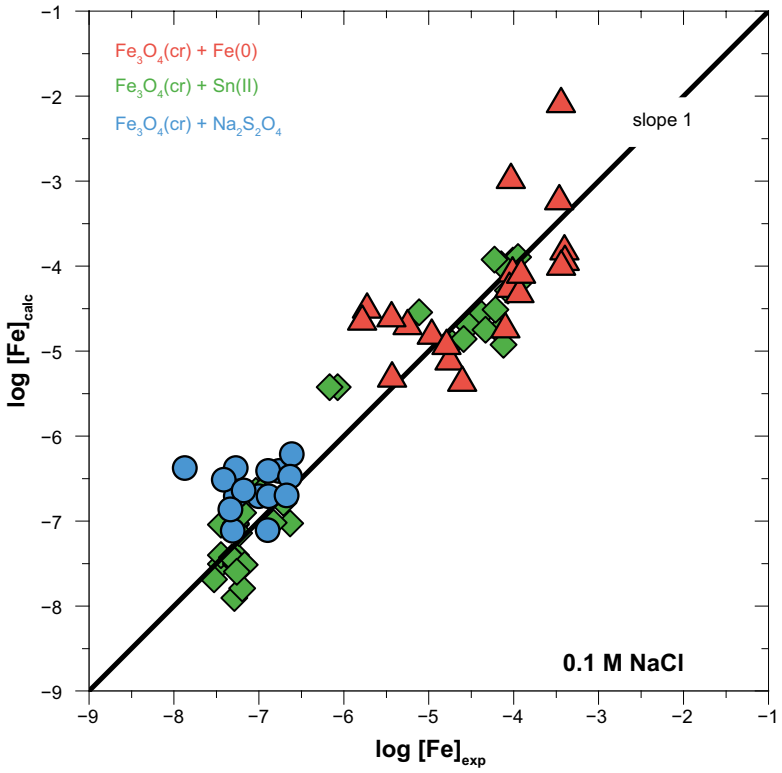

Figure 3-4. *Comparison of Fe concentrations measured experimentally (x-axis) and calculated (y-axis) for the solubility of Fe_3O_4(cr) in the presence of different reducing systems (Fe(0), Sn(II) and $Na_2S_2O_4$). Solubilites calculated using thermodynamic model derived in the present work and experimental pH_m and pe values.*

The ratio Fe(II):Fe(III) in the original magnetite material (29 ± 3 %) slightly increased in the reducing systems investigated in the present study: 32 ± 3 % in Fe(0) (at pH_m = 9), 32 ± 3 % in $Na_2S_2O_4$ (at pH_m = 12.8) and 34 ± 3 % in Sn(II) (at pH_m = 12.8). We note that the Fe(II):Fe(III) ratio in pure, stoichiometric magnetite is 33.3 %. Accordingly, our experimental observations reflect the reduction of Fe(III) in the original (oxidized) surface to a Fe(II):Fe(III) ratio close the stoichiometric value in Fe_3O_4(cr) (33.3 %). We further note that for the {Fe_3O_4(cr) + Fe(0)} system at pH_m = 12.8, a Fe(II):Fe(III) ratio of 28 ± 3 % was quantified by XPS. As discussed above, Fe(0) does not provide strongly reducing conditions in hyperalkaline systems, likely as a result of the passivation of its surface. Because of the more oxidizing conditions posed by this system and the expected presence of Fe(III) hydrolysis species, solubility data determined in {Fe_3O_4(cr) + Fe(0)} above $pH_m \approx 10$ was not considered in the thermodynamic interpretation described above.

Figure 3-5 shows a comparison of experimental solubility data determined for Fe_3O_4(cr) in the absence of other reducing systems and the solubility calculated using the thermodynamic model derived in the present work. Because of the large variation of (pe + pH_m) values in this system (see Figure 3-1), we have performed these calculations for an upper and lower limit of (pe + pH_m), namely +2 and +6. As shown in the figure, all solubility values are embraced within this (pe + pH_m) range. This qualitative exercise provides further confidence on the thermodynamic data derived in the present work.

Comparison with data available in the literature summarizes the equilibrium constants determined in the present work for the solubility of magnetite and Fe(II) hydrolysis, together with thermodynamic data reported for the same reactions in the most relevant thermodynamic compilations and databases on Fe (Baes and Mesmer 1976, Chivot 2004, PSI-Nagra TDB, NEA-TDB and Thermochimie TDB). This comparison is used afterwards for an in-depth discussion of log $*K°_{s,0}${Fe_3O_4(cr)} and hydrolysis constants of Fe(II).

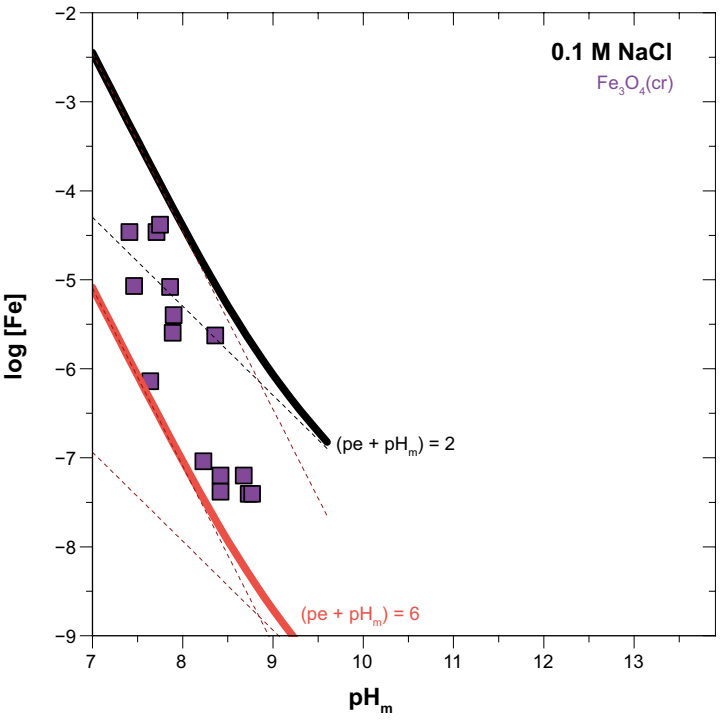

Figure 3-5. *Experimental solubility data for Fe_3O_4(cr) determined in the present work in the absence of other reducing systems. Solid lines correspond to the solubility of Fe_3O_4(cr) calculated with thermodynamic data derived in the present work and (pe + pH_m) = 2 (red line) and (pe + pH_m) = 6 (black line).*

Table 3-1. Equilibrium constants determined in the present work (p.w.) for the solubility of magnetite and Fe(II) hydrolysis, and comparison with thermodynamic data selected in Baes and Mesmer (1976), Chivot (2004), PSI-Nagra TDB, NEA-TDB and Thermochimie TDB.

Reaction	log *K°	Reference
0.33 Fe_3O_4(cr) + 2.67 H+ + 0.67 e– ⇔ Fe^{2+} + 1.33 H_2O(l)	(12.9 ± 0.4)	(p.w.)
	12.05	Chivot (2004)
	12.02	PSI-Nagra TDB
	12.12	NEA-TDB
	12.15	Thermochimie TDB
Fe^{2+} + H_2O(l) ⇔ $Fe(OH)^+$ + H^+	–(8.8 ± 0.5)	(p.w.)
	–(9.5 ± 0.1)	Baes and Mesmer (1976)
	–9.5	Chivot (2004)
	–9.5	PSI-Nagra TDB
	–(9.1 ± 0.4)	NEA-TDB
	–9.5	Thermochimie TDB
Fe^{2+} + 2 H_2O(l) ⇔ $Fe(OH)_2$(aq) + 2 H^+	–(20.4 ± 0.7)	(p.w.)
	–(20.6 ± 1.0)	Baes and Mesmer (1976)
	–20.6	Chivot
	–20.6	Thermochimie TDB
Fe^{2+} + 3 H_2O(l) ⇔ $Fe(OH)_3^-$ + 3 H^+	–(32.8 ± 0.5)	(p.w.)
	–(31 ± 1.5)	Baes and Mesmer (1976)
	–31.9	Chivot
	–31.9	Thermochimie TDB

*Discussion of log *K°$_{s,0}${Fe_3O_4(cr)}*

The first equilibrium reaction in Table 3-1 shows that the equilibrium constant determined in the present work for the reductive dissolution of Fe_3O_4(cr) is signficantly higher (almost one order of magnitude) than the corresponding constants calculated using thermodynamic data selected in Chivot (2004), PSI-Nagra TDB, NEA-TDB and Thermochimie TDB. We note here that thermodynamic data selected for Fe_3O_4(cr) in all these databases is based upon thermochemical studies with very crystalline solid phases synthesized at very high temperatures. It is a very common observation that such thermochemical studies (providing enthalpy and entropy data) result in more negative values of $\Delta_f G°_m$ (and consequently in smaller solubility constants, log *$K°_{s,0}$) than solubility experiments conducted in aqueous systems at ambient temperature.

Although not using such data for the final thermodynamic selection, the NEA–TDB (Lemire et al. 2013) critically reviewed the existing solubility data for Fe_3O_4(cr), and evaluated the solubility constants that can be derived from these experiments. The existing studies (accepted by NEA reviewers, Sweeton and Baes 1970, Tremaine and LeBlanc 1980) were performed at $T \geq 50$ °C, and different approaches were used to extrapolate these data to the reference state, i.e. $T = 25$ °C. Figure 3-6 shows log *$K°_{s,0}$ values determined in the present work (at $T = 22$ °C), reported in Sweeton and Baes (1970) (for $50 \leq T$ [°C] ≤ 300) and in Tremaine and LeBlanc (1980) (for $100 \leq$ T [°C] ≤ 300), together with model calculations using the four different approaches discussed in the NEA-TDB.

Table 3-2 Summarizes the values of log *$K°_{s,0}$ extrapolated by the NEA–TDB to $T = 25$ °C and reported in the present work at $T = 22$ °C. For comparison purposes, Figure 3-6 includes also the value of log *$K°_{s,0}$ calculated in this study using $\Delta_f G°_m(Fe_3O_4)$ selected in the NEA–TDB from thermochemical studies.

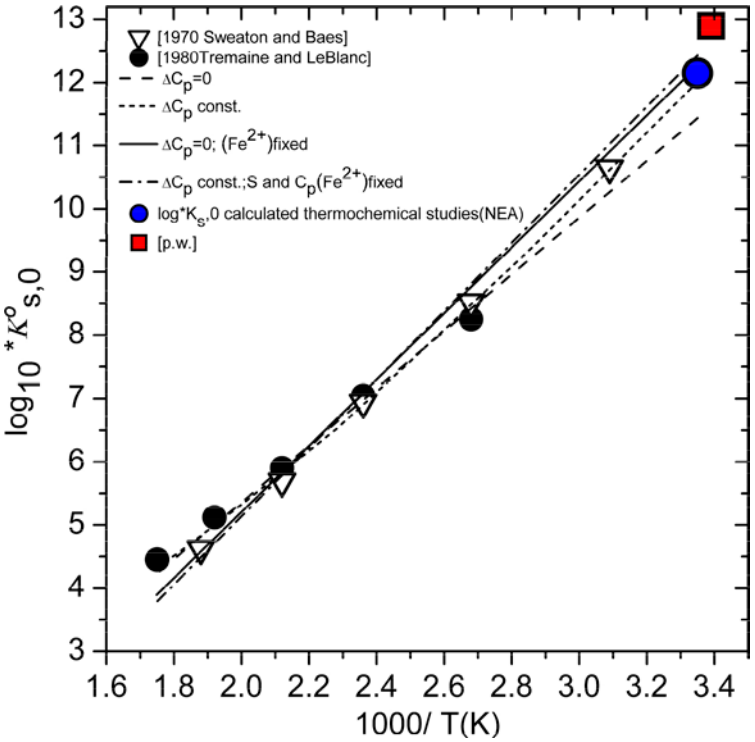

Figure 3-6. *Equilibrium constants determined in the present work ($T = 22$ °C), reported in Sweeton and Baes (1970) ($50 \leq T$ [°C] ≤ 300) and in Tremaine and LeBlanc (1980) ($100 \leq T$ [°C] ≤ 300) for the solubility reaction 0.33 Fe_3O_4(cr) + 2.67 H^+ + 0.67 e^- ⇔ Fe^{2+} + 1.33 H_2O(l). Solid and dashed lines show the temperature dependence of log *K°$_{s,0}$ calculated using the four different approaches outlined in the NEA–TDB (Lemire et al. 2013). Red symbol corresponds the value of log *K°$_{s,0}$ calculated internally using $\Delta_f G°_m(Fe_3O_4)$ selected in the NEA–TDB from thermochemical studies.*

Table 3-2. Values of log $*K°_{s,0}$ determined in the present work at $T = 22$ °C and extrapolated in the NEA–TDB based upon solubility data reported in Sweeton and Baes (1970) and in Tremaine and LeBlanc (1980) within the temperature range 50 ≤ T [°C] ≤ 300.

Reference	log $*K°_{s,0}$	Temperature range of original experimental data [°C]	Comments
Present work	(12.9 ± 0.4)	22	
NEA–TDB (Lemire et al. 2013)	Fit 1: 12	50–300	Fit 1: $\Delta C_p = 0$
	Fit 2: 11.5		Fit 2: ΔC_p const.
	Fit 3: 12.3		Fit 3: $\Delta C_p = 0$; $S(Fe^{2+})$ fixed
	Fit 4: 12.5		Fit 4: ΔC_p const.; S and $C_p(Fe^{2+})$ fixed
NEA–TDB (Lemire et al. 2013)	12.12		Calculated internally from $\Delta_f G°_m(Fe_3O_4)$ selected from thermochemical studies

Although not included in the table of selected values, the NEA-TDB favors fit number 4 (resulting in log $*K°_{s,0} = 12.5$) in their discussion. This value lays between log $*K°_{s,0}$ derived in the present work at $T = 22$ °C and the solubility constant calculated internally from $\Delta_f G°_m$ selected from thermochemical studies.

Differences in the experimental approach used may contribute to explain the disagreement between log $*K°_{s,0}$ determined in the present work at $T = 22$ °C and log $*K°_{s,0}$ extrapolated to $T = 25$ °C from solubility studies performed at $50 \leq T\,[°C] \leq 300$. Table 3-3 summarizes some key features in the experimental approach used in this work and considered in Sweeton and Baes (1970) and in Tremaine and LeBlanc (1980):

Table 3-3. Main features of the solubility experiments with Fe_3O_4(cr) performed in the present work, Sweeton and Baes (1970) and Tremaine and LeBlanc (1980).

Reference	Synthesis of Fe_3O_4	Experimental method	Contact time	Reducing system
Present work	at $T = 80$ °C	Batch experiments with ≈ 10 mg Fe_3O_4(cr)	480 days[a]	Fe(0), Sn(II) and $Na_2S_2O_4$
Sweeton and Baes (1970)	at $T = 500$ °C	Colum experiments with 45–66 g Fe_3O_4(cr)	4–20 minutes[b]	H_2(g)
Tremaine and LeBlanc (1980)	at $T = 1300$ K	Colum experiments with ≈ 85 g Fe_3O_4(cr)	[c]	H_2(g)

a. thermodynamic equilibrium assumed after repeated measurements with constant [Fe], pH_m and Eh;

b. the authors assumed thermodynamic equilibrium after observing that variations in the flow rate (and thus in the contact time) did not affect [Fe] in the column output;

c. contact time not reported, but similar flow rates as in Sweeton and Baes (1970) were used by these authors.

The low-temperature synthesis of Fe_3O_4(cr) used in the present work is expected to result in a significantly less crystalline material (i.e. with smaller particle size) than with the high-temperature methods used in Sweeton and Baes (1970) and in Tremaine and LeBlanc (1980). Particle size is know to impact the solubility product of a given solid phase, as originally described in the late 60's by Schindler (Schiendler 1967). This effect could possibly contribute to the differences in the solubilities observed in both groups of experimental studies.

Sweeton, Baes, Tremain and LeBlanc suggested that equilibrium conditions might be prevented in solubility experiments conducted with Fe_3O_4(cr) at low temperatures (*e.g.* 25 °C). Such argumentation was also reflected in the NEA-TDB book dedicated to Fe. We consider that such statement may apply to the column experiments involving very short contact times as used by these author, but we believe that does not apply to our experimental set-up. Hence, we consider that the very long contact times allowed in the present study (480 days) ensure approriate thermodynamic equilibrium, as also supported by the constant [Fe], pH_m and E_h measurements after a given time in our experiments. Some figures showing the time-dependency of [Fe] are provided in the Annex for several pH_m and

for three reducing systems evaluated (Fe(0), Sn(II) and $Na_2S_2O_4$) (see Figure A1-6 in Appendix 1). Our previous experience with solubility experiments with transition metals (e.g. Ni(II), see chapter 3.3 of this report) or solid phases involving mixed oxidation states (e.g. Pu(IV) + Pu(V), see Neck et al. 2007) further support that 480 days suffice to achieve thermodynamic equilibrium. Further insights on the equilibrium conditions in our solubility studies are provided in the following section in the context of the discussion of Fe(II) hydrolysis.

The discussion on the solubility of Fe_3O_4(cr) is of high relevance in the context of SFR. Under repository conditions, magnetite is expected to form as secondary phase as a result of the anoxic corrosion of Fe. Thermodynamic data selected in most databases for Fe_3O_4(cr) correspond to very crystalline solid phases synthesized at very high temperatures, and have been investigated in thermochemical, solid-state, studies. Such solid phases and conditions are not representative of the magnetite to be expected in SFR. Less crystalline phases as the one investigated in the present work will expectedly be reponsible of controlling the solubility of Fe in the system. A less crystalline magnetite with greater solubility product will have the following impact in the corresponding thermodynamic calculations:

- The redox borderline defined by magnetite and Fe(III) solid phases will move towards more reducing conditions (*ca.* 1 pe unit, compared with calculations using current thermodynamic data).
- Concentration of Fe(II) in solution will increase about 1 log-unit, compared with calculations using current thermodynamic data.

Table 3-1 shows a good agreement between the first and second Fe(II) hydrolysis constant determined in the present work and thermodynamic data selected for these species in the main thermodynamic compilations and databases. We note that the thermodynamic data selected for these species is based upon a combination of solubility and potentiometric data in the case of $FeOH^+$ (Hedström 1953, Gayer and Woontner 1956, Takashi and Posey 1967, Ehrenfreund and Leibenguth 1970, Sweeton and Baes 1970, Mesmer 1971, Johnson and Bauman 1978, Tremaine and LeBlanc 1980). The good agreement obtained for these hydrolysis constants indicates that, although our study deals with a significantly less crystalline magnetite, this solid phase provides us a sufficiently accurate basis to properly characterize these equilibrium reactions at $T = 22$ °C.

The case of $Fe(OH)_3^-$ requires a more in-depth discussion, with a detailed analysis of the original experimental data used to derive equilibrium constants selected in the different databases under discussion. The value of log $*\beta^\circ_{(1,3)}$ determined in the present study is by far the smallest of all those summarized in Table 3-1, but we note also relevant discrepancies between the third hydrolysis constant proposed by Baes and Mesmer (1976), and that selected by Chivot (2004) and later included in Thermochimie TDB.

The value of log $*\beta^\circ_{(1,3)} = -(31 \pm 1.5)$ selected by Baes and Mesmer (1976) is the average of log $*\beta^\circ_{(1,3)} = -29.4$ reported in Sweeton and Baes (1970) and the value of log $*\beta^\circ_{(1,3)} = -31.9$ reported in a solubility study with $Fe(OH)_2$(s) (Gayer and Woontner 1956). As discussed in Tremaine and LeBlanc (1980) and further agreed by the NEA–TDB reviewers, the value of log $*\beta^\circ_{(1,3)}$ reported by Sweeton and Baes is very likely flawed by the presence of $Fe^{III}(OH)_4^-$, expected to form at elevated temperatures in the hyperalkaline range of their experiments. The formation of this Fe(III) species was not accounted for by these authors, which expectedly resulted in a significant overestimation of the third hydrolysis constant of Fe(II). The equilibrium constant reported by Sweeton and Baes (1970) should therefore be omitted in the selection of log $*\beta^\circ_{(1,3)}$.

The value of log $*\beta^\circ_{(1,3)}$ reported by Gayer and Woontner (1956) was also the basis for the equilibrium constant selected by Chivot (2004), and accordingly by Thermochimie. Gayer and Woontner did not characterize the solid phase controlling the solubility, but rather assumed the only presence of $Fe(OH)_2$(s). Although not clearly stated in the experimental description, experiments were likely performed in N_2 atmosphere but absence of any reducing chemical. Batch samples were stirred for seven days, and then allowed to settle for 3 to 5 days before proceeding to the quantification of uranium concentration in solution. In these conditions, we consider that both oxidation and presence of colloids can not be disregarded. We consider that the relevant shortcomings described above represent an important limitation for considering these data for a sound thermodynamic selection.

As discussed by the NEA reviewers, the solubility study with Fe_3O_4(cr) (at T = 100–300 °C) by Tremaine and LeBlanc can be considered valid also in the hyperalkaline pH range. In contrast to Sweeton and Baes (1970), these authors did consider the formation of $Fe^{III}(OH)_4^-$ in the interpretation of their solubility under hyperalkaline conditions. The value of log $*K°_{s,3}$ extrapolated by these authors to T = 25 °C (–22.4), is again significantly lower than log $*K°_{s,3}$ = –(19.9 ± 0.4) determined in the present work using a magnetite synthesized at T = 80 °C. However, when combining the log $*K°_{s,3}$ reported in Tremaine and LeBlance with log $*K°_{s,0}$ = 11.0 reported by the same authors at T = 25 °C , we obtain a value for the third hydrolysis constant of Fe(II) log $*\beta°_{(1,3)}$ = –33.4 which is in moderate agreement with the constant obtained in the present work, log $*\beta°_{(1,3)}$ = –(32.8 ± 0.4). Considering the fact that the value reported by Tremaine and LeBlanc has been extrapolated from solubility studies at T ≥ 100 °C, we consider our value determined at T = 22 °C a more accurate estimate of the third hydrolysis constant of Fe(II). We note that our value is about one order of magnitude smaller than log $*\beta°_{(1,3)}$ selected in some thermodynamic compilations and databases (Baes and Mesmer, Chivot, Thermochimie), and thus that the formation of anionic hydrolysis species of Fe(II) will be shifted (about 1 pH-units) towards more alkaline conditions (pK_3 = 12.2 as determined in the present work).

3.1.4 Conclusions

The solubility of α-Fe_3O_4 in dilute NaCl-NaOH aqueous systems has been investigated at T = 22 °C in the pH_m range 8-13 and under reducing conditions covering the (pe + pH_m) range 0 to 6. Solubility experiments have been complemented with extensive solid phase characterization.

- Solubility studies conducted at T = 22 °C under reducing conditions provide a sound basis for the thermodynamic interpretation of the reductive dissolution of magnetite and corresponding hydrolysis of Fe(II).
- Solubility constant of magnetite derived in the present study from solubility experiments at T = 22 °C is significantly higher than values available in current thermodynamic databases, derived from thermochemical studies.
- First and second hydrolysis constants of Fe(II) determined in present study are in good agreement with previous solubility and potentiometric studies.
- Relevant differences arise with third hydrolysis constant of Fe(II) selected in most TDB. Differences can be rationalized in terms of diffences in experimental approach and interpretation of chemical system.
- Our dataset provides (to our understanding) the most complete thermodynamic study available to date for magnetite and Fe(II) solution chemistry under conditions (pH, pe, T) relevant for repository systems in general and for SFR in particular.
- New thermodynamic data derived in present work results in a modified redox borderline defined by magnetite and Fe(III) solid phases (moving towards more reducing conditions) and an increased concentration of Fe(II) in solution.

3.2 Study of the redox state of Pu, U and Tc under highly alkaline conditions and in the presence of iron and its anaerobic corrosion products

3.2.1 Introduction

Magnetite, Fe_3O_4(cr), has been identified as one of the main products resulting from the anoxic corrosion of metallic iron and steel. Chapter 3.1 of this report was dedicated to characterize the behaviour of this solid phase in the reducing conditions expected in the SFR repository. Systematic solubility experiments in combination with a comprehensive solid phase characterization allowed deriving a thermodynamic model including the solubility product of Fe_3O_4(cr) and the hydrolysis of Fe(II) in the hyperalkaline conditions relevant in cementitious systems. However, besides the

improved knowledge on the chemical behaviour of this system under conditions representing thermodynamic equilibrium, the question of kinetics and redox equilibrium / disequilibrium is particularly relevant for electron transfer processes in heterogeneous systems. This affects some key redox-sensitive radionuclides (actinides and fissions products) of relevance in the context of nuclear waste disposal: Pu(III)/Pu(IV), U(IV)/U(VI) and Tc(IV)/Tc(VII).

The determination of the response of the redox sensitive radionuclides to the evolution of the system containing large amounts of iron and concrete is fundamental to the performance assessment of SFR. Redox transitions in the hyperalkaline pH range of the radionuclides chosen in this study (Pu(III) → Pu(IV) at pH+pe ~ –1, U(IV) → U(VI) at pH+pe ~ +2, Tc(IV) → Tc(VII) at pH+pe ~ +6) strategically cover the field of stability of the system Fe(0)/Fe(II)/Fe_3O_4, and thus are expected to provide a key understanding on the interaction of the waste with Fe corrosion products under repository conditions.

3.2.2 Experimental part and results

All experiments were performed at $T = (22 \pm 2)$ °C under inert gas (Ar) atmosphere gloveboxes ($O_2 < 5$ ppm). Batch solubility experiments were performed from undersaturation with a hydrothermally prepared α-Fe_3O_4(cr) (Schwertmann and Cornell 2000) (see further details in Section 3.1.2).

Independent experiments were prepared at $pH_m \approx 9$ and $pH_m = 12.8$ in 0.1 M NaCl-NaOH solutions. The solid to liquid ratio was S/L = 2 g/L. Four different redox systems were defined. Additional experimental details are provided in Table 3-4.

i. α-Fe_3O_4(cr) + RN,

ii. α-Fe_3O_4(cr) + Fe(cr) + RN,

iii. α-Fe_3O_4(cr) + 0.01 M $SnCl_2$ + RN and

iv. α-Fe_3O_4(cr) + 0.01 M $Na_2S_2O_4$ + RN.

Table 3-4. Summary of the experimental conditions for the redox experiments with Tc, U and Pu in the presence of Fe_3O_4(cr), Fe_3O_4(cr) + Fe(0), Fe_3O_4(cr) + Sn(II) and Fe_3O_4(cr) + $Na_2S_2O_4$.

Radionuclide (RN)	Fe_3O_4(cr)	Fe_3O_4(cr) + Fe(0)	Fe_3O_4(cr) + $SnCl_2$	Fe_3O_4(cr) + $Na_2S_2O_4$
Tc(VII) [3×10^{-5} M]	pH_m~9 and pH_m =12.8 (V=20mL)	pH_m~9 and pH_m =12.8 (V=20mL)	pH_m~9 and pH_m =12.8 (V=20mL)	pH_m~9 and pH_m =12.8 (V=20mL)
U(VI) [3×10^{-5} M]	pH_m~9 and pH_m =12.8 (V=20mL)	pH_m~9 and pH_m =12.8 (V=20mL)	pH_m~9 and pH_m =12.8 (V=20mL)	pH_m~9 and pH_m =12.8 (V=20mL)
Pu(V) [3×10^{-5} M]	pH_m~9 and pH_m =12.8 (V=10mL)	pH_m~9 and pH_m =12.8 (V=10mL)	pH_m~9 and pH_m =12.8 (V=10mL)	pH_m~9 and pH_m =12.8 (V=10mL)

A total of 24 samples were prepared in the corresponding background solutions either in 0.1 M NaCl (pH_m ~ 9) or 0.1 M NaOH ($pH_m = 12.8$). In all cases $[RN]_0$ was 3×10^{-5} M. The more soluble redox states of these radionuclides were chosen for the sample preparation: Tc(VII), U(VI) and Pu(V). In the latter case, the corresponding stock solution was prepared electrochemically by reduction of a Pu(VI) solution under acidic conditions. The redox purity of Pu(V) was confirmed by UV-vis/NIR.

Liquid Scintillation Counting (LSC) for Tc-99 and Pu-242 and Inductively Coupled Plasma-Mass Spectrometry (ICP-MS) for U-238 were used for the quantification of total radionuclide concentration after 10 kD ultrafiltration. The redox behaviour of these radionuclides in the aqueous phase and on the surface of magnetite was followed in combination with pH and Eh data collected for the same systems. Redox speciation in the aqueous phase was investigated by solvent extraction techniques for the case of Pu.

Selected Fe solid phases containing Tc, U and Pu were characterized using several techniques available at KIT-INE:

- XPS was used for the characterization of the redox state of Tc, U and Pu on the surface of Fe_3O_4(cr). XPS is a surface-sensitive technique, and provides information at a depth of a few nm.
- XANES / EXAFS provided information on the redox speciation of Pu in Fe_3O_4(cr). XAFS techniques provide information on the bulk of solid phases.

The results obtained by solid phase characterization are not discussed in the main text of this report, but are summarized in the Appendix 2.

3.2.3 Experimental results for Tc(IV)/Tc(VII)

Figure 3-7 shows the pH_m and E_h (pE) values measured for Fe_3O_4(cr), Fe_3O_4(cr) + Fe(0), Fe_3O_4(cr) + Sn(II) and Fe_3O_4(cr) + $Na_2S_2O_4$ systems in the presence of Tc. Experimental data are plotted in the Pourbaix diagram of Tc calculated using thermodynamic data selection in ThermoChimie database. Data previously reported in Kobayashi et al. (2013) and Yalçıntaş et al. (2016) for analogous systems but using a more amorphous magnetite are appended to the figure for comparison. Figure 1b shows [Tc] measured in Fe_3O_4(cr), Fe_3O_4(cr) + Fe(0), Fe_3O_4(cr) + Sn(II) and Fe_3O_4(cr) + $Na_2S_2O_4$ systems at the two pH_m-values investigated in the present work (≈ 9 and 12.8). The figure includes the solubility curve of $TcO_2 \times 1.63H_2O$(am) calculated using thermodynamic data selected in ThermoChimie. As in Figure 3-7a, analogous data reported in Kobayashi et al. (2013) and Yalçıntaş et al. (2016) are included for comparison purposes.

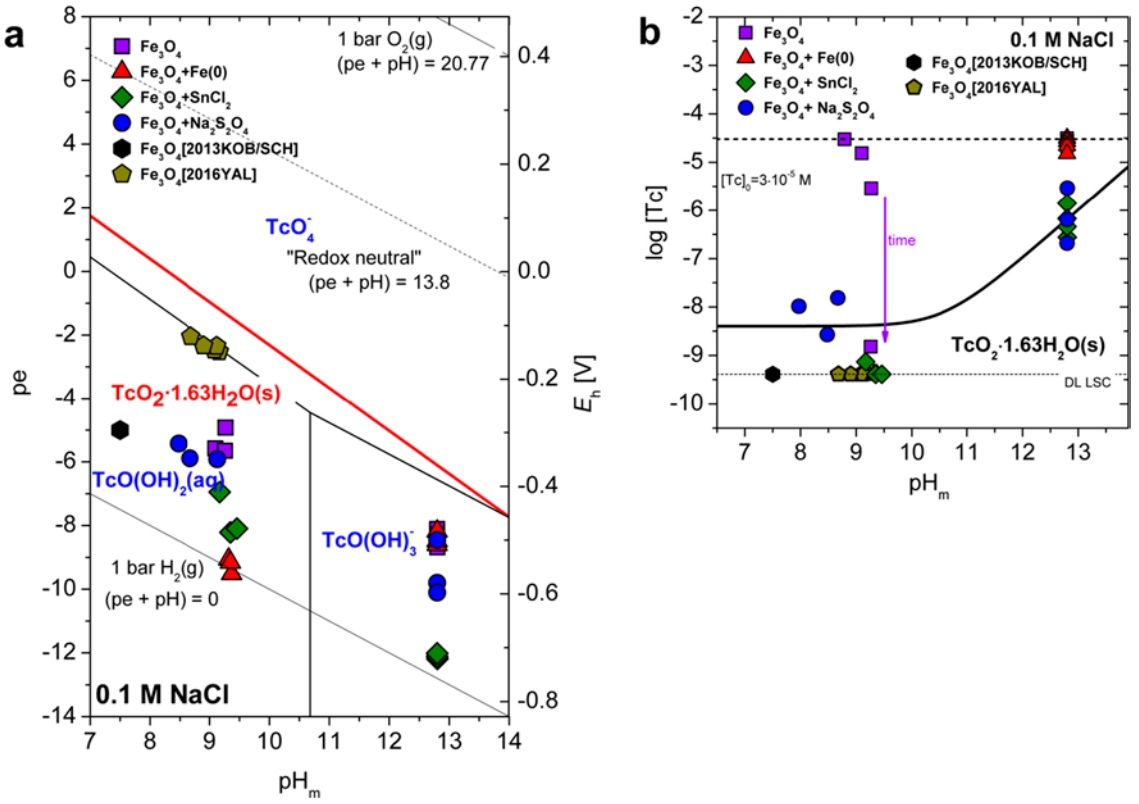

Figure 3-7. *Experimental pH_m, E_h and [Tc] data for the Tc(IV) / Tc(VII) system obtained at contact time $t \leq 275$ days. a: Predominance diagram calculated for 0.1 M NaCl-NaOH systems with [Tc] = 3×10^{-5} M using Tc thermodynamic data selected in Thermochimie; black lines corresponding to borderlines between Tc aqueous species; red line corresponding to borderline including also solid phases. b. Solubility curve of $TcO_2 \times 1.63H_2O$(am) calculated for 0.1 M NaCl-NaOH systems using Tc thermodynamic data selected in Thermochimie.*

Figure 3-7 shows that all samples prepared in the presence of Tc are in the stability field of Tc(IV), and thus that the reduction of Tc(VIII) to Tc(IV) would occur. Among all reducing systems evaluated, the one with magnetite in the absence of additional reducing chemicals (Sn(II), Fe(0), $Na_2S_2O_4$) results always in higher E_h values than the ones containing redox buffers. The presence of Fe(0) promotes very reducing conditions at $pH_m \approx 9$ (close / at the border of water reduction), but results only in moderate reducing E_h values at $pH_m = 12.8$. As discussed in the previous chapter, this effect is expected due to the passivation of the surface of Fe(0).

Due to the low solubility of $TcO_2 \times 1.63H_2O$(am) and the strong sorption of Tc(IV), the reduction of Tc(VII) to Tc(IV) should result in a significant decrease of the initial Tc concentration ($[Tc(VII)]_0 = 3 \times 10^{-5}$ M). At $pH_m \approx 9$, such a decrease is observed for all evaluated systems, although Fe_3O_4(cr) in the absence of other reducing chemicals (purple squares in Figure 3-7 a) and b) reaches log [Tc] ≈ –9 only at $t = 275$ days. In hyperalkaline systems with $pH_m = 12.8$, the concentration of Tc in the presence of Fe_3O_4(cr) + Sn(II) and Fe_3O_4(cr) + $Na_2S_2O_4$ shows a fast decrease of 1-2 orders of magnitude. On the other hand, the initial concentration of Tc in the presence of Fe_3O_4(cr) and Fe_3O_4(cr) + Fe(0) decreases very slowly, and only ≈ 30 % and ≈ 50 %, respectively, of the total Tc is reduced after a contact time of 275 days. Although kinetics play a very relevant role in the redox chemistry of Tc in the presence of Fe phases (see also Figure 3-8 a) and b), and discussion thereafter), we note that for all those systems were thermodynamic equilibrium has been attained, the final concentration of Tc is in agreement with the calculated solubility of $TcO_2 \times 1.63H_2O$(am). This result suggests that, in the conditions of our study, the concentration of Tc in solution is not controlled by sorption phenomena (onto magnetite) but rather by solubility.

Relevant insights on the reduction kinetics of Tc in Fe systems can be drawn from Figure 3-8:

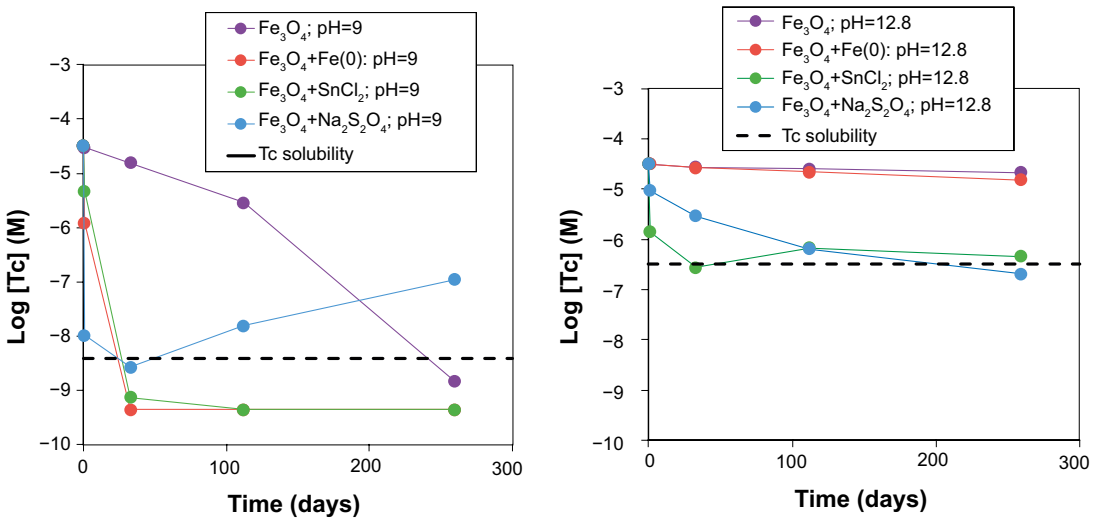

Figure 3-8. *Experimentally measured [Tc] as a function of time in Fe_3O_4(cr), Fe_3O_4(cr) + Fe(0), Fe_3O_4(cr) + Sn(II) and Fe_3O_4(cr) + $Na_2S_2O_4$ systems: a. $pH_m \approx 9$; b. $pH_m = 12.8$. Dashed black lines in the figures correspond to the solubility of $TcO_2 \times 1.63H_2O$(am) calculated for the corresponding pH_m using Tc thermodynamic data selected in Thermochimie.*

$pH_m \approx 9$, Figure 3-8a

- Very fast reduction kinetics are observed at this pH_m, where Fe_3O_4(cr) + Fe(0), Fe_3O_4(cr) + Sn(II) and Fe_3O_4(cr) + $Na_2S_2O_4$ systems reach log [Tc] ≈ –9 (corresponding to the solubility-control by $TcO_2 \times 1.63H_2O$(am)) at $t \leq 30$ days.
- Much longer contact time (≈ 275 days) is required to reach the complete reduction of Tc(VII) in Fe_3O_4(cr). This observation can be rationalized with the fact that Fe_3O_4(cr) is the less reducing of all investigated systems. The driving force for the reduction of Tc(VII) to Tc(IV) (represented as $\Delta pe = pe_{experimental} - pe_{Tc(VII)/Tc(IV)borderline}$) is accordingly the smallest for this system.
- The increase of the concentration of Tc observed after t ≈ 30 days for the system Fe_3O_4(cr) + $Na_2S_2O_4$ is likely related with the known degradation of $Na_2S_2O_4$ in weakly alkaline to acidic systems, with the consequent impact on the solution chemistry of Tc as previously described in Yalçıntaş et al. (2016).

$pH_m = 12.8$, Figure 3-8b

- A fast decrease in [Tc] is observed in Fe_3O_4(cr) + Sn(II) and Fe_3O_4(cr) + $Na_2S_2O_4$ systems. In both systems, the concentration of Tc after attaining equilibrium conditions is in excellent agreement with the solubility limit set by the equilibrium $TcO_2 \times 1.63H_2O(am) + 0.37H_2O(l) \Leftrightarrow TcO(OH)_3^- + H^+$.
- The concentration of Tc decrases very slowly in Fe_3O_4(cr) and Fe_3O_4(cr) + Fe(0). Although complete reduction is expected also for both systems, the driving force represented by $\Delta pe = pe_{experimental} - pe_{Tc(VII)/Tc(IV)borderline}$ is again much smaller for these systems ($\Delta pe \approx 2$) compared to Fe_3O_4(cr) + $Na_2S_2O_4$ ($\Delta pe \approx 4$) and Fe_3O_4(cr) + Sn(II) ($\Delta pe \approx 6$) systems.

Besides the solution chemical data discussed above, XPS results summarized in Appendix A2.2 confirm the predominance of Tc(IV) on the surface of Fe_3O_4(cr) in all evaluated reducing systems.

3.2.4 Experimental results for U(IV)/U(VI)

Figure 3-9a shows the pH and Eh values measured for Fe_3O_4(cr), Fe_3O_4(cr) + Fe(0), Fe_3O_4(cr) + Sn(II) and Fe_3O_4(cr) + $Na_2S_2O_4$ systems in the presence of U. The experimental data are plotted in the Pourbaix diagram of U calculated using thermodynamic data from the ThermoChimie database. Figure 3-9b shows [U] measured in Fe_3O_4(cr), Fe_3O_4(cr) + Fe(0), Fe_3O_4(cr) + Sn(II) and Fe_3O_4(cr) + $Na_2S_2O_4$ systems at the two pH_m-values investigated in the present work (≈ 9 and 12.8). The figure includes the solubility curves of UO_2(am,hyd), $UO_3 \times 2H_2O$(cr) and $Na_2U_2O_7 \times H_2O$(cr) calculated using thermodynamic data selected in ThermoChimie. These solid phases are expected to control the solubility of U(IV) and U(VI), respectively, in the absence of other retention phenomena (*e.g.* sorption).

Figure 3-9a shows that all samples prepared in the presence of U at $pH_m \approx 9$ are in the stability field of U(IV), and thus that the reduction of U(VI) to U(IV) should occur. However, at $pH_m = 12.8$, clear differences arise between the systems in the presence of Fe_3O_4(cr) + Sn(II) and Fe_3O_4(cr) + $Na_2S_2O_4$, and the systems in the presence of Fe_3O_4(cr), Fe_3O_4(cr) + Fe(0). In the first case, E_h measurements confirm highly reducing conditions clearly located in the stability field of U(IV), thus reduction to U(IV) and consequent decrease in concentration to log [U] ≤ –8.5 (solubility limit of UO_2(am, hyd)) should occur. Significantly higher E_h values are measured in Fe_3O_4(cr) and Fe_3O_4(cr) + Fe(0) systems. According with the thermodynamic calculations shown in the Pourbaix diagram in Figure 3-9b, the E_h values measured for these systems at $pH_m = 12.8$ indicate that no (or minor) reduction of U(VI) to U(IV) should be expected. We note however that solubility calculations shown in Figure 3b are subjected to very large uncertainties in the hyperalkaline pH_m-region. This is mostly due to the uncertainties associated to the thermodynamic data available for the U(IV) aqueous species and solid compounds predominating in this pH_m-region:

$$U^{4+} + 4OH^- \Leftrightarrow UO_2(am, hyd) + 2H_2O(l) \quad (3\text{-}8)$$

log $K°$ = (54.5 ± 1.0) (Guillaumont et al. 2003)

$$U^{4+} + 4OH^- \Leftrightarrow U(OH)_4(aq) \quad (3\text{-}9)$$

log $K°$ = (46.0 ± 1.4) (Guillaumont et al. 2003)

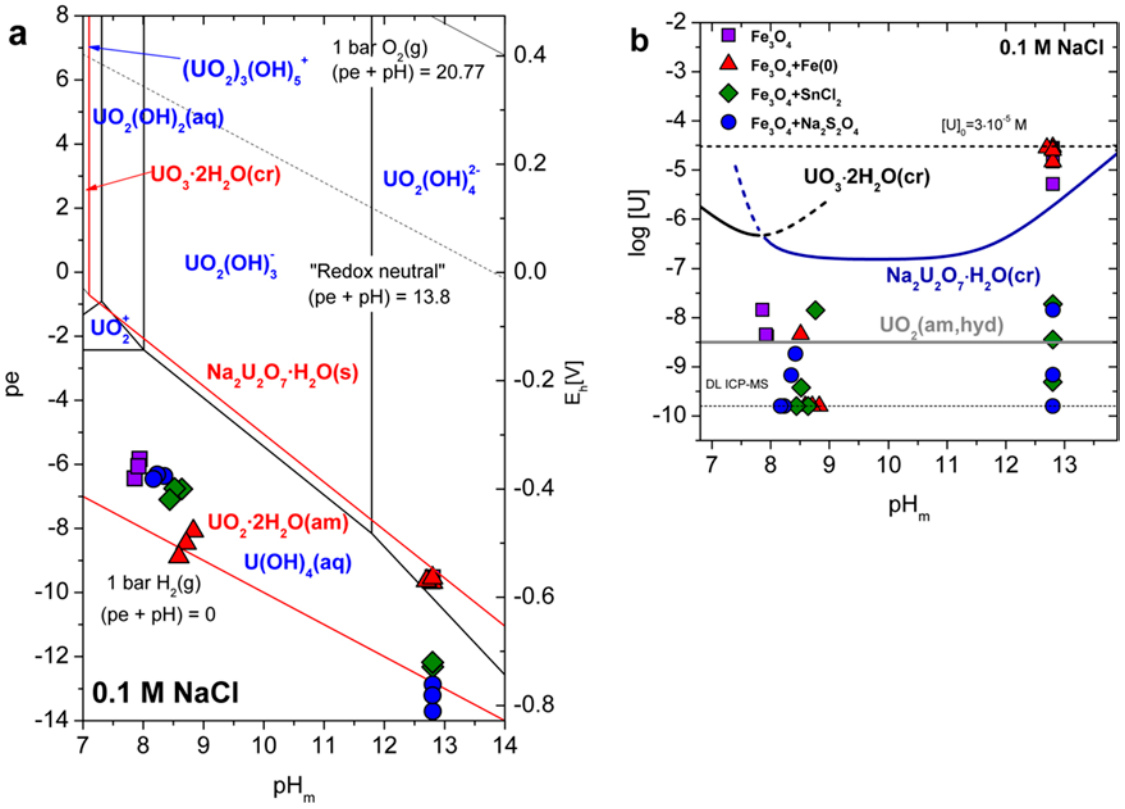

Figure 3-9. *Experimental pH_m, Eh and [U] data for the U(VI) / U(IV) system obtained at contact time $t \leq 275$ days. a: Predominance diagram calculated for 0.1 M NaCl-NaOH systems with [U] = 3×10^{-5} M using U thermodynamic data selected in Thermochimie. Black lines corresponding to borderlines between U aqueous species; red line corresponding to borderline including also solid phases. b. Solubility curves of UO_2(am, hyd), $UO_3 \times 2H_2O$(cr) and $Na_2U_2O_7 \times H_2O$(cr) calculated for 0.1 M NaCl-NaOH systems using U thermodynamic data selected in Thermochimie.*

The results shown in Figure 3-9b shall be then considered as a proof-of-concept for the thermodynamic data available for this system under hyperalkaline pH conditions.

Figure 3-9b shows very low [U] ($\leq 10^{-8}$ M) in all the systems at $pH_m \approx 9$. Similar uranium concentrations are measured at $pH_m = 12.8$ for the systems Fe_3O_4(cr) + Sn(II) and Fe_3O_4(cr) + $Na_2S_2O_4$. On the contrary, the initial concentration of uranium does not decrease (or only very slightly) in Fe_3O_4(cr) and Fe_3O_4(cr) + Fe(0) systems at $pH_m = 12.8$. These observations indicate that U(VI) is reduced in all the systems investigated except Fe_3O_4(cr) and Fe_3O_4(cr) + Fe(0) at $pH_m = 12.8$, in agreement with experimental pH_m and E_h values and thermodynamic calculations shown in Figure 3-9a. Such agreement gives further confidence in the current thermodynamic selection for uranium available in the NEA-TDB, and allows decreasing the uncertainty with regard to the chemical behavior of uranium under hyperalkaline pH_m conditions.

Figure 3-10 show the time dependence of [U] in the investigated reducing systems at $pH_m \approx 9$ and $pH_m = 12.8$, respectively. As in the case of Tc, slightly faster reduction kinetics are observed in weakly alkaline (≈ 50 days) compared to hyperalkaline (≈ 100 days) systems. This is possibly related with a decreased driving force under hyperalkaline conditions, represented by lower $\Delta pe = pe_{experimental} - pe_{U(VI)/U(IV)borderline}$. As discussed above, Figure 3-10 confirms also that no reduction is observed for Fe_3O_4(cr) and Fe_3O_4(cr) + Fe(0) systems at $pH_m = 12.8$. We note that, as a general trend, higher oxidation states tend to be stabilized by hyperalkaline pH_m conditions.

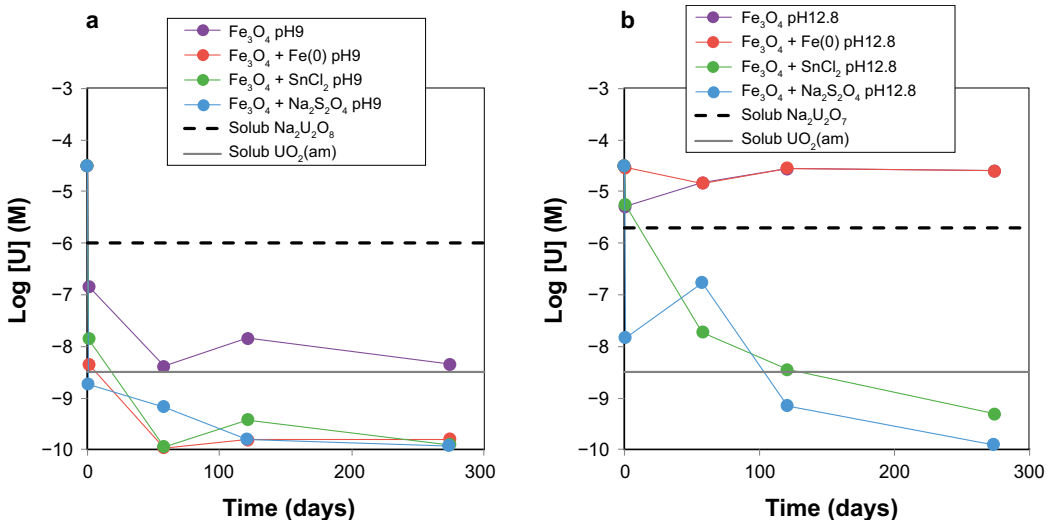

Figure 3-10. *Experimentally measured [U] as a function of time in Fe_3O_4(cr), Fe_3O_4(cr) + Fe(0), Fe_3O_4(cr) + Sn(II) and Fe_3O_4(cr) + $Na_2S_2O_4$ systems: a. $pH_m \approx 9$; b. $pH_m = 12.8$. Dashed black and grey lines in the figures correspond to the solubility of $Na_2U_2O_7 \times H_2O$(cr) and UO_2(am, hyd) respectively, calculated for the corresponding pH_m using U thermodynamic data selected in Thermochimie.*

XPS results summarized in Appendix A2.2 confirm the predominance of U(IV) on the surface of Fe_3O_4(cr) in most of the samples were a drop in [U] was observed. The only exception is observed at $pH_m \approx 9$ for the sample in the presence of Fe_3O_4(cr) in the absence of additional reducing chemicals. In this case, XPS suggest the presence of U(V) and U(VI). The presence of U(V) on the surface of magnetite has been reported previously in the literature (Ilton et al. 2010, Huber et al. 2012). At this point, it remains unclear whether this is a real effect caused by an energetically favored incorporation of U(V) in the structure of magnetite, or rather corresponds to an artifact of the XPS technique. We note that the U(VI) and U(IV) XPS bands are very close in energies, and that the presence or absence of U(V) is strongly dependent on the deconvolution / fitting approach used to evaluate XPS data (see discussion in Huber et al. 2012). Independently of the redox state of U in the magnetite, wet-chemistry data discussed above confirm that [U] at $pH_m \approx 9$ remains very low in all systems.

3.2.5 Experimental results for Pu(III)/Pu(IV)

Figure 3-11 shows the pH and E_h values measured for Fe_3O_4(cr), Fe_3O_4(cr) + Fe(0), Fe_3O_4(cr) + Sn(II) and Fe_3O_4(cr) + $Na_2S_2O_4$ systems in the presence of Pu. Experimental data are plotted in the Pourbaix diagram of Pu calculated using thermodynamic data selection in ThermoChimie database. Figure 3-11b shows [Pu] measured in Fe_3O_4(cr), Fe_3O_4(cr) + Fe(0), Fe_3O_4(cr) + Sn(II) and Fe_3O_4(cr) + $Na_2S_2O_4$ systems at the two pH_m-values investigated in the present work (≈ 9 and 12.8). The figure includes the solubility curves of PuO_2(am, hyd) and $Pu(OH)_3$(am), as well as the solubility curve corresponding to the reductive dissolution of PuO_2(am, hyd) at $(pe + pH_m) = 2$ (reaction (11) and chemical equations (3-11) and (3-12)):

$$Pu(IV)O_2(am,hyd) + (1+n)\,H^+ + e^- \Leftrightarrow Pu(III)(OH)_{3-n}^{n+} + (n-1)\,H_2O(l) \quad (3\text{-}10)$$

$$\log {}^*K^\circ_{IVs/III,(3-n)} = \log {}^*K'_{IVs/III,(3-n)} + \log \gamma_{Pu(III)(OH)_{3-n}^{n+}} + pe + (1+n)\log a_w - (1+n)\log \gamma_{H^+} \quad (3\text{-}11)$$

$$\log {}^*K'_{IVs/III,(3-n)} = \log [Pu(III)(OH)_{3-n}^{n+}] + (1+n)\,pH_m \quad (3\text{-}12)$$

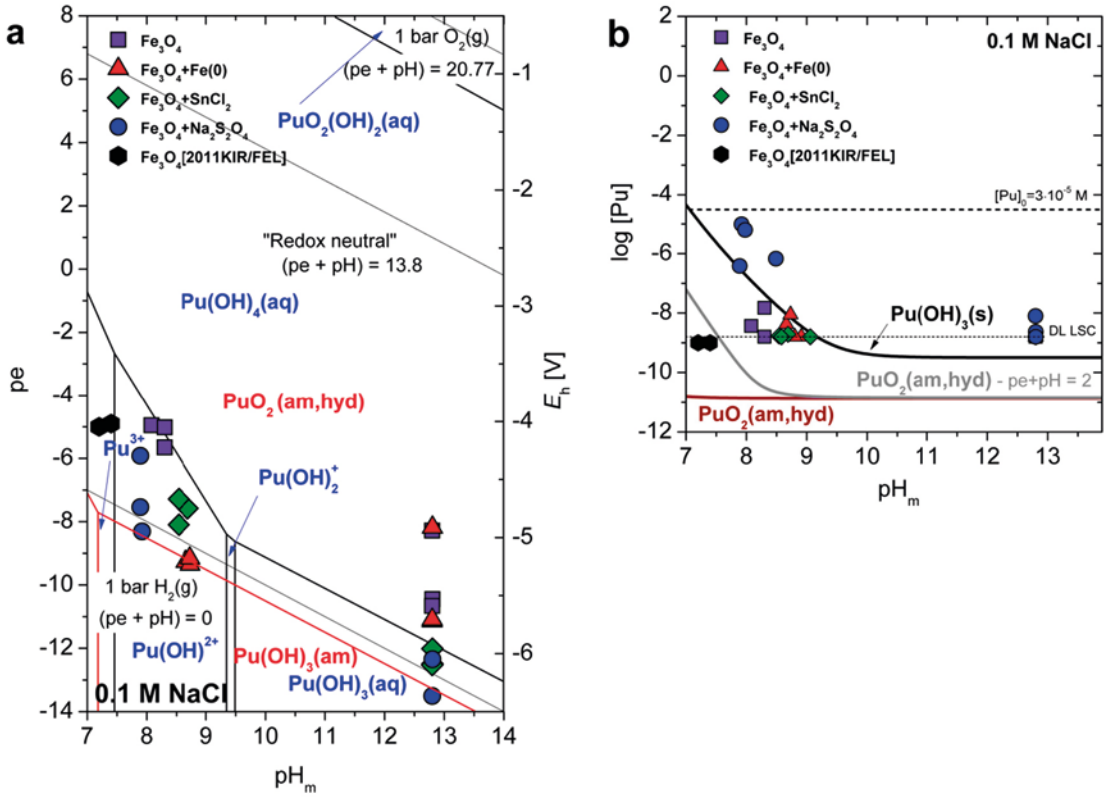

Figure 3-11. *Experimental pH_m, E_h and [Pu] data for the Pu(IV) / Pu(III) system obtained at contact time $t \leq 275$ days. a: Predominance diagram calculated for 0.1 M NaCl-NaOH systems with [Pu] = 3×10^{-5} M using Pu thermodynamic data selected in Thermochimie. Black lines corresponding to borderlines between Pu aqueous species; red line corresponding to borderline including also solid phases. b. Solubility curves of PuO_2(am, hyd) and $Pu(OH)_3$(am), as well as the solubility curve corresponding to the reductive dissolution of PuO_2(am, hyd) at (pe + pH_m) = 2 calculated for 0.1 M NaCl-NaOH systems using U thermodynamic data selected in Thermochimie.*

Relevant uncertainties affect the thermodynamic data available for Pu(III) and Pu(IV) under reducing alkaline conditions, which result in a rather ill-defined Pu(IV) / Pu(III) redox boundary in these conditions (see discussion in Tasi et al. 2018). Figure 3-11a shows that all E_h measurements in the investigated magnetite systems at $pH_m \approx 9$ are in the stability field of $Pu(III)_{aq}$ and PuO_2(am, hyd) (if controlled by solubility). The figure shows also that $Pu(III)_{aq}$ may prevail at $pH_m = 12.8$ in Fe_3O_4(cr) + Sn(II) and Fe_3O_4(cr) + $Na_2S_2O_4$ systems, whereas $Pu(IV)_{aq}$ is expected to be the predominant redox state of Pu Fe_3O_4(cr) and Fe_3O_4(cr) + Fe(0) systems at this pH_m. In these hyperalkaline pH_m conditions, PuO_2(am, hyd) is the Pu solid phase expected to control the solubility of Pu in all investigated systems. We note however that the redox borderline between PuO_2(am, hyd) and $Pu(OH)_3$(am) remains ill-defined as a result of the large uncertainties in the available thermodynamic data:

$$PuO_2(am,hyd) + H_2O(l) + H^+ + e^- \Leftrightarrow Pu(OH)_3(am) \quad (3\text{-}13)$$

$$\log {}^*K^\circ_{IVs/IIIs} = pH + pe - \log a_w = -(0.4 \pm 1.6) \quad (3\text{-}14)$$

Recent investigations with Pu solubility under reducing alkaline conditions indicated the possible co-existence of Pu(III) and Pu(IV) in the solid phases controlling the solubility of Pu in these conditions (Tasi et al. 2018). So far, it remains unclear whether this involves the co-existence of PuO_2(am, hyd) and $Pu(OH)_3$(am), the formation of a sub-stoichiometric solid solution in the form of PuO_{2-x}(am, hyd), or to a transient state in the process towards a final conversion to PuO_2(am, hyd) or $Pu(OH)_3$(am).

Figure 3-11 shows very low concentrations of Pu (close to, or at the detection limit of LSC) for all investigated systems except Fe_3O_4(cr) + $Na_2S_2O_4$ at $pH_m \approx 8$. The latter sample gives log [Pu] ≈ –(5.5 ± 0.6), which would indicate a solubility control by the equilibrium $Pu(OH)_3(am) \Leftrightarrow Pu(III)_{aq}$. For this sample, plutonium redox speciation of Pu in the aqueous phase was investigated by solvent extraction. This method indicated that 95 % of Pu is in the form of Pu(III), in good agreement with thermodynamic calculations shown in Figure 3-11a and b.

No definitive conclusions on the process controlling [Pu] in solution can be drawn for all other systems. Experimental observations are consistent with either a solubility control by PuO_2(am, hyd) $\Leftrightarrow Pu(IV)_{aq}$, a reductive dissolution PuO_2(am, hyd) + $e^- \Leftrightarrow Pu(III)_{aq}$ or, in some cases, $Pu(OH)_3(am) \Leftrightarrow Pu(III)_{aq}$. The role of sorption cannot be ruled out either from the available data. Indeed, our observations based on solution chemistry are consistent with previous findings by Kirsch et al. (2011), who reported very low concentrations of $[Pu]_{aq}$ in the presence of magnetite at $pH_m \approx 7$ (see Figure 3-11a and b) and demonstrated by EXAFS that this was mostly due to the formation of a very stable Pu(III) surface complex on magnetite.

XPS and XAFS data summarized in Appendix A2.3 confirm the presence of both Pu(III) and Pu(IV) in the solid phases retrieved from Fe_3O_4(cr) + $Na_2S_2O_4$ and Fe_3O_4(cr) + Sn(II) systems at $pH_m \approx 8$–9, and from Fe_3O_4(cr) + Sn(II) systems at $pH_m = 12.8$. These results are in line with the recent study by Tasi and co-workers (Tasi et al. 2018), who reported the co-existence of Pu(III) and Pu(IV) in the solid phases controlling the solubility of Pu under alkaline to hyperalkaline systems in the presence of Sn(II).

Figure 3-12 show a fast decrease of the initial Pu concentration for all the investigated systems. This confirms that the reduction of Pu(V) to either Pu(IV) or Pu(III) is significantly faster than in the case of Tc or U. We note that Pu(V) is only stable under moderately oxidizing conditions and near-neutral pH_m, and thus the driving force for its reductions is much stronger than in the case of U(VI) or Tc(VII).

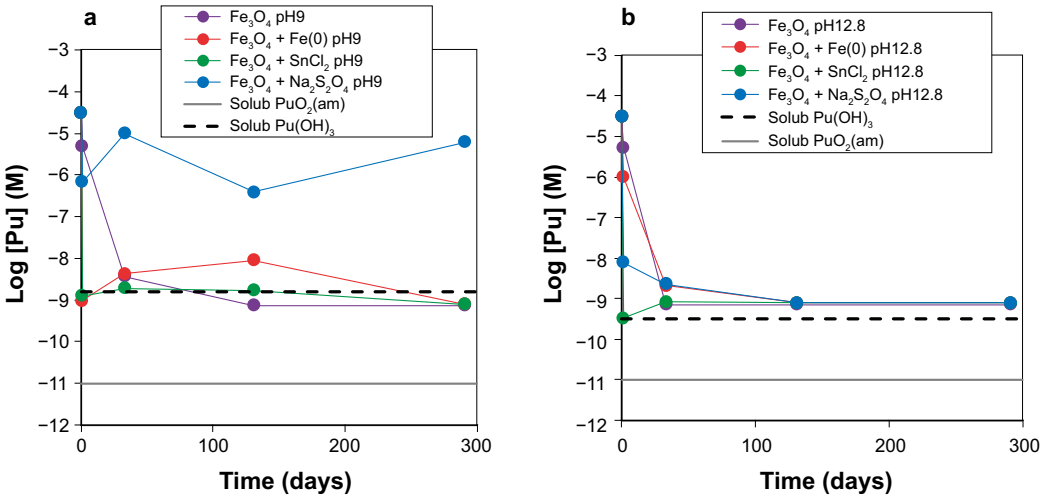

Figure 3-12. *Experimentally measured [Pu] as a function of time in Fe_3O_4(cr), Fe_3O_4(cr) + Fe(0), Fe_3O_4(cr) + Sn(II) and Fe_3O_4(cr) + $Na_2S_2O_4$ systems: a. $pH_m \approx 9$; b. $pH_m = 12.8$. Continuous grey and dashed black lines in the figures correspond to the solubility of PuO_2(am, hyd) $\Leftrightarrow Pu(IV)_{aq}$, the reductive dissolution PuO_2(am, hyd) + $e^- \Leftrightarrow Pu(III)_{aq}$ or to $Pu(OH)_3(am) \Leftrightarrow Pu(III)_{aq}$ (at (pe + pH_m) = 2), calculated for the corresponding pH_m using Pu thermodynamic data selected in Thermochimie.*

3.2.6 Conclusions

- pH and E_h defined in cementitious systems in presence of magnetite and other Fe corrosion products are master parameters governing the chemical behavior of redox sensitive radionuclides.
- Experimental E_h and [U] measurements in combination with thermodynamic calculations suggest that magnetite does not reduce U(VI) in hyperalkaline conditions (pH_m = 12.8).
- Although the reduction of Tc(VII) to Tc(IV) is observed in all investigated systems, the formation of anionic hydrolysis species of Tc(IV) in hyperalkaline conditions enhances [Tc] up to $\approx 10^{-6}$ M.
- Very low Pu concentrations are observed in all investigated systems, except at $pH_m \approx 8$ in the presence of Fe_3O_4(cr) + Sn(II), where the solubility equilibrium $Pu(OH)_3(am) \Leftrightarrow Pu(III)_{aq}$ imposes [Pu] $\approx 10^{-6}$ M.
- Kinetics importantly affect those redox transformations involving several electrons and re-arrangement of radionuclide structure (*e.g.* Tc(VII)=>Tc(IV) or U(VI)=>U(IV)).
- Kinetics have a stronger impact on redox transformations in hyperalkaline pH systems, where higher oxidations states tend to be stabilized (*e.g.* Tc(VII) and U(VI)) .

3.3 Study of thermodynamic model of Ni(II) solubility, hydrolysis and complex formation with ISA

3.3.1 Introduction

The radionuclides ^{59}Ni ($t_{1/2} = 7.5 \times 10^4$ a) and ^{63}Ni ($t_{1/2}$ = 96 a) are activation products of stable isotopes of Ni, Zn and Co. They are removed from the reactor coolant by ion-exchange resins, and disposed of in SFR (Lindgren et al. 2007). According to the long-term safety analysis (SKB 2008), both isotopes are important contributors to the radiotoxicity of the wastes in SFR. ^{59}Ni could be found in the austenitic steel in the reactor, activation of Ni dissolved in the coolant and in corrosion particles deposited on the core. In the case of ^{63}Ni, sources are austenitic steels in the core. Stainless steel contents around 10 % of Ni and in Inconel 50–75 %. Furthermore, Ni is also found as an impurity in Zircaloy (approx. 40 ppm) and in reactor fuel (approx. 20 ppm) (Lindgren et al. 2007).

Nickel is a non-redox sensitive element and representative of divalent cations. Almkvist and Gordon have estimated the inventory of radionuclides expected in the different packages of the SFR repository (Almkvist and Gordon 2007, Fanger et al. 2001). The maximum concentration of Ni expected in the different vauls calculated using data from Almkvist and Gordon (2007) and Fanger et al. (2001) are: 1.4×10^{-6} M for BMA, 2.5×10^{-5} M for SILO and 2.5×10^{-7} M for BTF.

Low- and intermediate level radioactive waste contains both organic and inorganic ligands. The main sources of organic ligands present in SFR are decontamination agents at the nuclear power plant (EDTA, DTPA, NTA, among others), degradation products of bitumen, ion exchange resins, cellulose and cement additives, as well as degradation of other high molecular weight organics such as nylon, polystyrene or polyvinylchloride. An accurate knowledge of radionuclide interaction with these organic ligands is important because of the impact of complexation on radionuclide solubility and sorption, and by extension on the assessment of the source term.

Under highly alkaline cement porewaters, cellulose is slowly degraded to low molecular weights compounds. The final products depend on porewater composition, although in the presence of Ca^{2+}, the formation of α-isosaccharinic acid (ISA) is favored (Bradbury and Van Loon 1997, Van Loon and Glaus 1997, 1998). ISA is also considered as one of the main representatives of polyhydroxy carboxylic acids expected in cementitious repositories.

The amount of organic ligands present in the waste was formerly estimated by Fanger and co-workers (Fanger et al. 2001), who calculated organic ligands concentrations in the different repository packages (BMA, SILO and BTF). Using data reported in Fanger et al. (2001), it is possible to calculate the maximum concentration of organic ligands expected to be present in the waste packages of each sub-system. The maximum concentration of ISA expected in the different vaults calculated using data from Fanger and co-autors are: 5.4×10^{-2} M for BMA, 5.5×10^{-2} M for SILO and 1.0×10^{-6} M for BTF.

The effect of organic substances on the mobility of radionuclides must be investigated as part of safety assessment of a deep underground repository for radioactive waste (Glaus et al. 1999).

The reader is referred to the peer-review publication González-Siso et al. (2018) for more extensive / detailed discussion of the experimental results obtained in the present work in combination with data reported in previous studies.

3.3.2 Experimental part and results

All solutions were prepared with purified water (Milli-Q academic, Millipore) and purged for two hours with Ar before use to remove traces of O_2 and CO_2. The solution chemistry of Ni(II) is characterized by a moderate hydrolysis and the formation of the sparingly soluble $Ni(OH)_2(s)$ under alkaline to hyperalkaline pH conditions. The solubility of $Ni(OH)_2(s)$ has been investigated at $T = 22 \pm 2$ °C under inert gas (Ar) atmosphere ($O_2 < 5$ ppm). Batch solubility experiments were performed from undersaturation conditions with a commercial $Ni(OH)_2(s)$. Independent batch samples were prepared using 20 mg $Ni(OH)_2(s)$ in 20 mL per experiment. Experiments were performed in 0.5 and 3.0 M NaCl–NaOH with $7.5 \le pH_m \le 13$ (with $pH_m = -\log {}_mH^+$). mNi and pH_m were monitored at regular time intervals for up to 310 days. Dissolved mNi was measured by ICP–MS after 10 kD ultrafiltration. NaISA(s) was synthesized in the present study from the alkaline degradation of α-lactose hydrate (Sigma Aldrich) following the approach summarized in Appendix A3.1.

Solubility and hydrolysis of Ni(II) in the absence of ISA

The experimental details:

- Undersaturation solubility experiments with $Ni(OH)_2(cr)$.
  - *ca.* 20 mg solid per batch.
- 0.5/3.0 M NaCl–NaOH and 0.5 M $NaNO_3$; $7.5 \le pH_m \le 13$.

A total of 32 independent batch samples were prepared using 20 mg of $Ni(OH)_2(s)$ in 20 mL per experiment. Experiments were performed at constant ionic strength in 0.5 and 3.0 M NaCl–NaOH solutions with $7.5 \le pH_m \le 13$. One additional solubility sample was prepared in 0.5 M $NaNO_3$ with $pH_m \ge 9.3$ to assess the possible role of Ni(II)–Cl aqueous complexes in 0.5 M NaCl systems. [Ni] and pH_m were monitored at regular time intervals for up to 310 days.

Solubility and hydrolysis of Ni(II) in the presence of ISA

The experimental details:

- Undersaturation solubility experiments with $Ni(OH)_2(cr)$.
- *ca.* 20 mg solid per batch.
- [ISA]= 0.01, 0.1 and 0.2 M.
- 0.5 M NaCl–NaOH; $9 \le pH_m \le 13$.

Ni(II) solubility experiments in the presence of NaISA were conducted using the same solid phase and experimental approach as in the absence of NaISA. A total of 28 independent batch samples were prepared in 0.5 M NaCl–NaOH–NaISA solutions with $0.01\ M \le [ISA-] \le 0.2\ M$ and $9 \le pH_m \le 13$. [Ni] and pH_m were monitored at regular time intervals for up to 290 days

3.3.3 Experimental results in the absence of ISA

Solubility of Ni(II) in NaCl and $NaNO_3$ systems

Ni(II) experimental solubility data determined in NaCl–NaOH and $NaNO_3$ solutions in the absence of ISA are shown in Figure 3-13. Only values of $\log_{10}$ [Ni] quantified above the detection limit of ICP–MS for the given salt concentration are provided in the Figure. Note that in 3.0 M NaCl systems with $pH_m \ge 10.5$, all values of $\log_{10}$ [Ni] fell below the calculated detection limit and thus have been omitted. Solid lines in Figure 3-13 correspond to the solubility of b-$Ni(OH)_2(cr)$ calculated using thermodynamic data derived in González-Siso et al. (2018), selected in NEA–TDB (Gamsjäger et al. 2005), ThermoChimie (Giffaut et al. 2014) and reported in the review by Brown and Ekberg (2016) for a microcrystalline phase.

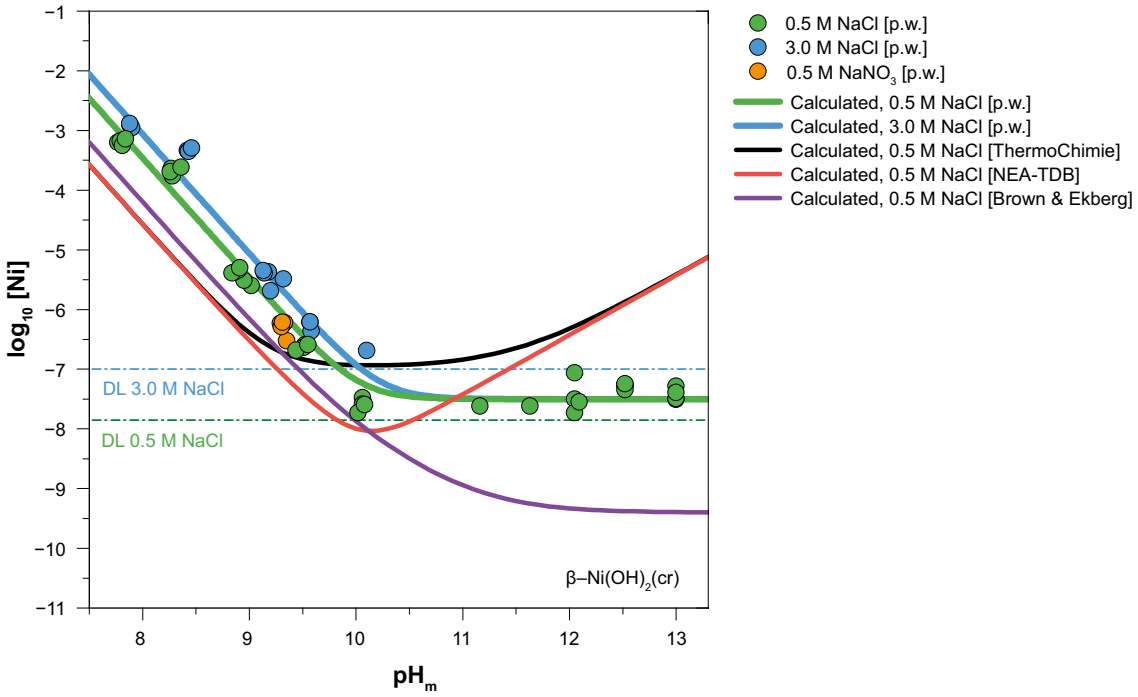

Figure 3-13. *Ni(II) experimental solubility data determined in the present work in 0.5 M NaCl–NaOH, 0.5 M $NaNO_3$ and 3.0 M NaCl–NaOH. Solid lines corresponding to the solubility of β-$Ni(OH)_2$(cr) calculated according with the thermodynamic model derived in the present work (green line: 0.5 M NaCl; blue line: 3.0 M NaCl), selected in NEA–TDB (Gamsjäger et al. 2005) (red line), ThermoChimie (Giffaut et al. 2014) (black line) and in Brown and Ekberg (2016) (purple line).*

Constant pH_m and $\log_{10}$ [Ni] readings confirm that 310 days is sufficient contact time to attain thermodynamic equilibrium in all the investigated NaCl–NaOH and $NaNO_3$ systems. Two main regions can be identified in the experimentally determined solubility data:

- $pH_m \leq 10$: A steep decrease of the solubility with a well-defined slope of –2 ($\log_{10}$ [Ni] vs. pH_m) is observed in this pH-region for both 0.5 M and 3.0 M NaCl systems, indicating that two H+ are taken up in the equilibrium reaction controlling the solubility of Ni(II). Solubility data in 0.5 M $NaNO_3$ agree very well with solubility data in 0.5 M NaCl, indicating that Ni(II)–Cl aqueous complexes play no significant role at this [Cl^-]. Thermodynamic calculations using NEA–TDB (Gamsjäger et al. 2005), ThermoChimie (Giffaut et al. 2014) or the selection in Brown and Ekberg (2016) clearly underestimate experimental solubility determined in the present work, very likely due to differences in crystallinity (e.g. particle size) of the solid phase.
- $pH_m \geq 10$: Solubility data in 0.5 M NaCl–NaOH show a pH-independent trend up to $pH_m \geq 13$, thus confirming that no H^+ are involved in the equilibrium reaction controlling the solubility of Ni(II) in this pH-range. These experimental observations are in disagreement with the increase in solubility calculated for this pH-region using thermodynamic data in NEA–TDB (Gamsjäger et al. 2005) and ThermoChimie (Giffaut et al. 2014), due to the selection of the anionic hydrolysis species $Ni(OH)_3^-$ in both databases. On the contrary, our experimental observations are in line with NiO(cr) and β-$Ni(OH)_2$(cr) solubility data reported by Palmer and co-workers (Palmer et al. 2004, 2011, Palmer and Gamsjäger 2010) (see Figure A3-3 in Appendix 3). A good agreement is also obtained with recent Ni(II) solubility data in 0.02 M NaOH solutions, approached from both under- and oversaturation conditions (Felipe-Sotelo et al. 2016). Note however that, although the trend in our solubility data is in agreement with thermodynamic calculations using the selection in Brown and Ekberg (2016), this model predicts a far too low solubility in this pH_m-region compared to our observations.

3.3.4 Experimental results in the presence of ISA

Solubility of Ni(II) in 0.5 M NaCl–NaOH–NaISA systems

The experimentally measured solubility of Ni(II) in the presence of [ISA] = 0.01, 0.1 and 0.2 M is shown in Figure 3-14. The figure includes thermodynamic calculations for the solubility of β-$Ni(OH)_2$(cr) in the absence and presence of ISA using thermodynamic data derived in the work González-Siso et al. (2018) as well as thermodynamic calculations in the presence of ISA based on the thermodynamic data selection in ThermoChimie (Giffaut et al. 2014). Note that ThermoChimie considers $\log_{10}$ $^*K°_{s,0}${β-$Ni(OH)_2$(cr)} = (11.03 ± 0.28) as currently selected in the NEA–TDB (Gamsjäger et al. 2005) .This value is significantly lower than $\log_{10}$ $^*K°_{s,0}${ β-$Ni(OH)_2$(cr)} determined by González-Siso et al. (2018), and thus the calculated solubility (in the absence of ISA) is lower than [Ni] experimentally measured by González-Siso et al. (2018).

3.3.5 Chemical, thermodynamic and activity models for the system Ni^{2+}–Na^+–H^+–Cl^-–OH^-–ISA^-–H_2O(l)

Table 3-*5* summarizes the chemical and thermodynamic models derived in the present work or reported in Gamsjäger et al. (2005) for Ni(II) in the absence and presence of ISA^-. These models properly explain experimental solubility data collected at $8 \le pH_m \le 13$. Table 3-6 provides all SIT ion interaction coefficients used in the present work and involving Ni(II), either as reported in Gamsjäger et al. (2005) or estimated in González-Siso et al. (2018).

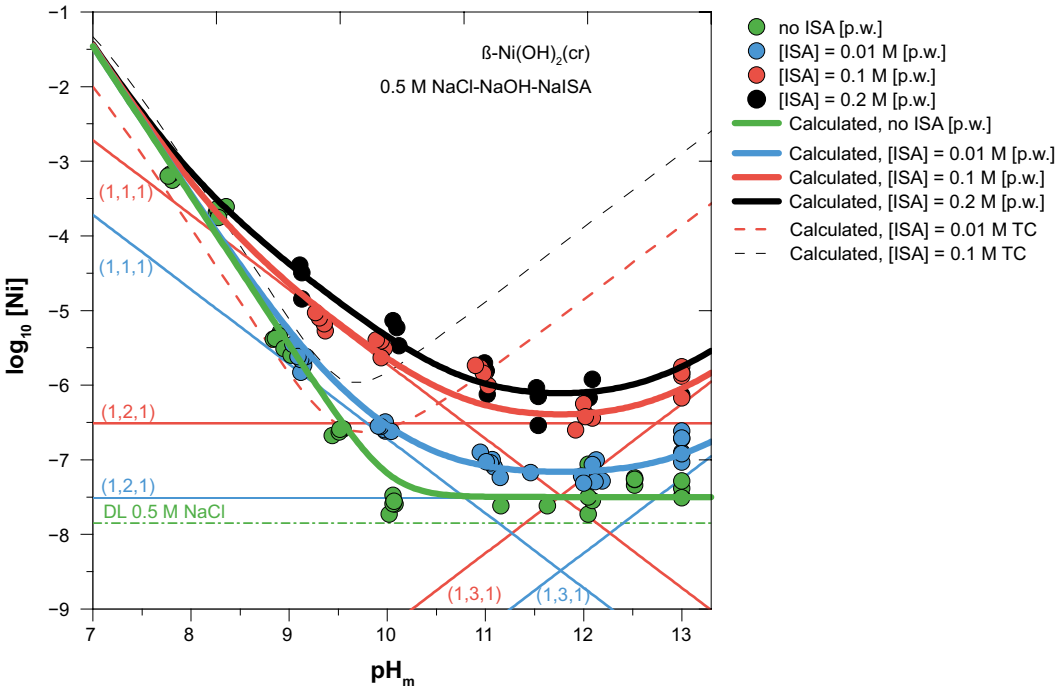

Figure 3-14. *Experimental solubility data of Ni(II) determined in the present work in 0.5 M NaCl–NaOH solutions, in the absence and presence of NaISA (0.01, 0.1 and 0.2 M). Solid lines corresponding to the solubility of α-$Ni(OH)_2$(cr) (thick lines) and underlying aqueous speciation (thin lines) in the absence and presence of NaISA as calculated with the thermodynamic model derived in the present work. Dashed lines corresponding to the solubility of α-$Ni(OH)_2$(cr) as calculated with the current thermodynamic selection in ThermoChimie (Giffaut et al. 2014).*

Table 3-5. Stability constants for the solubility, hydroxide and ISA complexes of Ni(II) as derived in González-Siso et al. (2018) or reported in Gamsjäger et al. (2005).

Solubility	$\log_{10}$ $^*K^\circ_{s,0}$	Reference
α-$Ni(OH)_2$(cr) + 2 H^+ ⇔ Ni^{2+} + 2 H_2O(l)	(12.09 ± 0.07)	(p.w.)
Hydroxide complexes	$\log_{10}$ $^*K^\circ_{(1,n)}$	
Ni^{2+} + 2 H_2O(l) ⇔ $Ni(OH)_2$(aq) + 2 H^+	–(19.7 ± 0.4)	(p.w.)
Chloride complexes	$\log_{10}$ $K^\circ_{(1,n)}$	
Ni^{2+} + Cl^- ⇔ $NiCl^+$	(0.08 ± 0.60)	Gamsjäger et al. (2005)
ISA complexes	$\log_{10}$ $^*K^\circ_{(1,n,1)}$	
Ni^{2+} + H_2O(l) + ISA^- ⇔ NiOHISA(aq) + H^+	–(6.5 ± 0.3)	(p.w.)
Ni^{2+} + 2 H_2O(l) + ISA^- ⇔ $Ni(OH)_2ISA^-$ + 2 H^+	–(17.6 ± 0.5)	(p.w.)
Ni^{2+} + 3 H_2O(l) + ISA^- ⇔ $Ni(OH)_3ISA^{2-}$ + 3 H^+	–(31.0 ± 0.7)	(p.w.)

Table 3-6. SIT ion interaction coefficients used in the present work for Ni(II) hydroxide and ISA complexes.

i	j	ε (*i*, *j*)	Reference
Ni^{2+}	Cl^-	(0.17 ± 0.02)	Gamsjäger et al. (2005)
$NiCl^+$	Cl^-	(0.21 ± 0.06)	Estimated by correlation with ε(*i*, ClO_4^-)
$Ni(OH)_2$(aq)	Na^+ / Cl^-	0	By definition in SIT
NiOHISA(aq)	Na^+ / Cl^-	0	By definition in SIT
$Ni(OH)_2ISA^-$	Na^+	–(0.05 ± 0.10)	Estimated by charge analogy (Hummel 2009)
$Ni(OH)_3ISA^{2-}$	Na^+	–(0.10 ± 0.10)	Estimated by charge analogy (Hummel 2009)

3.3.6 Conclusions

The solubility of Ni(II) in dilute to concentrated aqueous NaCl–NaOH systems ($I \leq 3.0$ M) in the absence of ISA is controlled by β-$Ni(OH)_2$(cr), and can be explained by the predominance of Ni^{2+} and $Ni(OH)_2$(aq) in the aqueous phase. Differences in the value of $\log_{10}$ $^*K^\circ$s,0{ β -$Ni(OH)_2$(cr)} determined in the present work and the data available in the literature highlight the important role of particle size / crystallinity effects in the solubility-control of this system. The use of $\log_{10}$ $^*K^\circ$s,0{β-$Ni(OH)_2$(cr)} currently selected in the NEA–TDB (Gamsjäger et al. 2005) for a very crystalline solid phase tend to underestimate the solubility of Ni(II) in natural and anthropogenic systems. We found no evidence for the formation of the anionic species $Ni(OH)_3^-$ up to $pH_m \leq 13$. The solubility of β-$Ni(OH)_2$(cr) remains pH-independent with a total nickel concentration below $\approx 10^{-7}$ M within the pH_m range 10 to 13.

The solubility of Ni(II) at $7.5 \leq pH_m \leq 13$ is increased up to 2 orders of magnitude in the presence of ISA relative to comparable ISA-free systems. These results confirm the capacity of ISA to outcompete hydrolysis even under strongly alkaline pH conditions. Solubility data determined in the present work can be properly explained with a simple chemical model including the predominance of the complexes NiOHISA(aq), $Ni(OH)_2ISA$– and $Ni(OH)_3ISA^{2-}$ in the aqueous phase. These results furthermore provide indirect evidence on the deprotonation of the a-OH group of ISA at $pH_m > 8$ induced by the complexation with Ni(II).

This work represents the most comprehensive experimental study available to date reporting chemical, thermodynamic and activity models for the system Ni^{2+}–Na^+–H^+–Cl^-–OH^-–ISA^-–H_2O(l) at low to intermediate ionic strength, valid from near-neutral to hyperalkaline pH conditions. The equilibrium models developed represent a significant improvement and are highly relevant for calculating reliable Ni(II) source term concentrations in the context of safety assessments for L/ILW repositories.

3.4 Uptake of Ni(II) by cement in the presence of ISA

3.4.1 Introduction

Cement is the largest mass component of the SFR repository, knowledge of the interaction between cement and the potentially released radionuclides is fundamental to assess their mobility.

Ordinary cement has a relevant amount of Ni in its composition. There are several publications in the literature dealing with the behaviour of Ni in the presence of cement which point towards Ni being solubility and not sorption limited in cementitious environment (Hietanen et al. 1984, Wieland et al. 2006, Ochs et al. 1998). Scheidegger et al. (2000) proved that Ni Al-containing hydrotalcite-like layered double hydroxides (LDH) formed when Ni was added to cement materials under very high alkaline conditions (stage I of degradation of cement, pH around 13.3). According to these authors, the LDH solids were formed under conditions oversaturated with respect to the Nickel hydroxide after 150 days of aging, and XAFS and DRS results unequivocally identified LDH in the system.

Wieland and Van Loon (2003) in their Cementitious Near-Field Sorption Data base revision of 2003, propose the elimination of distribution coefficients for Ni onto cement, and taking into consideration that it is solubility limited. The same authors recognise that the composition of the solid phase accounting for the Ni solubility limitation is not clear, although a solid solution with LDH-type structure can be proposed.

The determination of the uptake of radioactive nickel onto cement is therefore hampered by the presence of nickel in the cement composition used in the experiments. Nickel concentrations of water equilibrated with cement in our experiments are in the range $1–3 \times 10^{-7}$ M at pH 12.5. These values agree with other data in the literature (Wieland et al. 2006). To overcome this difficulty, uptake experiments were done by using ^{63}Ni as a tracer, a procedure also used by other experimentalists when investigating the behaviour of Ni in cementitious environments (Wieland et al. 2006).

Wieland et al. (2006) presented results of partitioning tests of Ni in artificial cement water, which showed that the concentration of Nickel in solution was independent of the solid-to-liquid ratio used in the experiments in a range of S/L between 10^{-6} and 0.13 Kg/L. Their sorption study showed that the concentration of Ni in solution increased only slightly when the added Ni concentration changed over several orders of magnitude. In all cases, reported Nickel concentration in waters equilibrated with cement materials were in the order of 2×10^{-7} M, below the solubility of the pure nickel hydroxide calculated with the thermodynamic data available by then, and impossible to be described by a reversible sorption process. Wieland's data supported the hypothesis that the uptake of radioactive Ni on cement proceeds via isotopic exchange with stable nickel (see Ochs et al. 2014 and references therein).

Our data of total aqueous nickel in the system, measured at pH 12.5 indicate concentrations in the range of $1–3 \times 10^{-7}$ M (see Appendix 4), which agree with the solubility of $Ni(OH)_2(cr)$ experimentally determined in preceding sections. On these basis, we cannot exclude that in our system it is $Ni(OH)_2(cr)$ and not a mixed Ni-Al DLH the one controlling the solubility of Nickel, although we do not have sufficient solid characterisation to support this hypothesys.

We have proved that the presence of ISA enhances the solubility of Ni(II) under alkaline conditions and consequently, there is a need to assess the effect of ISA onto the uptake of Ni on cement. ISA interacts with the cement surface and a ternary surface complex with Ca has been proposed to account for ISA uptake (Pointeau et al. 2008, Van Loon et al. 1997). Consequently, it is important to handle the surface interactions between Ni(II), Ni-ISA complexes and ISA in a comprehensive way to understand and quantify the processes of retention of Ni in the Ni-ISA-cement system.

3.4.2 Experimental

The cement used in the experiments was grinded and sieved SKB ordinary Portland cement powder ($d_{av} < 100$ μm), CEMI42.5NBV/SR/LA type. An extensive physical characterization has been performed including, XRD, DTA, SEM-EDX and BET surface area determination.

The XRD diffractogram confirmed the predominance of portlandite, as expected. The complete cement analyses available is shown in Appendix 3.

Typical sorption experiments were set up in teflon tubes, where a weighed amount of crushed and sieved cement was contacted with the desired solution.

All solutions were prepared with purified water (Milli-Q acadèmic, Millipore) and purged for 2h with Ar before use, to remove traces of O_2 and CO_2. All the samples were prepared, stored and handled inside an inert gas (Ar) glovebox (O_2< 5ppm) at $T=(22\pm2)$°C.

A first set of experiments investigated the sorption of ISA on cement, as follows (Exp ISA):

Exp ISA:

1. Cement was left to equilibrate with deionized water (up to 30 days).
2. 3 different ISA concentrations were added to 3 experiments and the concentration of ISA in solution was measured at different time intervals.

In order to ascertain whether the addition of the components had some influence on the ^{63}Ni uptake by cement the following three procedures were used in the experiments:

Exp A:

1. Cement was left to equilibrate with deionized water (up to 30 days).
2. ^{63}Ni tracer was spiked to the experiment and left to equilibrate for 2 days.
3. ISA was added to the experiment.

Exp B:

1. Cement was left to equilibrate with deionized water (up to 30 days).
2. ISA was added to the experiment and left to equilibrate for 2 days.
3. ^{63}Ni tracer was spiked to the experiment.

Exp C:

1. ^{63}Ni and ISA solutions were left to equilibrate for 2 days.
2. The ^{63}Ni and ISA equilibrated solution was put in contact with equilibrated cement with deionized water (up to 30 days).

In all cases, the solid to liquid ratio in the experiments was of 25g/L. The pH was always constant at 12.5, as expected, buffered by equilibrium with portlandite. ^{63}Ni was added in all experiments to reach an initial concentration of 2.83×10^{-10} mol dm^{-3}.

The kinetics of the sorption process was studied by following the evolution of the concentration of ^{63}Ni with time.

At desired time intervals, 5 mL of the supernatant solution was taken and centrifuged for 20 minutes to separate colloids or suspended solid phase. 1mL of the solution was filtered in Polyether 10 kD filters, mixed with 10 mL LSC cocktail (Ultima Gold™ XR , Perkin-Elmer) in a screw-cap vessel (PP, 20 mL, Zinsser Analytic) and measured with a LKB Wallac 1220 Quantulus Liquid Scintillation Counter for 30 minutes each for ^{63}Ni determination.

ISA concentration in “Exp ISA” was determined by NPOC (non-purgeable organic carbon) technique.

Distribution solid to liquid ratios of ^{63}Ni($^*R_d$) were calculated by dividing the measured ^{63}Ni in solution over the ^{63}Ni retained in the solid phase, as expressed in equation (3-15):

$$^*R_d = \frac{\left[^{63}Ni\right]aq}{\left[^{63}Ni\right]0-\left[^{63}Ni\right]aq} \qquad (3\text{-}15)$$

Where

$[^{63}Ni]aq$ stands for the LSC measurement in solution and $[^{63}Ni]0$ is the initial concentration of ^{63}Ni added to the sorption experiment.

The same procedure was used to determine the R_d(ISA):

$$R_d(ISA) = \frac{[ISA]aq}{[ISA]0-[ISA]aq} \quad (3\text{-}16)$$

The conditions of the uptake experiments and the results obtained are shown in Appendix 4. For the sake of completeness, also the concentration of total Ni (stable) in the experiments, determined by ICP-MS, is provided.

3.4.3 Results and Discussion

ISA uptake

The experiments of sorption of ISA showed no important kinetic effects (in agreement with resuls obtained by Van Loon et al. 1997 and Pointeau et al. 2008), except for the higher concentration of ISA (0.1 M) where the concentration decreased probably due to the formation of the Calcium isosaccharinate solid phase.

The results indicate ISA sorption percentages in the range 34 % to 73 %. The calculated R_d values (between 20 and 107 L/Kg) are in line with those obtained by Pointeau et al. (2008).

Van Loon et al. (1997) investigated the sorption of α-ISA onto Portland cement at pH 13.3, i.e. stage-I of cement degradation. Initial ISA concentrations added to the system were in the range 10^{-6} to 0.1 M. The authors obtained the best fit to their data by adjusting a 2-site Langmuir-type isotherm.

Pointeau et al. (2008) investigated the uptake of different anionic compounds by cement. These authors worked in the pH range 11.5–13.5 and observed a dependence of the calculated R_d(ISA) with pH. Sorption increased from pH 11.5 to pH 12.5 and decreased until pH 13.5. The authors discuss that the ISA uptake is a surface mechanism, given the faster kinetics in comparison with the uptake of other anions tested (for details see Pointeau et al. 2008). Taking into account that the dominant species of ISA is negatively charged at this pH, and so is the surface of the solid phase, the authors proposed that Ca sorbed to the cement surface and conditioned a positive surface charge that facilitated the formation of a mixed surface complex >SOCaH$_4$ISA, according to the equilibrium:

$$> SOH + Ca^{2+} + H_4ISA^- \leftrightarrow > SOCaH_4ISA + H^+ \quad (3\text{-}17)$$

with a logK = −7.5.

We have approached the modelling of our data in three different ways:

- Model I: Langmuir-type isotherm, as in Van Loon et al. (1997).
- Model II: Surface complexation, conditioned by Ca, as in Pointeau et al. (2008).
- Model III: Surface complexation without expliciting Ca sorption to the surface.

PHREEQC has been used as calculation tool in the case of Models II and III. The adjustment of the Langmuir isotherm, together with the information on specific surface area determined by BET measurements have allowed the calculation of the density of surface sites. The PHREEQC inputs are shown in Appendix 5.

The results (shown in Figure 3-15) were not improved by incorporating a second type site in the Langmuir isotherm, as proposed by Van Loon et al. (1997). The model was not able to describe the results at the higher ISA contents, probably due to the precipitation of the solid Calcium isosaccarinate. It is also noticeable that both surface complexation models tested -Models II (Pointeau) and III (the tailored SCM without Ca conditioning the surface)- provided reasonably good data descriptions. The increase of R_d simulated for higher concentrations of ISA agrees with the data and is due to the precipitation of Calcium isosaccarinate, allowed to happen in the phreeqC simulation once the solid reaches saturation.

Models II and III considered that the system was equilibrated with portlandite, what provided a continuous Calcium source both, for the precipitation of $Ca(Isa)_2(cr)$, as well as for the conditioning of the surface by Ca needed in Model II. Given that the concentration of Ca measured in the water in equilibrium with cement was below the saturation of portlandite (0.006 M), we tested which would be the effect of not having a sufficient calcium source. The results are shown in Figure 3-16 in terms of R_d versus initial ISA concentration added to the system.

It seems clear that data at the higher ISA concentrations, likely affected by the precipitation of $Ca(Isa)_2(cr)$, needs of a sufficiently high source of Calcium such as the one provided by portlandite or by the dissolution of Calcium contained in the CSH phases of cement. When this continuous source is not present, the models do not reproduce the data at higher ISA concentration. Although both models; II and III, provide a reasonable good description of the data, Model III performs better, especially in the lower range of ISA concentrations, as it does not depend on the conditioning of the surface by calcium, in opposition to Model II.

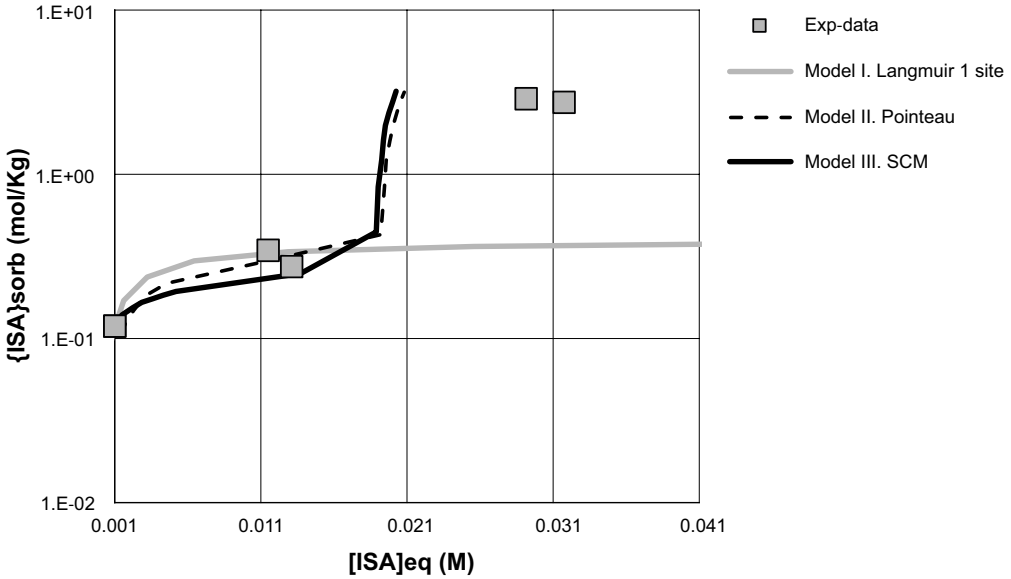

Figure 3-15. *Comparison between experimental data of ISA uptake by cement and the different models tested. For explanations see text.*

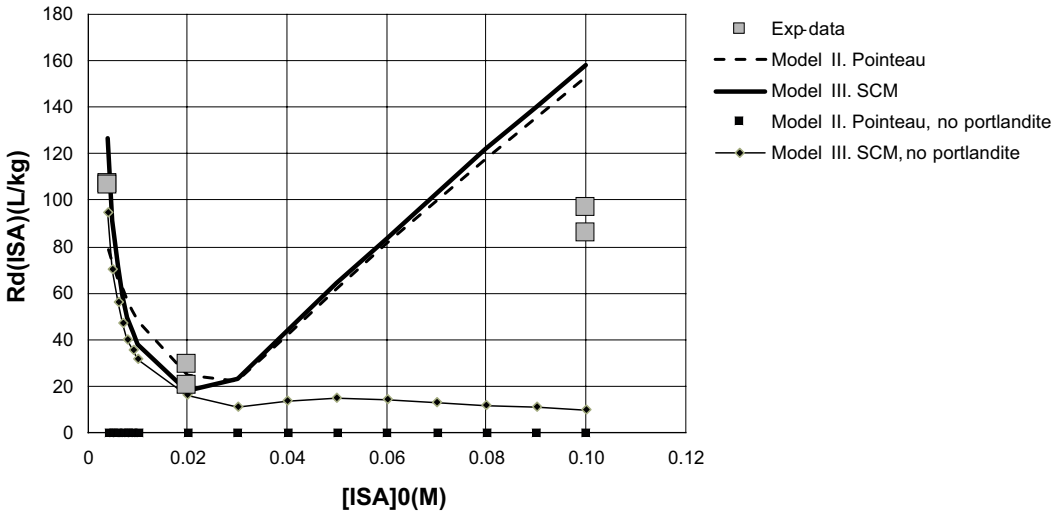

Figure 3-16. *Comparison between experimental data and Models II and III with and without considering the infinite source of Calcium provided by portlandite.*

Nickel uptake

The results of the ^{63}Ni uptake experiments show no important kinetic effects and the same observation holds for the evolution of the total concentration of Ni in the experiments.

For the sake of data interpretation, we have calculated average distribution coefficient values for ^{63}Ni ($^{*}R_d$) for each experimental condition.

The results are shown in Figure 3-17 and in tables in Appendix 4.

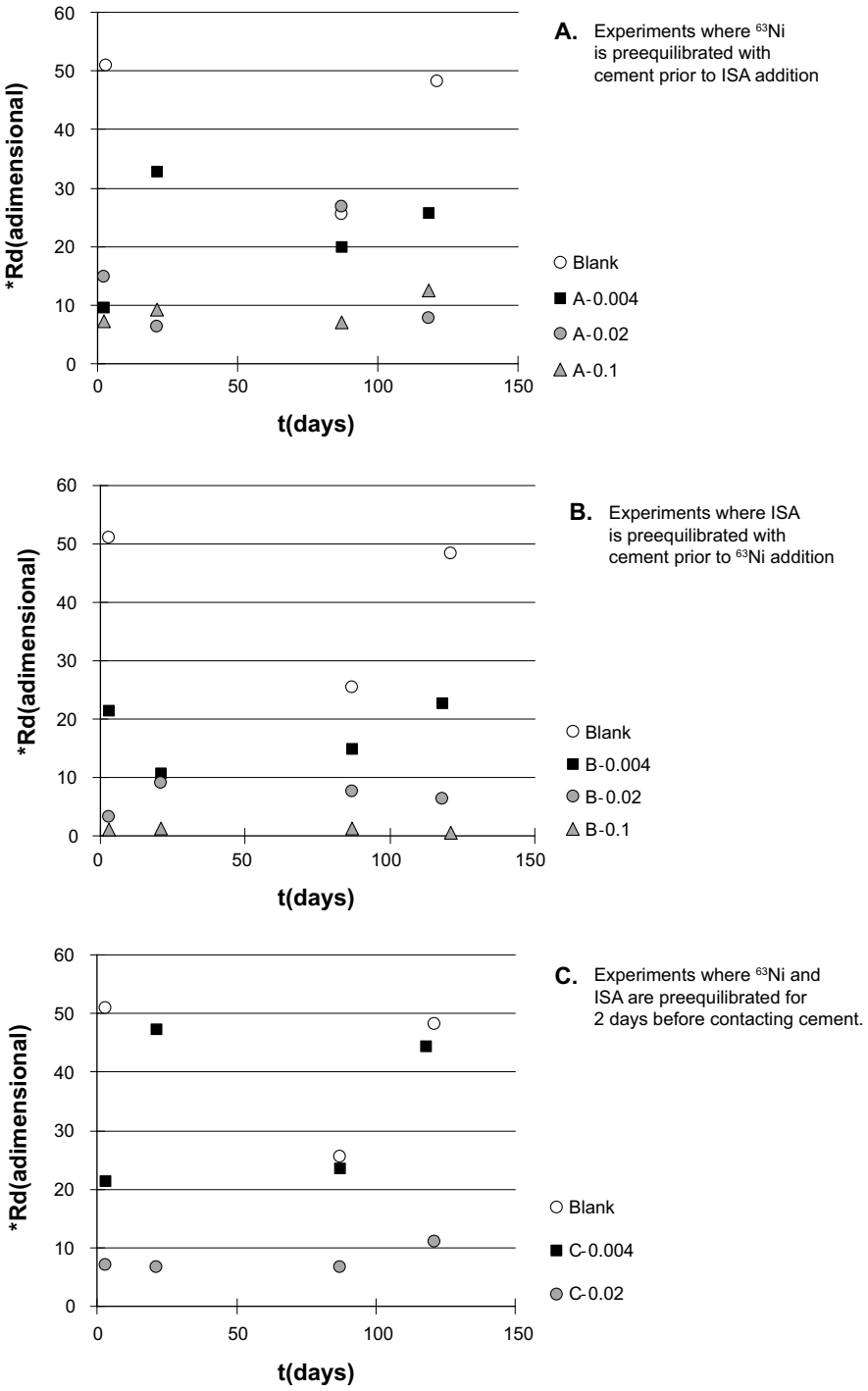

Figure 3-17. Evolution of $^{*}R_d$ with time in experiments A, B and C.

There is a clear dependence of the sorption extent of ^{63}Ni with the total ISA concentration, which was expected as per the complexation scheme Ni-OH-ISA elucidated in the previous chapters of this report.

The values of $^{*}R_d$ obtained under the different conditions (Figure 3-18) show that, for the same ISA concentration, the uptake extent is higher when Ni contacts the solid before adding lSA (experiments A) than in the reverse order (Experiments B). This may be related with the difficulty of ISA to detach Ni from the solid once it is already incorporated (or attached to its surface) and also to the blocking of sites by ISA if it is previously sorbed to the cement surface, as shown in the precedent sub-section.

Sorption Reduction Factors for active ^{63}Ni(*SRF) have been calculated as the ratio between the distribution ratio in the absence ($^{*}R_d^0$) and that in the presence of the complexing agent ($^{*}R_d^L$). The value of *SRF gives an indication of the reduction in sorption extent occurring due to the presence of the ligand (3-18).

$$* SRF = \frac{^{*}Rd^{0}}{^{*}Rd^{L}} \qquad (3\text{-}18)$$

*SRF values vary from 1.2 to almost 40 (Table 3-7). Previous data in the literature indicated no influence of ISA on the sorption of Ni onto cement until ISA concentrations around 0.01 M (Wieland et al. 2000, Van Loon and Glaus 1998). In our case a decrease of ^{63}Ni uptake is visible for the lowest concentration of ISA used in the experiments (0.004 M), with *SRF values between 1.2 and 2.4, depending on the order of addition of the reactants.

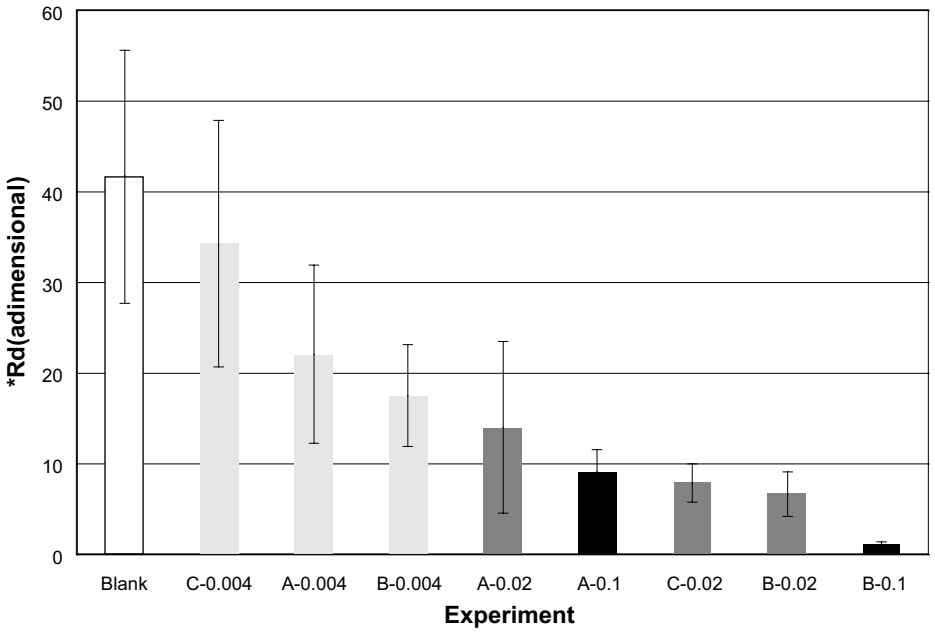

Figure 3-18. *Plot of $^{*}R_d$ in decreasing order. Labels in the x-axis indicate the conditions of the experiments, as presented in* Table 3-7.

Table 3-7. Average $^{*}R_d$ values obtained in the experiments for ^{63}Ni and calculated Sorption Reduction Factors.

sample	[ISA]0	$^{*}R_d$	*SRF
Blank	0	41.60 ± 14.01	1.00
A-0.004	0.004	22.02 ± 9.78	1.89 ± 1.48
A-0.02	0.02	13.93 ± 9.43	2.99 ± 3.03
A-0.1	0.1	9.02 ± 2.51	4.61 ± 2.84
B-0.004	0.004	17.46 ± 5.68	2.38 ± 1.58
B-0.02	0.02	6.62 ± 2.51	6.28 ± 4.50
B-0.1	0.1	1.06 ± 0.31	39.35 ± 24.71
C-0.004	0.004	34.19 ± 13.61	1.22 ± 0.89
C-0.02	0.02	7.86 ± 2.11	5.30 ± 3.20

We have derived the values of SRF by using the thermodynamic speciation scheme presented in Section 3.3.5 of this report. The details of the calculations are shown in the following section.

Derivation of SRF theoretical values

Without information on the stoichiometry of the surface complex formed between Ni and the surface of the solid, we can write a generic sorption reaction under the conditions of the experiment as:

$$> SOH + "63Ni(aq)" \leftrightarrow " > SOH - 63Ni" \quad (3\text{-}19)$$

Where "63Ni(aq)" stands for the total concentration of active Ni in solution, independently on the species formed, and "$>$SOH-63Ni" represents the Ni that has been sorbed or incorporated to the solid phase. From the former reaction we can define $^{*}R_d$ as:

$$^{*}R_d = \frac{[">SOH-63Ni"]}{["63Ni(aq)"]} \quad (3\text{-}20)$$

The set of reactions and equilibrium constants considered for the calculation of SRF is shown in Table 3-8.

Table 3-8. Set of reactions considered in the thermodynamic derivation of SRF. The acid/base character of ISA is not considered as under the conditions of the experiment the dominant species is the one used for the calculations.

Reaction	logK and reference
$Ni(OH)_2$ +ISA^- + H^+ = Ni(OH)ISA	logK1' = 13.2 (p.w.)
$Ni(OH)_2$ + ISA^- = $Ni(OH)_2ISA$	logK2' = 2.6 (p.w.)
$Ni(OH)_2$ + ISA^- + H_2O = $Ni(OH)_3ISA$ + H^+	logK3' = −11.3 (p.w.)
$Ca(OH)_2(s)$ + $2H^+$ = Ca^{2+} + $2H_2O$	logKs = 22.8 (ThermoChimie)
Ca^{2+} + ISA^- = $CaISA^+$	logKISA = 1.7 (ThermoChimie)
Ca^{2+} + ISA^- + H_2O = Ca(OH)ISA + H^+	logKISA' = −10.4 (ThermoChimie)

In the absence of ISA at pH 12.5, the dominant Ni species in solution is $Ni(OH)_2(aq)$, and the contribution of ISA species to the total concentration of Ni in solution increases with the ISA concentration in the system (see Figure 3-19).

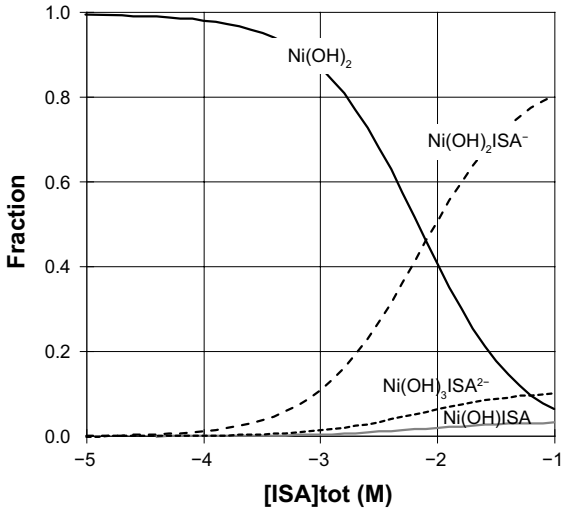

Figure 3-19. *Fractional diagram of aqueous Ni species at pH 12.5 as the concentration of ISA increases in the system.*

We can substitute [Ni(aq)] in (22) by [$Ni(OH)_2$] in the absence of ISA, while it will be equal to the total sum of aqueous Ni species in the case of having ISA in the system. Thus, we can write:

$$* Rd^0 = \frac{[>SOH-Ni(OH)_2]}{[Ni(OH)_2]} \quad (3\text{-}21)$$

and

$$* Rd^L = \frac{[>SOH-Ni(OH)_2]}{[Ni(OH)_2]\left\{1+K_1'[ISA^-][H^+]+K_2'[ISA^-]+K_3'\frac{[ISA^-]}{[H^+]}\right\}} \quad (3\text{-}22)$$

From where, substituting in (18) (for the meaning of the constants see Table 3-8) we obtain:

$$* SRF = \frac{*Rd^0}{*Rd^L} = \left\{1 + K_1'[ISA^-][H^+] + K_2'[ISA^-] + K_3'\frac{[ISA^-]}{[H^+]}\right\} \quad (3\text{-}23)$$

The calculation of the free concentration of [ISA^-] needed for the calculation of the SRF depends on different parameters and processes, as discussed below:

- ISA forms complexes with Calcium that can be important in the presence of cement, especially as the calcium concentration is expected to be controlled by equilibrium with portlandite ($Ca(OH)_2(s)$). The concentration of Calcium in the system affects therefore, the impact of ISA on the sorption extent of Ni. Equilibrium with portlandite fixes the free Ca^{2+} concentration at a value of 0.006 M. The few measured data of Ca in solution available from our experiments indicate total Calcium concentrations of 0.006 M, ie. lower concentration of Ca^{2+} than the one given by equilibrium with portlandite.
- ISA can precipitate with calcium forming calcium isosaccharinate.
- ISA itself can sorb onto the cement surface, as recognized in the literature for example by Pointeau et al. (2008) and as observed and modelled in our experiments. ISA Sorption percentages in our data range between 30 % and 60 %.

The former processes and variables have been considered also for the calculation of the theoretical SRF in this work, so that [ISA^-] is expressed as a combination of all the relevant parameters in the system, and the senstitivity of the calculated SRF to some of these variables has been assessed.

The comparison between the experimental and the calculated $*R_d$ and *SRF values versus the total concentration of ISA in the system is shown in Figure 3-20.

As appreciated the speciation scheme proposed for the complexation Ni-ISA is able to explain the data.

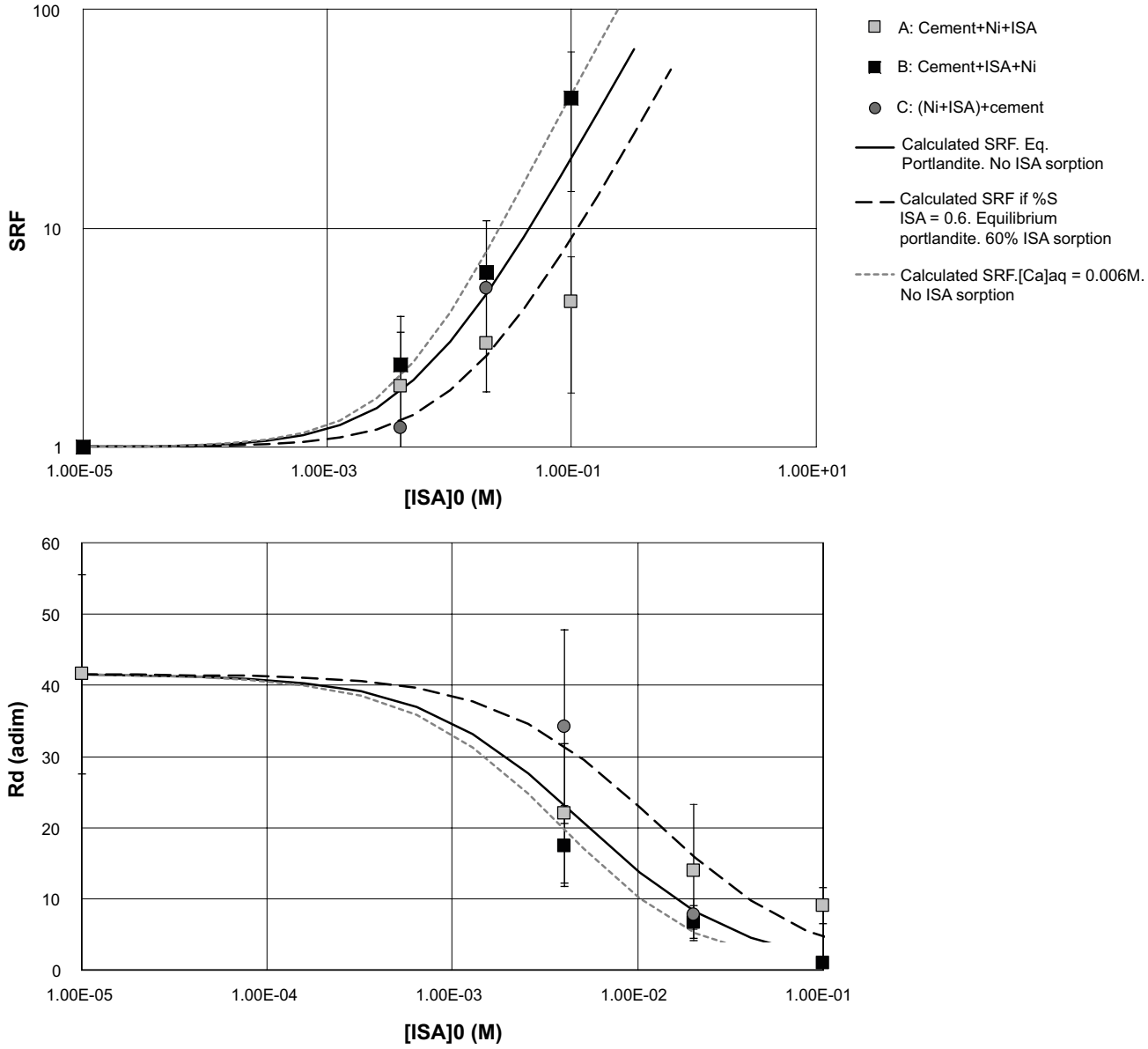

Figure 3-20. *Comparison between SRF calculated and SRF experimentally determined (upper) and *Rd calculated and *Rd experimentally determined (lower). Different calculation hypothesis are presented.*

The central case (continuous line) considers that ISA does not sorb on the cement surface and that the concentration of calcium is controlled by portlandite equilibrium.

Incorporating ISA sorption (dashed line), leaves less ISA for Ni complexation, thus higher $^*R_d$ and lower *SRF.

Decreasing calcium concentration to the measured values in the experiment (dotted line) decreases soption, as more ISA is available for Ni complexation, thus increases SRF.

The performance of the model in reproducing independent data in the literature has been tested with the work of Warwick et al. (2003). These authors reported distribution of Nickel between an ion exchange resin and the solution at different ISA concentrations at pH 10 and 13. The comparison between the model calculations and the experimental data at pH 10 and 13 is shown in Figure 3-21. A case simulating a 60 % of ISA sorption on the exchange resin has been also calculated.

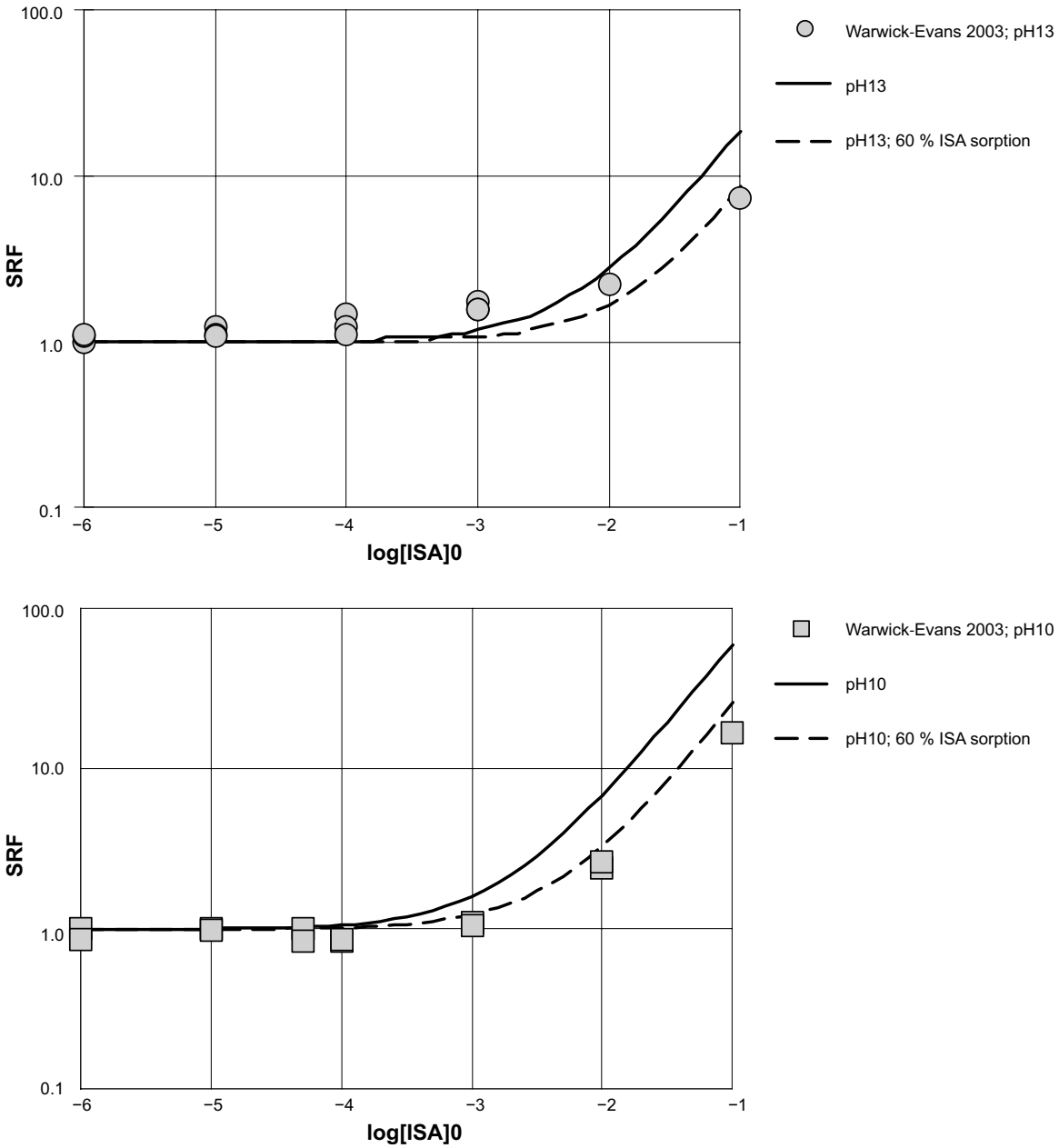

Figure 3-21. *Comparison between calculated and experimental Sorption Reduction Factors derived by Warwick et al. (2003) at pH 13 and pH 10. Dashed lines stand for the results of the model under the assumption of 60 % of ISA sorption on the solid phase.*

Our model is able to reproduce independent SRF data with a reasonable degree of accuracy. Assuming ISA retention on the solid surface improves the representation of the experimental data.

Once observed that the model hypothesis was able to reproduce the measured data, we have attempted a surface complexation model by considering both the uptake of ISA and that of ^{63}Ni on the surface of the solid, and allowing for $Ca(Isa)_2(cr)$ to form if supersaturated. The complete model (Model-A21) combines the model developed for the sorption of ISA presented in the previous section (Model III) with the formation of a "generic surface complex" between ^{63}Ni at the solid surface, as expressed by the following reacton:

$$>SOH + {}^{63}Ni(OH)_2 = Z\_sOH^{63}Ni(OH)_2;\ \text{with } \log K = 3.6 \qquad (3\text{-}24)$$

Where >SOH stands for the solid surface. The value of logK has been adjusted to fit the data.

The comparison between model and data are shown in Figure 3-22 for the simulation of the uptake of ISA and that of ^{63}Ni.

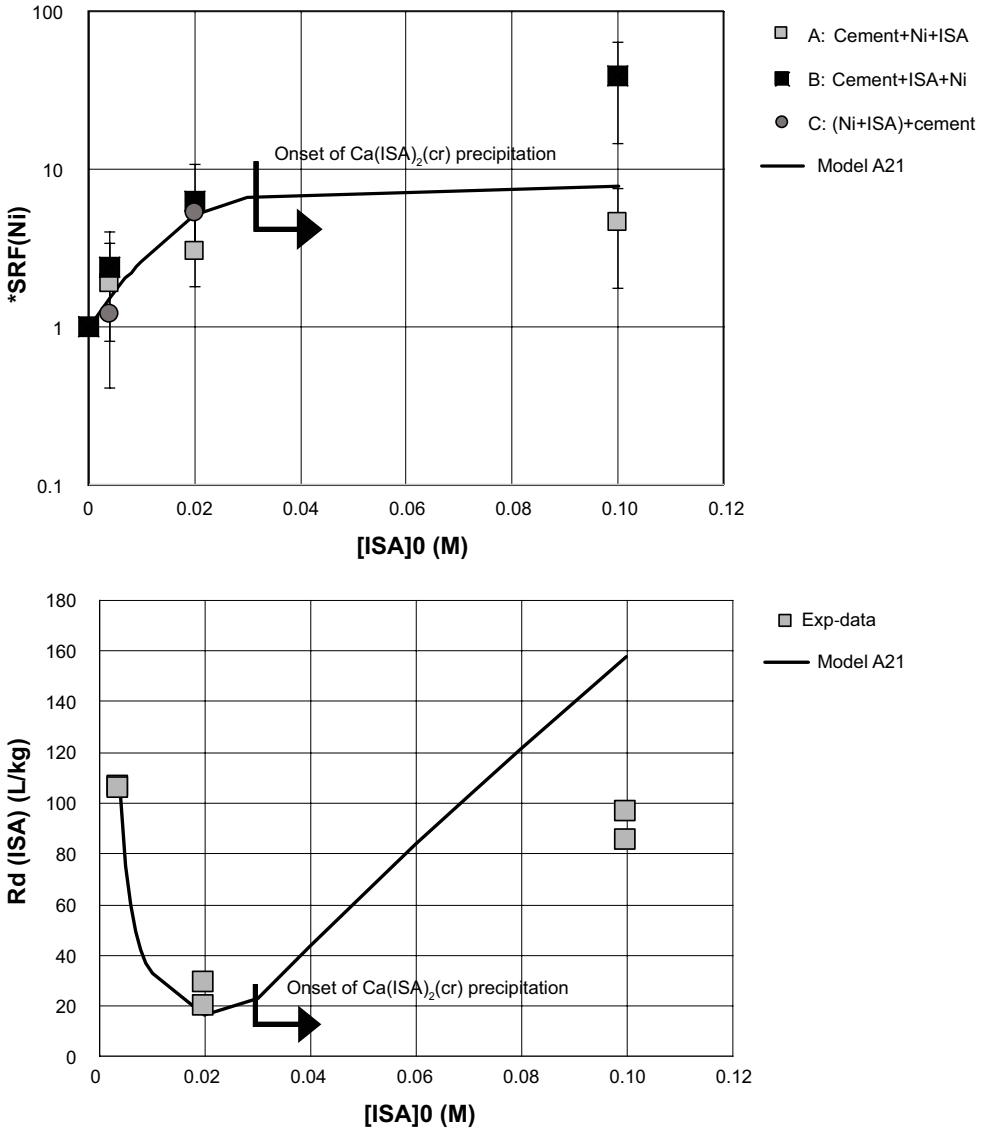

Figure 3-22. *Comparison between the complete model including surface complexation of ISA and Ni and experimental data. The arrow indicates the start of oversaturation of the $Ca(ISA)_2(cr)$ solid phase.*

As previously discussed, solubility and not sorption is proposed in the literature for Ni retention in cement under repository conditions. The uptake of ^{63}Ni is considered as isotopic exchange with the pre-existing stable Ni in cement. Our data and assumptions, however, seem to agree with a surface model for the uptake of ^{63}Ni.

According to Wieland et al. (2006) and later compilations by Wang et al. (2009) and Ochs et al. (2016), the isotopic exchange of active to non active Ni (α) in cementitious environments equals the ratio between the distribution ratio of the active $^*R_d$ to the one of the stable (R_d) isotope:

$$\alpha = \frac{^*R_d}{R_d} \quad (3\text{-}25)$$

The R_d for stable nickel needs of the determination of the total Ni content in the solid and can be calculated by the following expression:

$$Rd = \frac{C_s^0}{S} \quad (3\text{-}26)$$

Where C_s^0stands for the initial concentration of Ni in the solid (we do not have this value for our cement composition) and S is the solubility of Ni in the cement equilibrated water (in our case, 1.4×10^{-7} M).

Therefore, the value of the distribution ratio for the active isotope, $^*R_d$, can be calculated by the following equation:

$$^*R_d = \alpha \frac{C_s^0}{S} \quad (3\text{-}27)$$

By using data in Wieland et al. (2006) for α and in Wieland and Van Loon (2003) for S, and by using average Nickel contents in CEM I, CEM IIIa and CEM IIIB cements, Ochs et al. (2016) calculated $^*R_d$ varying between 26 and 730 L/Kg depending on the type of cement, in its degradation stage I (pH = 13.3). The same authors propose values for stage II of degradation of cement (pH 12.5, equivalent to our experiments) which vary between 160 and 4 500 L/Kg (see for example Wang et al. 2009, Table 4-27 and Ochs et al. 2016, Table 5-6). This $^*R_d$ increase from stage I to stage II of cement degradation relies on the formation of $Ni(OH)_3^-$, which is not supported by our experimental data.

In the absence of ISA, we obtain a value of $^*R_d$ = 1664±560 L/Kg, reduced to lower values due to the presence of ISA, to compare with the range of values calculated for stage II in Ochs et al. (2016) and in Wang et al. (2009), between 160 and 4 500 L/Kg.

Wang et al. (2009) discussed about the validity of the determination of the $^*R_d$ of ^{63}Ni and argued that, although Ni is probably solubility limited, the removal of ^{63}Ni will still occur through isotopic exchange and the $^*R_d$ would reflect a "genuine adsorption process". He concludes that although most of published experiments did not take into account the stable Ni in solution, the $^*R_d$ measured with radiotracer should still be valid for evaluating uptake of Ni.

It is worth noting that the calculated $^*R_d$ and resulting SRF's in this work, determined for active ^{63}Ni in the presence of relatively large amounts of stable Ni mimic the expected evolution of the repository condition: release of active ^{59}Ni in the presence of non-active nickel in the SFR repository. It is evident from our work that the measured influence of ISA on the $^*R_d$ is also valid to account for the uptake of active Ni in Safety Assesment considerations, as well as for assessing the influence of ISA on the uptake process.

The influence of organics on Ni uptake by cement is reviewed and discussed by Ochs et al. (2014, 2016 and references therein). Wieland et al. (2000) observed no influence of ISA on Ni(II) uptake up to a concentration of about 1 mM, Holgersson et al. (1998) observed a corresponding value of 5 mM ISA. The same authors refer to the work of Van Loon and Glaus (1998) who compared Ni(II) sorption on feldspar as a function of ISA concentration and observed only a minor sorption reduction at dissolved ISA concentrations > 0.01 M. On the basis of their review, Ochs et al. (2014) propose allocating a SRF of 1 for Ni (no effects of organic ligads) and define a conservative SRF of 10 for organic ligand concentrations above 5mM.

Most of the SRF values for ^{63}Ni produced by our work are below 10, even for 0.1 M ISA concentrations (see Appendix 4 and Figure 4-20). Only in one case, working at concentrations of 0.1 M ISA a value of SRF of 40 was obtained.

According to Keith-Roach et al. (2014) the maximum concentration of ISA in the relevant waste packages in the SFR will be of 0.02 M, given by the precipitation of $Ca(Isa)_2(cr)$ under portlandite equilibrium. Under the conditions of our experiments, a concentration of ISA of 0.02 M would imply a *SRF(Ni) between 5 and 7.

3.4.4 Conclusions

Our results indicate that ISA complexation with nickel reduces ^{63}Ni uptake to cement for concentrations of ISA equal or above 0.004 M.

Under the concentrations of ISA expected in repository conditions, the majority of our data indicate *SRF for ^{63}Ni in the order of 2 to 10, in agreement with previous data in the literature.

The speciation scheme of the system Ni-OH-ISA derived in this work can be satisfactorily used to explain the reduction of ^{63}Ni uptake by cement, as well as independent experimental data of Ni sorption onto a solid of different characteristics to cement.

The uptake process of ^{63}Ni and ISA as well as the effect of ISA on ^{63}Ni sorption has been explained by a simple sorption model which incorporates the speciation scheme derived in the solubility assessment.

Although aqueous Ni in cement under repository conditions seems to be solubility, and not sorption limited, the behaviour of ^{63}Ni added to the system can be well explained by a simple surface complexation model, able to explain observed and calculated data in the literature.

The system tested by our experiments can be taken as a fairly good representation of the long-term situation in the repository, where a release of active Ni (in the real case ^{59}Ni) will contact an environment likely saturated with concentrations of stable Ni in the range 10^{-7} to 10^{-8} M.

4 Main conclusions of relevance for the Safety Assessment of the SFR repository

The outcomes of this thesis for the Safety Assessment of the SFR repository are the following:

- The predicted redox evolution of the near field of the repository due to the anaerobic corrosion of the steel components as documented in Duro et al. (2014) has been confirmed by the experimental data collected in the pH, Eh space of concern.
- In the presence of magnetite and Fe(II) the Eh values obtained in the pH range of interest (10–13) are in the order of −600 mV and the Fe(II) data in this range is well represented by the equilibrium solubility of Fe_3O_4(cr).
- The value of the solubility constant of magnetite derived in the present study from solubility experiments at $T = 22$ °C is significantly higher than values available in current thermodynamic databases, derived from high-temperature thermochemical studies and they should give a more realistic representation of the behaviour of magnetite under SFR conditions.
- The pH and Eh space imposed by the anaerobic corrosion of iron in the presence of cement controls the redox state and solubility of key radionuclides as U, Pu and Tc. The extent of the electron-transfer reactions and the resulting radionuclide solubility depends very much on the alkalinity of the system.
- In the presence of magnetite and under slightly alkaline conditions (pH around 8) most of the radionuclide concentrations are under 10^{-8} molar, except in the case of Pu. In this case the presence of Pu(III) enhances the concentration up to 10^{-6} molar.
- At the alkaline conditions expected in the cementitious repository, pH=12.8, only Pu concentrations are below 10^{-8} molar. Aqueous Tc(IV), although apparently reduced, is stabilised due to the formation of Tc(IV) anionic hydroxo species and the measured concentrations are in the 10^{-6} molar range. Uranium(VI) is not reduced by magnetite at pH=12.8 and the resulting concentrations are un the 10^{-5} molar range.
- All these observations would indicate that kinetics of these redox reactions would be relatively slow, particularly at higher pH values. As we already indicated in Bruno (1997) the characteristic reaction times for such multielectron transfer processes are in the range of 10 to 1000 years, which have to be compared to the expected groundwater residence times in the SFR repository which are in the range of thousands of years. Kinetic modelling is underway to pinpoint these important issues in order to quantification of these processes under SFR conditions.
- Concerning the speciation and mobility of Ni(II) under SFR conditions, these are the main PA implications:
  - The solubility constant for β-$Ni(OH)_2$(s) has been determined to be log Kso = 12.10 ± 0.11
  - The main hydrolysis equilibria have been established, the main hydrolysis species under SFR conditions is $Ni(OH)_2$(aq) with a formation constant log $\beta_{11} = -19.7 \pm 0.04$. There is no evidence for the formation of anionic hydroxo species up to pH=13.
  - Under the presence of ISA the following species and equilibrium constants have been determined.
    - Ni(OH)ISA (aq) with log $\beta_{111} = -6.5 \pm 0.3$
    - $Ni(OH)_2ISA^-$ with log $\beta_{121} = -17.6 \pm 0.5$
    - $Ni(OH)_3ISA^{2-}$ with log $\beta_{131} = -31.0 \pm 0.7$
- Concerning the sorption of Ni(II) in the presence of cement and ISA these are the main implications:
  - The sorption of ^{63}Ni onto the cement is clearly reduced in the presence of ISA, in spite of the fact that there is a sizeable amount of ^{58}Ni both in the cement and the contacting water.
  - There seems to be no kinetic effect of the order of addition of the various components: cement, Ni(II) and ISA on the $^*R_d$. Only at very high ISA levels (0.1 M) there seems to be some kinetic effect but the data are not sufficient to discern the extent.

- Detailed modelling work has resulted on a thermodynamic model to account for the effect of ISA on the sorption of ^{63}Ni onto cement. The dependence of the $^{*}R_d$ of ^{63}Ni onto cement in the presence of background amounts of ^{58}Ni and ISA has been calculated and the subsequent *SRF's have been established based upon the aqueous themodynamic model determined in this work. *SRF values range from 2 to 40 in the ISA concentration range: 10^{-3} to 10^{-1}.
- The speciation scheme of Ni(II) in the presence of ISA proposed in this work explains the decrease of the extent of sorption of Ni(II) onto cement and in the presence of ISA. Independent sorption data can also be reasonably explained by the present Ni(II)-ISA speciation scheme. This gives additional confidence on the results obtained.
- Although aqueous Ni in cement under repository conditions seems to be solubility, and not sorption limited, the behaviour of ^{63}Ni added to the system can be well explained by a simple surface complexation model, able to explain observed and calculated data in the literature.
- The system tested by our experiments can be taken as a fairly good representation of the long-term situation in the repository, where a release of active Ni (in the real case ^{59}Ni) will contact an environment likely saturated with concentrations of stable Ni in the range 10^{-7} to 10^{-8} M.
- Under the conditions of our experiments, a concentration of ISA of 0.02 M, as the maximum expected in the SFR repository would imply a *SRF(Ni) between 5 and 7.

5 Acknowledgements

A number of people have contributed in several aspects of this work, particularly at KIT-INE. These are: Thomas Rabung for sorption studies, David Fellhauer and Ezgi Yalcintas for studies on radionuclides, Tonya Vitova and Ivan Pidchenko for XAFS measurements and data evaluation, Dieter Schild for SEM-EDS and XPS measurements and data evaluation, Gopala Darbha for AFM measurements and data evaluation and Melanie Böttle, Frank Geyer, Markus Lagos and Cornelia Walschburger for analytical support. We are deeply grateful for their valuable contribution to this work. David García (Amphos[21]) identified a typo in the PhreeqC input files which was making the life of the sorption modeller impossible. He is deeply acknowledged.

References

SKB's (Svensk Kärnbränslehantering AB) publications can be found at www.skb.com/publications.

Almkvist L, Gordon A, 2007. Low and intermediate level waste in SFR 1. Reference waste inventory 2007. SKB R-07-17, Svensk Kärnbränslehantering AB.

Atkins M, Glasser F P, 1992. Application of Portland cement-based materials to radioactive waste immobilization. Waste Management 12, 105–131.

Atkins M, Glasser F P, Kindness A, 1992. Cement hydrate phase: solubility at 25 °C. Cement and Concrete Research 22, 241–246.

Baes C F, Mesmer R E, 1976. Hydrolysis of cations. New York: Wiley.

Bildstein K L, 2006. Migrating raptors of the world: their ecology & conservation. Ithaca, NY: Cornell University Press.

Bradbury M H, Van Loon L R, 1997. Cementitious near-field sorption data bases for performance assessment of a L/ILW repository in a Palfris host rock. PSI Bericht 98-01, CEM-94: Update I, Paul Scherrer Institut, Switzerland.

Brown P L, Ekberg C, 2016. Hydrolysis of metal ions. Berlin: Wiley-VCH.

Bruno J, 1997. Trace element modelling. In Grenthe I, Puigdomènech I (eds). Modelling in aquatic chemistry. Paris: OCDE/Nuclear Energy Agency, 593–621.

Chivot J, 2004. Thermodynamique des produits de corrosion: Fonctions thermodynamiques, diagrammes de solubilité, diagrammes E-pH des systèmes Fe-H_2O, Fe-CO_2-H_2O, Fe-S-H_2O, Cr-H_2O et Ni-H_2O en fonction de la température. Châtenay-Malabry, France: Andra. Available at: https://www.andra.fr/download/site-principal/document/editions/236.pdf (In French.)

Ciavatta L, 1980. The specific interaction theory in evaluating ionic equilibria. Annali di Chimica 70 , 551–562.

Colàs E, 2013. Complexation of Th(IV) and U(VI) by polyhydroxy and polyamino carboxylic acids. PhD thesis. Universitat Politècnica de Catalunya (UPC).

Cronstrand P, 2007. Modelling the long-time stability of the engineered barriers of SFR with respect to climate changes. SKB R-07-51, Svensk Kärnbränslehantering AB.

Duro L, Grivé M, Domènech C, Roman-Ross G, Bruno J, 2012. Assessment of the evolution of the redox conditions SFR1. SKB TR-12-12, Svensk Kärnbränslehantering AB.

Duro L, Domènech C, Grivé M, Roman-Ross G, Bruno J, Källström K, 2014. Assessment of the evolution of the redox conditions in a low and intermediate level nuclear waste repository (SFR1, Sweden). Applied Geochemistry 49, 192–205.

Ehrenfreund M, Leibenguth J L, 1970. Hydrolysis equilibriums of the ions of Fe(II) studied by ultraviolet and visible spectrophotometry. II. Study in 2 M ammonium sulfate or 2 M sodium perchlorate. Bulletin de la Société Chimique de France, 2498–2505.

Evans N, 2003. Studies on metal α-isosaccharinic acid complexes. PhD thesis. Loughborough University, United Kingdom.

Fanger G, Skagius K, Wiborgh M, 2001. Project SAFE. Complexing agents in SFR. Svensk Kärnbränslehantering AB.

Felipe-Sotelo M, Hinchliff J, Field L P, Milodowski A E, Holt J D, Taylor S E, Read D, 2016. The solubility of nickel and its migration through the cementitious backfill of a geological disposal facility for nuclear waste. Journal of Hazardous Materials 314, 211–219.

Gamsjäger H, Bugajski J, Gajda T, Lemire R J, Preis W, 2005. Chemical thermodynamics. Vol. 6. Chemical thermodynamics of nickel. Amsterdam: Elsevier.

Gayer K H, Woontner L, 1956. The solubility of ferrous hydroxide and ferric hydroxide in acidic and basic media at 25°. The Journal of Physical Chemistry 60, 1569–1571.

Giffaut E, Grivé M, Blanc P, Vieillard P, Colàs E, Gailhanou H, Gaboreau H, Gaboreau S, Marty N, Madé B, Duro L, 2014. Andra thermodynamic database for performance assessment: ThermoChimie. Applied Geochemistry 49, 225–236.

Glaus M A, Van Loon L R, 2008. Degradation of cellulose under alkaline conditions: new insights from a 12 years degradation study. Environmental Science & Technology 42, 2906–2911.

Glaus M A, Van Loon L R, Achatz S, Chodura A, Fischer K, 1999. Degradation of cellulosic materials under the alkaline conditions of acementitious repository for low and intermediate level radioactive waste Part I: Identification of degradation products. Analytica Chimica Acta 398, 111–122.

Glaus M A, Van Loon L R, Schwyn B, Vines S, Williams S J, Larsson P, Puigdomenech I, 2008. Long-term predictions of the concentration of a-isosaccharinic acid in cement pore water. In Lee W E (ed). Scientific basis for nuclear waste management XXXI: symposium held in Sheffield, United Kingdom, 16–21 September 2007. Warrendale, PA: Materials Research Society. (Materials Research Society Symposium Proceedings 1107).

González-Siso M R, Gaona X, Duro L, Almaier M, Bruno J, 2018. Thermodynamic model of Ni(II) solubility, hydrolysis and complex formation with ISA. Radiochimica Acta 106, 31–45.

Greenfield B J, Harrison W N, Robertson G P, Somers P J, Spindler M W, 1993. Mechanistic studies of the alkaline degradation of cellulose in cement. Harwell, United Kingdom: AEA Technology.

Grivé M, Duro L, Colàs E, Giffaut E, 2015. Thermoynamic data selection applied to radionuclides and chemotoxic elements: an overview of the ThermoChimie-TDB. Applied Geochemistry 55, 85–94.

Guillaumont R, Fanghänel J, Neck V, Fuger J, Palmer D A, Grenthe I, Rand M H, 2003. Chemical thermodynamics. Vol 5. Update on the chemical thermodynamics of uranium, neptunium, plutonium, americium and technetium. Amsterdam: Elsevier.

Hedström B O A, 1953. Studies on the hydrolysis of metal ions. VI. The hydrolysis of the iron(II) ion, Fe^{2+}. Arkiv för kemi 5,457–468.

Hietanen R, Kamarainen E-L, Alaluusua M, 1984. Sorption of strontium, caesium, nickel, iodine and carbon in concrete. Report YJT-84-04, Nuclear Waste Commission of Finnish Power Companies (YJT).

Holgersson S, Albinsson Y, Allard B, Boren H, Pavasars I, Engkvist I, 1998. Effects of Glucoisosaccharinate on Cs, Ni, Pm, and Th sorption onto, and diffusion into cement. Radiochimica Acta 82, 393–398.

Huber F, Schild D, Vitova T, Rothe J, Kirsch R, Schäfer T, 2012. U(VI) removal kinetics in presence of synthetic magnetite nanoparticles. Geochimica et Cosmochimica Acta 96 154–173.

Hummel W, 2009. Ionic strength corrections and estimation of SIT ion interaction coefficients. PSI Report TM-44-09-01, Paul Scherrer Institut, Switzerland.

Hummel W, Berner U, Curti E, Pearson F J, Thoenen T, 2002. Nagra/PSI chemical thermodynamic data base 01/01. Radiochimica Acta 90, 805–813.

Höglund L O, 2001. Project SAFE. Modelling of long-term concrete degradation processes in the Swedish SFR repository. SKB R-01-08, Svensk Kärnbränslehantering AB.

Ilton E S, Boily J-F, Buck E C., Skomurski F N, Rosso K M, Cahill C L, Bargar J R, Felmy A R, 2010. Influence of dynamical conditions on the reduction of U(VI) at the magnetite solution interface. Environmental Science & Technology 44, 170–176.

Johnson G K, Bauman J E, 1978. Equilibrium constants for the aquated iron(II) cation. Inorganic Chemistry 17, 2774–2779.

Kanert G A, Gray G W, Baldwin W G, 1976. The solubility of magnetite in basic solutions at elevated temperatures. AECL-5528, Atomic Energy of Canada Ltd.

Keith-Roach M, Lindgren M, Källström K, 2014. Assessment of complexing agent concentrations in SFR. SKB R-14-03, Svensk Kärnbränslehantering AB.

Kirsch R, Fellhauer D, Altmaier M, Neck V, Rossberg A, Fanghänel T, Scheinost T, 2011. Oxidation State and Local Structure of Plutonium Reacted with magnetite, mackinawite, and chukanovite. Environmental Science & Technology 45, 7267–7274.

Kobayashi T, Scheinost, A C, Fellhauer D, Gaona X, Altmaier M, 2013. Redox behavior of Tc(VII)/Tc(IV) under various reducing conditions in 0.1 M NaCl solutions.et al. Radiochimica Acta 101, 323–332.

Lagerblad B, Trägårdh J, 1994. Conceptual model for concrete long time degradation in a deep nuclear waste repository. SKB TR 95-21, Svensk Kärnbränslehantering AB.

Lemire R J, Berner U, Musikas C, Palmer D A, Taylor P, Tochiyama O, 2013. Chemical thermodynamics, Vol 13a. Chemical thermodynamics of iron, Part 1. Paris: OECD/Nuclear Energy Agency.

Lindgren M, Pettersson M, Wiborgh M, 2007. Correlation factors for C-14, Cl-36, Ni-59, Ni-63, Mo-93, Tc-99, I-129 and Cs-135 in operational waste for SFR1. Svensk Kärnbränslehantering AB.

Mesmer R E, 1971. Hydrolysis of iron(2+) in dilute chloride at 25°. Inorganic Chemistry 10, 857–858.

Neck V, Altmaier M, Seibert A, Yun J L, Marquardt C M, Fanghänel T, 2007. Solubility and redox reactions of Pu(IV) hydrous oxide: evidence for the formation of PuO_{2+x}(s, hyd). Radiochimica Acta 95, 193–207.

Ochs M, Hager D, Helfer S. Lothenbach B 1998. Solubility of radionuclides in fresh and leached cementitious systems at 22 °C and 50 °C. In McKinley I G, McCombie C (eds). Scientific basis for nuclear waste management XXI: symposium held in Davos, Switzerland, 23 September – 3 October 1997. Warrendale, PA: Materials Research Society. (Materials Research Society Symposium Proceedings 506), 773–780.

Ochs M, Colàs E, Grivé M, Olmeda J, Campos I, Bruno J, 2014. Reduction of radionuclide uptake in hydrated cement systems by organic complexing agents: Selection of reduction factors and speciation calculations. SKB R-14-22, Svensk Kärnbränslehantering AB.

Ochs M, Mallants D, Wang L, 2016. Radionuclide and metal sorption on cement and concrete. topics in safety, risk, reliability and quality. Springer International Publishing.

Palmer D A, Gamsjäger H, 2010. Solubility measurements of crystalline β-$Ni(OH)_2$ in aqueous solution as a function of temperature and pH. Journal of Coordination Chemistry 63, 2888–2908.

Palmer D A, Benezeth P, Wesolowski D J, Anovitz L M, Machesky M L, Hayashi K I, Hyde K E, 1997. Solubility of, and hydrogen ion adsorption on, some metal oxides in aqueous solutions to high temperatures. CONF-970623—1, Oak Ridge National Laboratory, Tennessee.

Palmer D A, Bénézeth P, Wesolowski D J, 2004. Solubility of nickel oxide and hydroxide in water. In Proceedings of the 14th International Conference on the Properties of Water and Steam, Kyoto, Japan, 29 August – 3 September 2004. Available at: http://www.iapws.jp/Proceedings/Symposium05/264Palmer.pdf

Palmer D A, Bénézeth P, Xiao C, Wesolowski D J, Anovitz L M, 2011. Solubility measurements of crystalline NiO in aqueous solution as a function of temperature and pH. Journal of Solution Chemistry 40, 680–702.

Pointeau I, Hainos D, Coreau N, Reiller P, 2006. Effect of organics on selenite uptake by cementitious materials. Waste Management 26, 733–740.

Pointeau I, Coreau N, Reiller P, 2008. Uptake of anionic radionuclides onto degraded cement pastes and competing effect of organic ligands. Radiochimica Acta 96, 367–374.

Schindler P W, 1967. Heterogeneous equilibria involving oxides, hydroxides, carbonates and hydroxide carbonates. In Stumm W (ed). Equilibrium concepts in natural water systems. Washington, DC: American Chemical Society. (Advances in Chemistry Series 67), 196–221.

Schwertmann U, Cornell R M, 2000. Iron oxides in the laboratory: preparation and characterization. Weinheim: Wiley-VCH.

Scheidegger A, Wieland E, Scheinost A C, Dahn R, Spieler P 2000. Spectroscopic evidence for the formation of layered ni-al double hydroxides in cement. Environmental Science & Technology 34, 4545–4548.

SKB, 2008. Safety analysis SFR 1. Long-term safety. SKB R-08-130, Svensk Kärnbränslehantering AB.

Smart N R, Blackwood D J, Werme L, 2001. The anaerobic corrosion of carbon steel and cast iron in artificial groundwaters. SKB TR-01-22, Svensk Kärnbränslehantering AB.

Sweeton F H, Baes C F, 1970. The solubility of magnetite and hydrolysis of ferrous ion in aqueous solutions at elevated temperatures. The Journal of Chemical Thermodynamics 2, 479–500.

Takashi M, Posey F A, 1967. Application of the electrochemical pH-stat to the study of the hydrolysis of metal ions. Denki Kagaku Oyobi Kogyo Butsuri Kagaku 35 (1967), 633–663, in Japanese, see also an extended abstract: Journal of the Electrochemical Society of Japan 35, (1967), 166 (in English).

Tasi A G, Gaona X, Fellhauer D, Böttle M, Rothe J, Dardenne K, Schild D, Grivé M, Colàs E, Bruno J, Källström K, Altmaier M, Geckeis H, 2018. Redox behavior and solubility of plutonium under alkaline, reducing conditions. Radiochimica Acta. doi.org/10.1515/ract-2017–2870

Thoenen T, Hummel W, Berner U, Curti E, 2014. The PSI/Nagra Chemical Thermodynamic Database 12/07. PSI Bericht 14-04, Paul Scherrer Institut, Switzerland.

Tremaine P R, LeBlanc J C, 1980. The solubility of magnetite and the hydrolysis and oxidation of Fe^{2+} in water to 300 °C. Journal of Solution Chemistry 9, 415–442.

Van Loon L R, Glaus M A, 1997. review of the kinetics of alkaline degradation of cellulose in view of its relevance for safety assessment of radioactive waste repositories. Journal of Environmental Polymer Degradation 5, 97–109.

Van Loon L R, Glaus M A, 1998. Experimental and theoretical studies on alkaline degradation of cellulose and its impact on the sorption of radionuclides. Nagra TR 97-04, Nagra, Switzerland.

Van Loon L R, Glaus M A, Stallone S, Laube A, 1997. Sorption of isosacchrinic acid, a cellullose degradation product, on cement. Environmental Science & Technology 31, 1243–1245.

Vercammen K, 2000. Complexation of calcium, thorium and europium by alpha-isosaccharinic acid under alkaline conditions. PhD thesis. Swiss Federal Institute of Technology, Zurich.

Wang L, Martens E, Jacques D, De Cannière P, Berry J, Mallants D 2009. Review of sorption values for the cementitious near field of a near surface radioactive waste disposal facility Project near surface disposal of category A waste at Dessel NIRAS-MP5-03 DATA-LT(NF) Version 1. NIROND-TR 2008-23 E April 2009.

Warwick P, Evans N, Hall T, Vines S, 2003. Complexation of Ni(II) by α-isosaccharinic acid and gluconic acid from pH 7 to pH 13. Radiochimica Acta 91, 233–240.

Whistler R, BeMiller J (eds), 1961. Methods in carbohydrate chemistry. Vol. 2, Reactions of carbohydrates. New York: Academic Press.

Wieland E, Van Loon D, 2003. Cementitious near-field sorption data base for performance assessment of an ILW repository in Opalinus clay. PSI Bericht 03-06, Paul Scherrer Institut, Switzerland.

Wieland E, Tits J, Spieler P, Dobler J-P, Scheidegger A M, 2000. Uptake of nickel and strontium by a sulphate-resisting Portland cement. In Rammlmair D, Mederer J, Oberthür T, Heimann R B, Pentinghaus H (eds). Applied mineralogy. Vol 2. Rotterdam: Balkema, 705–708.

Wieland E, Tits J Ulrich A, Bradbury M H, 2006. Experimental evidence for solubility limitation of the aqueous Ni(II) concentration and isotopic exchange of ^{63}Ni in cementitious systems. Radiochimica Acta 94, 29–36.

Yalçıntaş E, Gaona X, Scheinost A, Kobayashi T, Altmaier M, Geckeis H, 2015. Redox chemistry of Tc(VII)/Tc(IV) in dilute to concentrate NaCl and $MgCl_2$ solutions. Radiochimica Acta 103, 57–72.

Yalçıntaş E, Gaona X, Altmaier M, Dardenne K, Polly R, Geckeis H, 2016. Thermodynamic description of Tc(IV) solubility and hydrolysis in dilute to concentrated NaCl, $MgCl_2$ and $CaCl_2$ solutions. Dalton Transactions, 45, 8916–8936.

Ziemniak S E, Jones M E, Combs K E S, 1995. Magnetite solubility and phase stability in alkaline media at elevated temperatures. Journal of Solution Chemistry 24, 837–877.

Appendix 1

Characterization of magnetite

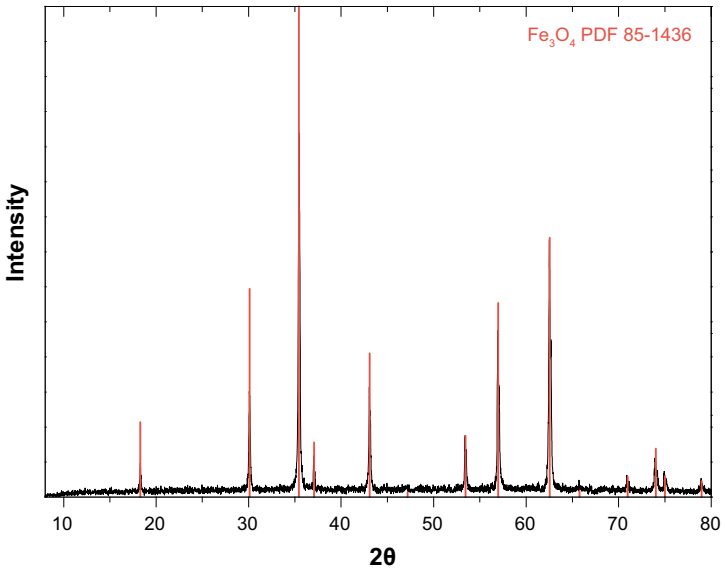

Figure A1-1. *XRD diffractogram of crystalline Fe_3O_4 (initial material) used in the present work. Ref: PDF 85-1436 Acta Crystallogr sec B volume 38, page 1718 (1982) Fleet, M.E.*

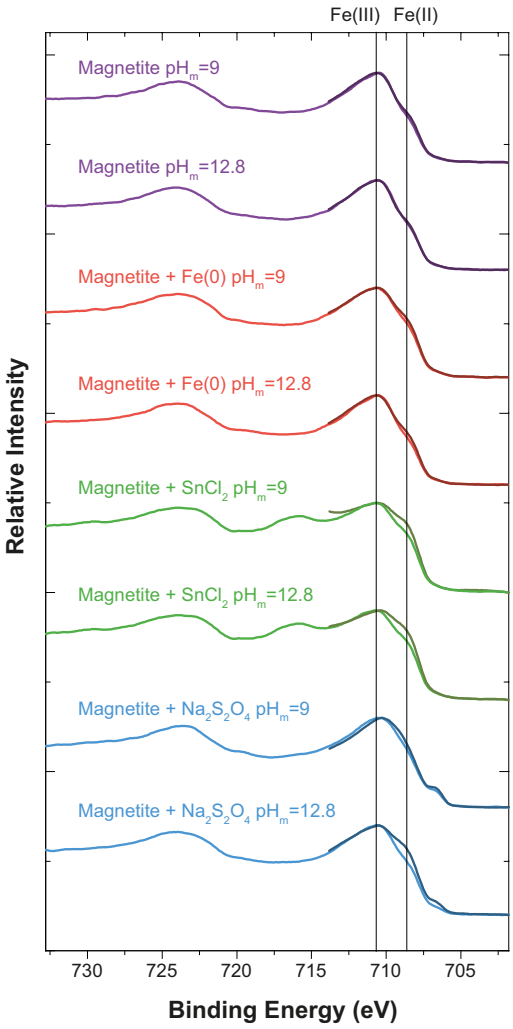

Figure A1-2. *XPS spectra for the magnetite systems investigated in this study.*

Table A1-1. Fraction of Fe(II) in magnetite determined by XPS in Fe_3O_4(cr), Fe_3O_4(cr) + Fe(0), Fe_3O_4(cr) + Sn(II) and Fe_3O_4(cr) + $Na_2S_2O_4$ systems.

	Fe(II)/Fe_{tot}			
	Fe_3O_4	Fe_3O_4 + Fe(0)	Fe_3O_4 + $SnCl_2$	Fe_3O_4 + $Na_2S_2O_4$
Initial Material	29±3 %	29±3 %	29±3 %	29±3 %
pH=9	28±3 %	32±3 % *Traces Fe(0)*	35±3 %	35±3 %
pH=12.5	28±3 %	28±3 %	34±3 % *Traces Fe(0)*	36±3 % *Traces Fe(0)*

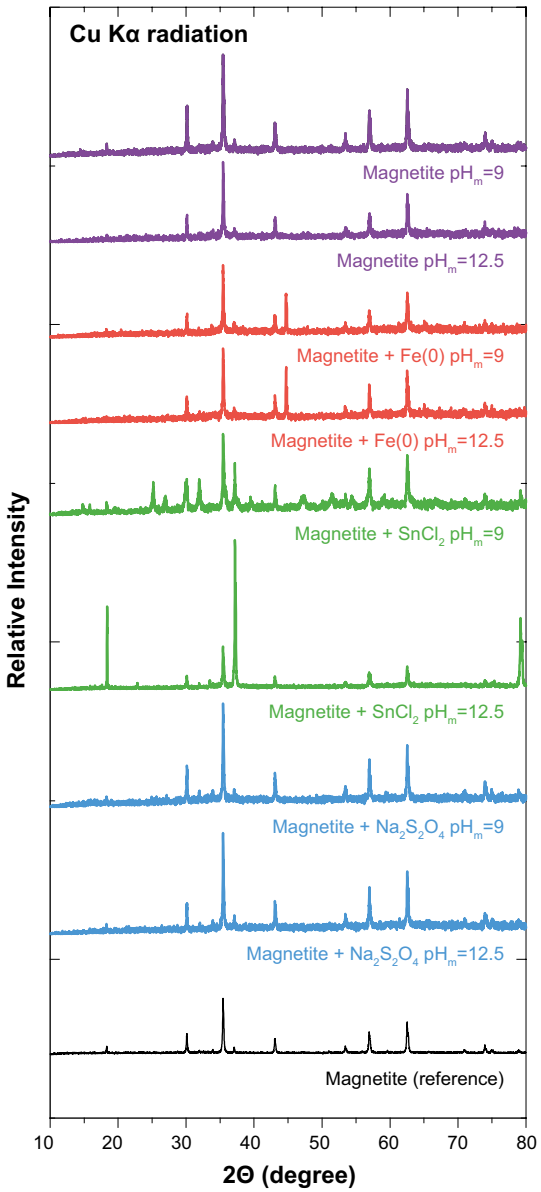

Figure A1-3. *XRD of selected solid phases from solubility experiments in 0.1 M NaCl-NaOH background solutions at pH 9 and 12.5. Purple indicates Pure magnetite, red for Magnetite + Fe(0), green in case of Magnetite + Sn(II) and finally blue for Magnetite + Na2S2O4. In black, reference spectra of Magnetite (PDF 85-1436).*

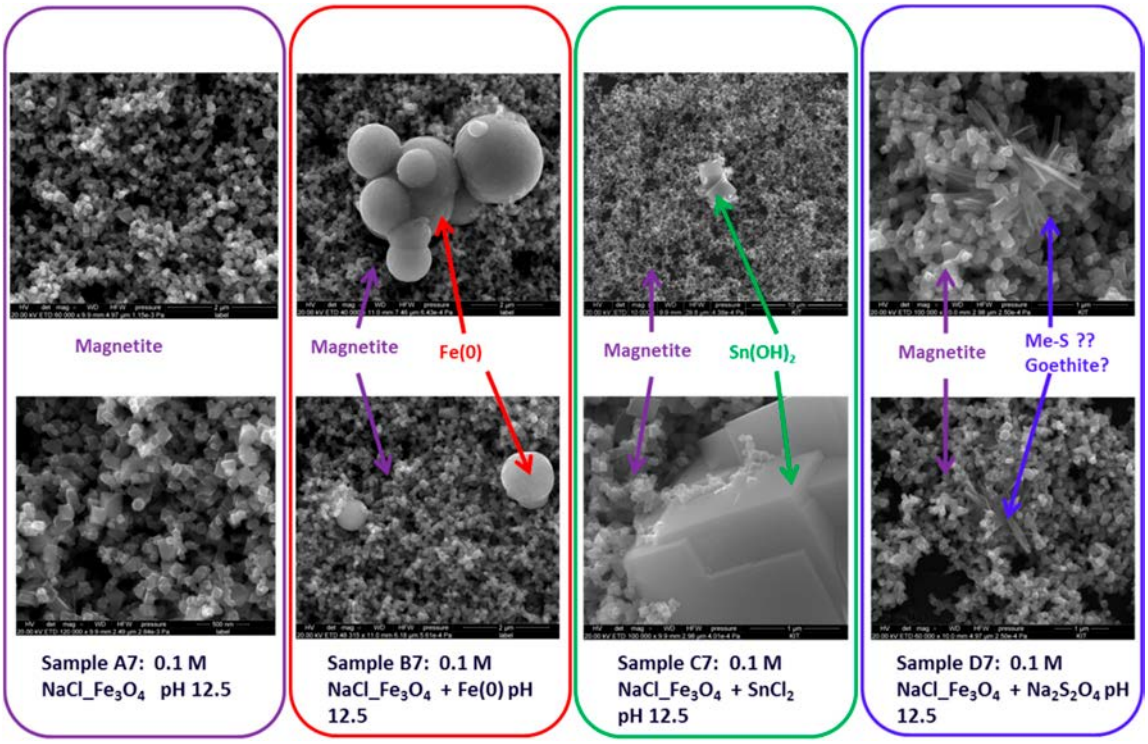

Figure A1-4. *SEM images of selected solid phases from solubility experiments in 0.1 M NaCl-NaOH background solutions at pH 12.5. Purple indicates Pure magnetite, red for Magnetite + Fe(0), green in case of Magnetite + Sn(II) and finally blue for Magnetite + $Na_2S_2O_4$.*

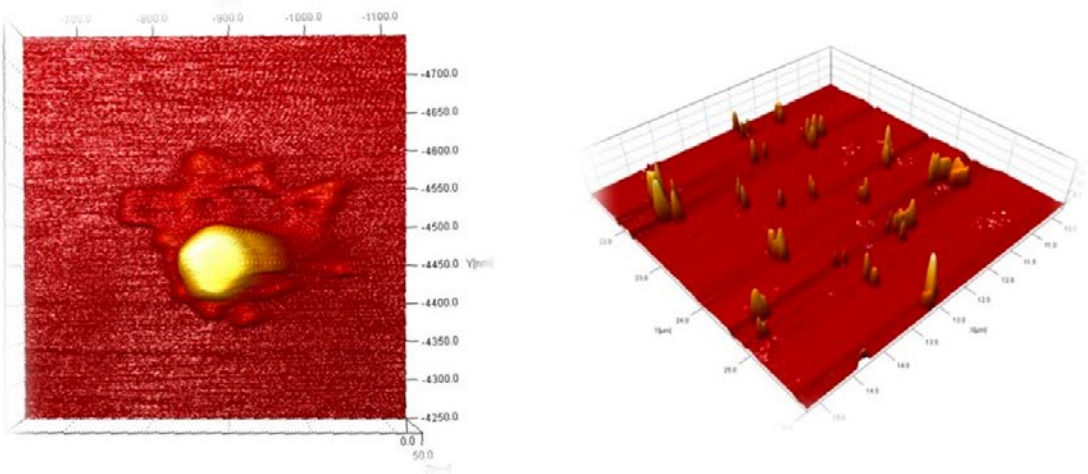

Figure A1-5. *AFM images of selected solid phases from solubility experiments in 0.1 M NaCl-NaOH background solutions at pH 12.5.*

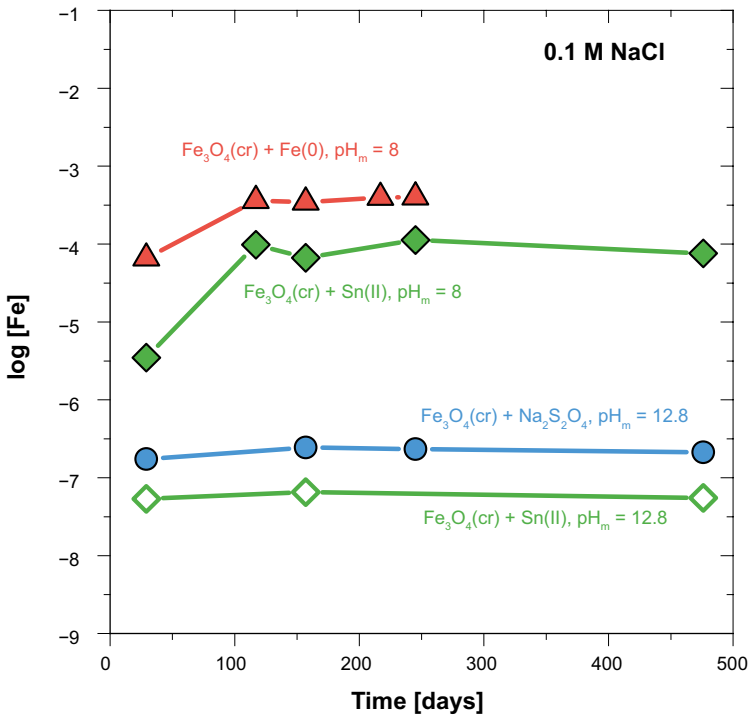

Figure A1-6. *Kinetics of the solubility equilibrium of magnetite in selected Fe(0), Sn(II) and $Na_2S_2O_4$ systems.*

Appendix 2

Solid state characterization

A2.1 Solid phase characterization in the Tc-Fe system

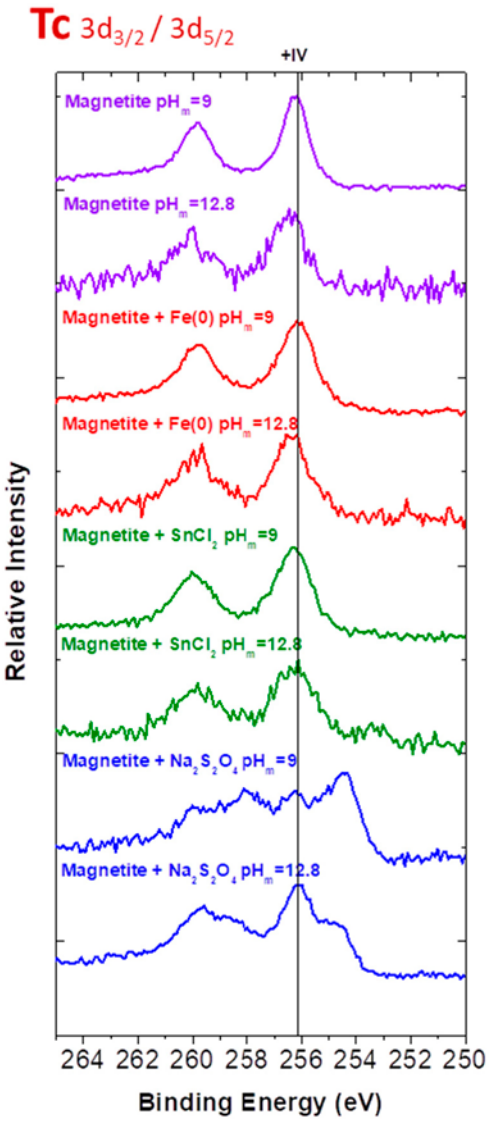

Figure A2-1. *XPS spectra for the Tc 3d3/2 / 3d5/2 transitions in Fe_3O_4(cr), Fe_3O_4(cr) + Fe(0), Fe_3O_4(cr) + Sn(II) and Fe_3O_4(cr) + $Na_2S_2O_4$ systems at pHm ≈ 9 and pHm = 12.8.*

Table A2-1. Tc redox states identified in Fe_3O_4(cr), Fe_3O_4(cr) + Fe(0), Fe_3O_4(cr) + Sn(II) and Fe_3O_4(cr) + $Na_2S_2O_4$ systems by XPS. The second peak at lowest binding energies observed in the presence of $Na_2S_2O_4$ is assigned to Tc(IV)-S interactions.

	Magnetite + Tc			
	Fe_3O_4	Fe_3O_4 + Fe(0)	Fe_3O_4 + $SnCl_2$	Fe_3O_4 + $Na_2S_2O_4$
pH=9	Tc(IV)	Tc(IV)	Tc(IV)	Tc(IV)
pH=12.8	Tc(IV)	Tc(IV)	Tc(IV)	Tc(IV)

A2.2 Solid phase characterization in the U-Fe system

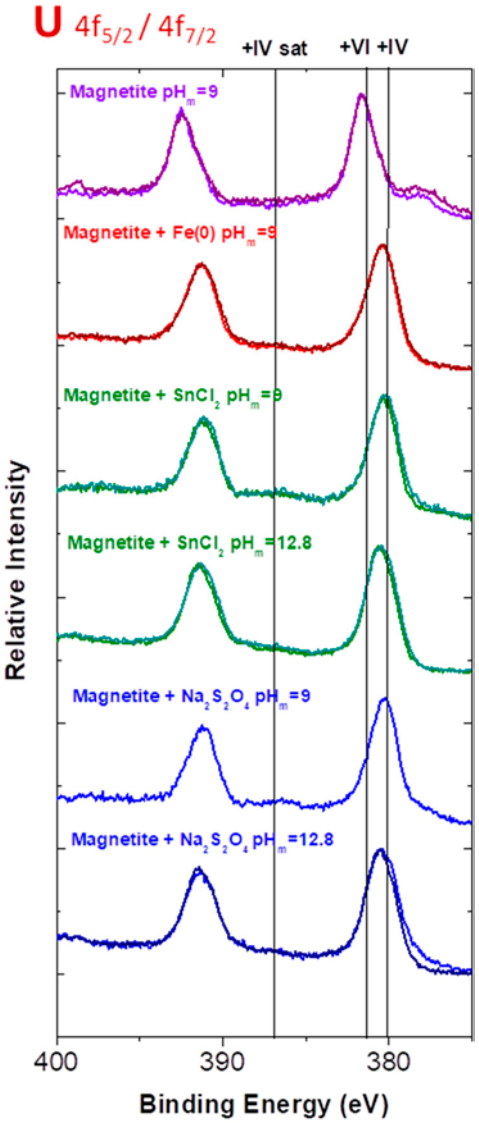

Figure A2-2. *XPS spectra for the U 4f5/2 / 4f7/2 transitions in Fe_3O_4(cr), Fe_3O_4(cr) + Fe(0), Fe_3O_4(cr) + Sn(II) and Fe_3O_4(cr) + $Na_2S_2O_4$ systems at pHm ≈ 9 and pHm = 12.8.*

Table A2-2. U redox states identified in Fe_3O_4(cr), Fe_3O_4(cr) + Fe(0), Fe_3O_4(cr) + Sn(II) and Fe_3O_4(cr) + $Na_2S_2O_4$ systems by XPS.

	Magnetite + U			
	Fe_3O_4	**Fe_3O_4 + Fe(0)**	**Fe_3O_4 + $SnCl_2$**	**Fe_3O_4 + $Na_2S_2O_4$**
pH=9	U(V)/(VI)	U(IV)	U(IV)	U(IV)
pH= 12.8	n.d.	n.d.	U (IV)	U(IV)

A2.3 Solid phase characterization in the Pu-Fe system

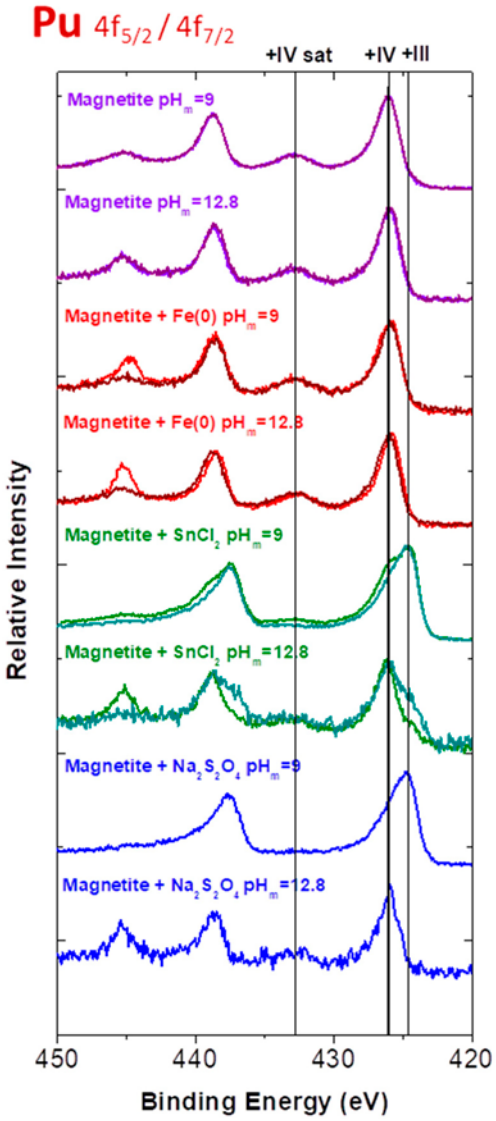

Figure A2-3. *XPS spectra for the U $4f_{5/2}$ / $4f_{7/2}$ transitions in Fe_3O_4(cr), Fe_3O_4(cr) + Fe(0), Fe_3O_4(cr) + Sn(II) and Fe_3O_4(cr) + $Na_2S_2O_4$ systems at $pH_m \approx 9$ and $pH_m = 12.8$.*

Table A2-3. Pu redox states identified in Fe_3O_4(cr), Fe_3O_4(cr) + Fe(0), Fe_3O_4(cr) + Sn(II) and Fe_3O_4(cr) + $Na_2S_2O_4$ systems by XPS.

	Magnetite + Pu			
	Fe_3O_4	Fe_3O_4 + Fe(0)	Fe_3O_4 + $SnCl_2$	Fe_3O_4 + $Na_2S_2O_4$
pH=9	Pu(IV)	Pu(IV)	Pu(IV)/(III)	Pu(IV)/(III)
pH= 12.8	Pu(IV)	Pu(IV)	Pu(IV)/(III)	Pu(IV)

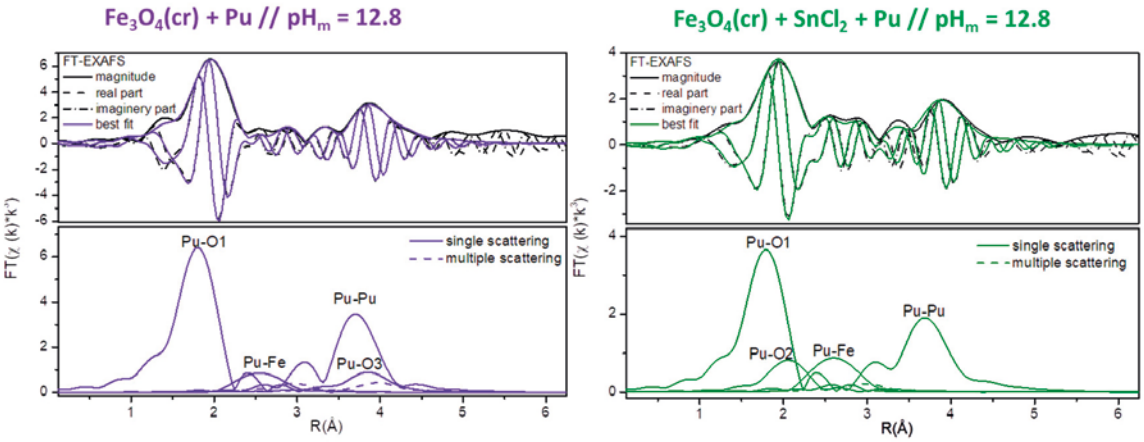

Figure A2-4. *Pu L_{III} EXAFS for solid samples in Fe_3O_4(cr) + Sn(II) and Fe_3O_4(cr) + $Na_2S_2O_4$ systems at pH_m = 12.8. The shorter backscattering distance in Pu-O_1 corresponds to Pu(IV), whereas the longer distance in Pu-O_2 corresponds to Pu(III).*

Appendix 3

Synthesis of ISA

A3.1 Synthesis and characterization of NaISA(s)

The calcium salt of isosaccharinic acid was synthetized following the procedure reported by Whistler and BeMiller (Whistler and BeMiller 1961)with some modifications from Vercammen and Evans (Vercammen 2000, Evans 2003). In a first step, α-lactose hydrate was contacted with an aqueous solution saturated with $Ca(OH)_2(s)$, and the mixture stirred during 3 days at room temperature in an inert gas (Ar) glovebox. The resulting suspension was heated for 10 hours and filtered whilst hot. A final volume reduction was performed in a rotary evaporator, and the mixture was left overnight at $T = 9$ °C. The resulting white crystals ($Ca(ISA)_2(s)$) were removed by filtration and washed with cold water, ethanol and acetone.

$Ca(ISA)_2(s)$ was converted into NaISA(s) using a cation exchange resin in the Na-form. An accurate description of the method is reported by Greenfield, Glaus, Pointeau and Colàs, among others (Greenfield et al. 1993, Pointeau et al. 2006, Glaus et al. 2008, Colàs 2013). Briefly, 2 g of $Ca(ISA)_2(s)$ were suspended in 500 mL of Milli-Q water in the presence of 25 g of resin. The mixture was agitated with a magnetic stirrer for approximately 1 hour, and then filtered with filter paper (Whatman blue ribbon, < 2 μm). The filtrate was evaporated on a heating plate at $T = 60$ °C until a brown viscous liquid was obtained. The remaining water content was removed using water-free diethyl-ether. The combination of repeated addition/evaporation of diethyl ether with a cooling step ($T = 9$ °C, laboratory fridge) resulted in a pale yellow solid phase, NaISA(s).

Both $Ca(ISA)_2(s)$ and NaISA(s) were characterized using XRD (X-ray diffraction), (solution) ^{1}H and ^{13}C NMR (nuclear magnetic resonance), quantitative chemical analysis and TOC (total organic content). XRD measurements were performed using a D8 Advance diffractometer (Bruker AXS) equipped with a Cu radiation tube. The resulting diffractograms were compared with data reported in the literature for $Ca(ISA)_2(cr)$, and confirmed the only presence of the Ca-salt of ISA [42]. Appropriate amounts of $Ca(ISA)_2(s)$ and NaISA(s) were dissolved in weakly alkaline solutions (pH ≈ 9) and the resulting solutions characterized using ^{1}H and ^{13}C NMR. NMR spectra of these samples were recorded at $T = 300$ K on a Bruker Avance III 400 spectrometer. The results confirm that ISA is the main organic component in both $Ca(ISA)_2(s)$ and NaISA(s) (> 95 %).

Ratios of Ca:ISA and Na:ISA in $Ca(ISA)_2(s)$ and NaISA(s) synthesized in the present work were quantified by a combination of quantitative chemical analysis and TOC measurements. Appropriate amounts of both solid phases were dissolved in water, and [Na] and [Ca] were quantified by ICP–OES (Optima 8300 DV, Perkin Elmer) and ICP–MS (X-Series II, Thermo Scientific), respectively. Aliquots of the same samples were also investigated by TOC using a Shimadzu TOC5000 equipment. The combination of these data resulted in Ca:ISA and Na:ISA ratios of 1:2 and 1:1, respectively, confirming the successful synthesis of the targeted $Ca(ISA)_2(s)$ and NaISA(s) compounds.

A3.2 Solid phase characterization of Ni(OH)2(s)

XRD analyses of the solid phase used in the present study confirm the only presence of $Ni(OH)_2(s)$ as a solid phase controlling the solubility of Ni(II) (Figure A3-1). XRD patterns before and after solubility experiments are identical, and show a good match with the reference spectra of β-$Ni(OH)_2(cr)$ (PDF 73-1520). Reflections of NaCl can be also observed in the solid phases recovered from solubility experiments in 3.0 M NaCl. This results from the insufficient removal of adhering matrix solution in concentrated NaCl solutions. In spite of this, XRD patterns corresponding to β-$Ni(OH)_2(cr)$ can be unequivocally identified for these systems. Note that XRD patterns collected in the present work are virtually the same as those reported in Palmer and Gamsjäger (2010), for β-$Ni(OH)_2(cr)$, although notably narrower peak widths were observed by the latter authors. This observation indicates a more crystalline material than the one used in the present work.

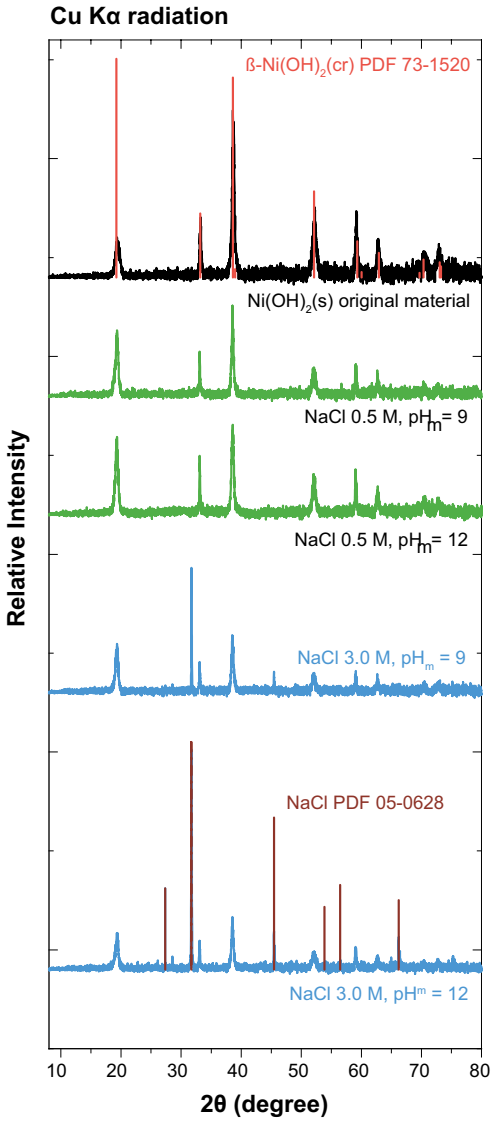

Figure A3-1. *XRD spectra of selected solid phases from Ni(II) solubility experiments in 0.5 and 3.0 M NaCl. Red and brown marks indicate peak positions for β-$Ni(OH)_2$(cr) and NaCl reference spectra (PDF 73-1520 and PDF 05-0628, respectively).*

A3.3 Solid phase characterization

The comparison of the XRD data collected for solubility experiments in the absence and presence of ISA shows that no solid phase alteration took place in the course of the experiments with ISA (Figure A3-2). The collected XRD patterns perfectly match those of β-$Ni(OH)_2$(cr) (PDF 73-1520), and thus the latter solid phase is considered to control the solubility of Ni(II) in the thermodynamic interpretation summarized in the following section.

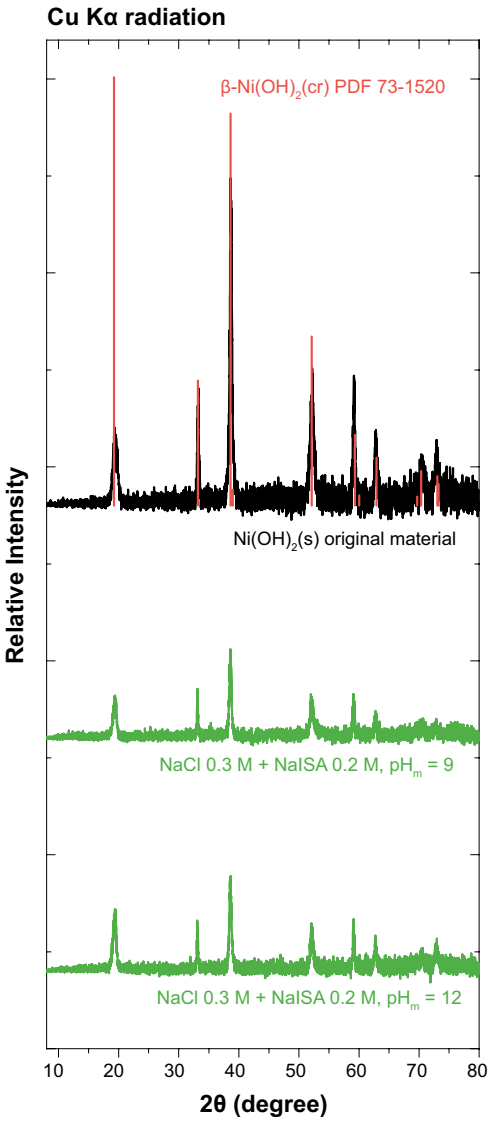

Figure A3-2. *XRD spectra of selected solid phases from Ni(II) solubility experiments in 0.5 M NaCl–NaISA in the absence and presence of NaISA (0.2 M). Red marks indicate peak positions for β-$Ni(OH)_2$(cr) reference spectrum (PDF 73-1520).*

A3.4 Comparison with data available in the literature

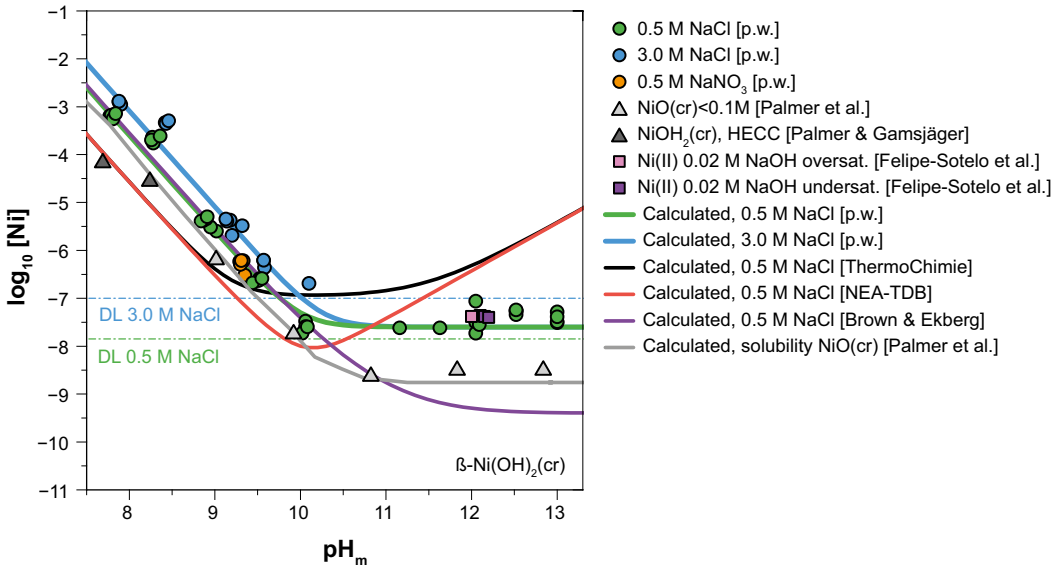

Figure A3-3. *Comparison of solubility data obtained in the present work for β-Ni(OH)$_2$(cr) with Ni(II) solubility data reported in Palmer et al. (2004, 2011) Palmer and Gamsjäger (2010) and Felipe-Sotelo et al. (2016).*

A3.5 The XRD diffractogram confirmed the predominance of portlandite

XRD analyses of the solid phase used in the present study confirm the presence of $Ca(OH)_2$ Portlandite.

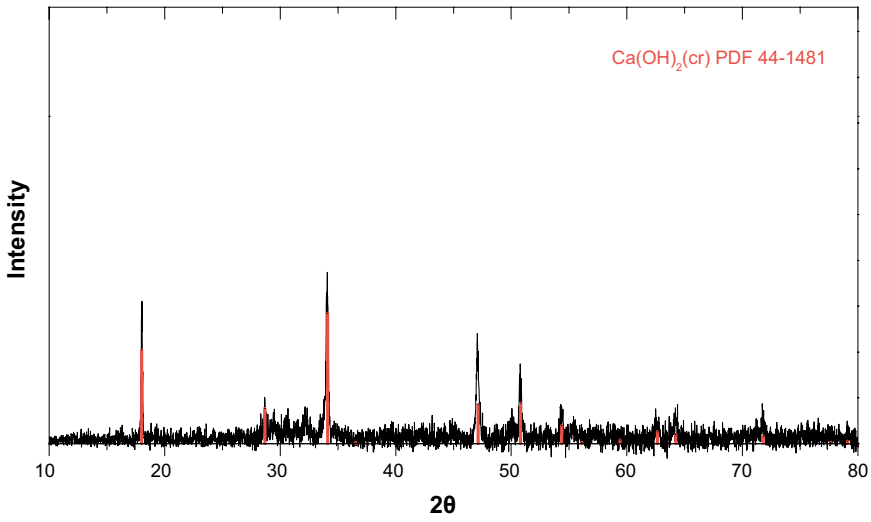

Figure A3-4. *XRD spectra of the solid phase used in the present study confirm the presence of $Ca(OH)_2$ Portlandite. Reference spectra of $Ca(OH)_2$(cr) (PDF 44-1481).*

Appendix 4

^{63}Ni sorption results

Table A4-1. Conditions and results of the sorption experiments. A: ^{63}Ni is preequilibrated with cement prior to ISA addition; B: ISA is preequilibrated with cement prior to ^{63}Ni addition; C: ^{63}Ni and ISA are preequilibrated for 2 days before contacting cement.

Experiment	[ISA]0 mol/L	[^{63}Ni]0 mol/L	Contact t (days)	[^{63}Ni]aq mol/L	*R_d (adim.)	[Ni]aq mol/L
Blank	0	2.83E-10	3	5.44E-12	51.00	1.37E-07
Blank	0	2.83E-10	87	1.07E-11	25.50	1.45E-07
Blank	0	2.83E-10	121	5.74E-12	48.31	1.45E-07
A	0.004	2.83E-10	2	2.67E-11	9.62	1.55E-07
A	0.004	2.83E-10	21	8.39E-12	32.74	1.46E-07
A	0.004	2.83E-10	87	1.35E-11	19.97	1.63E-07
A	0.004	2.83E-10	118	1.06E-11	25.75	1.42E-07
A	0.02	2.83E-10	2	1.79E-11	14.83	1.64E-07
A	0.02	2.83E-10	21	3.90E-11	6.26	2.23E-07
A	0.02	2.83E-10	87	1.01E-11	26.91	1.67E-07
A	0.02	2.83E-10	118	3.25E-11	7.70	1.38E-07
A	0.1	2.83E-10	2	3.43E-11	7.25	1.70E-07
A	0.1	2.83E-10	21	2.78E-11	9.17	1.67E-07
A	0.1	2.83E-10	87	3.48E-11	7.14	1.60E-07
A	0.1	2.83E-10	118	2.09E-11	12.52	1.55E-07
B	0.004	2.83E-10	3	1.26E-11	21.48	1.38E-07
B	0.004	2.83E-10	21	2.41E-11	10.74	1.67E-07
B	0.004	2.83E-10	87	1.79E-11	14.83	1.45E-07
B	0.004	2.83E-10	118	1.19E-11	22.81	1.38E-07
B	0.02	2.83E-10	3	6.67E-11	3.24	1.67E-07
B	0.02	2.83E-10	21	2.80E-11	9.11	1.90E-07
B	0.02	2.83E-10	87	3.23E-11	7.75	1.67E-07
B	0.02	2.83E-10	118	3.83E-11	6.39	1.91E-07
B	0.1	2.83E-10	3	1.36E-10	1.09	1.76E-07
B	0.1	2.83E-10	21	1.26E-10	1.25	1.80E-07
B	0.1	2.83E-10	87	1.24E-10	1.28	2.57E-07
B	0.1	2.83E-10	121	1.75E-10	0.61	1.59E-07
C	0.004	2.83E-10	3	1.26E-11	21.42	1.37E-07
C	0.004	2.83E-10	21	5.85E-12	47.36	1.42E-07
C	0.004	2.83E-10	87	1.15E-11	23.51	1.57E-07
C	0.004	2.83E-10	118	6.23E-12	44.46	n.d.
C	0.02	2.83E-10	3	3.51E-11	7.07	1.59E-07
C	0.02	2.83E-10	21	3.70E-11	6.66	1.66E-07
C	0.02	2.83E-10	87	3.68E-11	6.69	1.83E-07
C	0.02	2.83E-10	121	2.36E-11	11.01	1.45E-07

Table A4-2. Conditions and results of the ISA sorption experiments (no ^{63}Ni added). For the sake of completeness, the concentration of stable nickel in solution is also given. (n.d.: not determined).

Experiment	[ISA]0 mol/L	Contact t (days)	[ISA]aq mol/L	R_d(ISA)	[Ni]aq mol/L
ISA	0.004	3	0.0016	1.466	n.d.
ISA	0.004	21	0.0015	1.702	2.09E-07
ISA	0.004	87	0.0011	2.660	2.15E-07
ISA	0.004	119	0.0011	2.655	2.25E-07
ISA	0.02	3	0.0128	0.568	2.36E-07
ISA	0.02	21	0.0121	0.647	2.16E-07
ISA	0.02	87	0.0115	0.732	2.46E-07
ISA	0.02	119	0.0133	0.509	2.29E-07
ISA	0.1	3	0.0548	0.825	2.25E-07
ISA	0.1	21		n.d.	n.d.
ISA	0.1	87	0.0293	2.409	2.04E-07
ISA	0.1	119	0.0319	2.131	n.d.

Appendix 5

Snapshot of fractions of the Phreeqc inputs used in the simulations of ISA and ^{63}Ni sorption

Model II. Pointeau with portlandite

```
SELECTED_OUTPUT
   -file              ISA-sorp-pointeau-simple.sel
   -totals            Ca  Isa  Ni Z_sOH
   -molalities        Ni(OH)(HIsa)  Ni(OH)2(HIsa)-  Ca+2 Ni(OH)3(HIsa)-2  Z_sOH Z_sO- Z_sOCa+ Z_sOCaHIsa
Z_sHIsa
   -saturation_indices  Ca(HIsa)2(cr)  Portlandite
SURFACE_MASTER_SPECIES
   Z_s         Z_sOH
SURFACE_SPECIES
Z_sOH = Z_sOH
log_k 0.0
Z_sOH + Ca+2 + HIsa- = Z_sOCaHIsa + H+
log_k -7.5  #according to Pointeau et al., (2008)
END
SOLUTION 1
   temp      25
   pH       12.5
   pe       4
   redox     pe
   units     mol/kgw
   density   1
   #Ni       3e-07 Ni(OH)2(s)
Ca 7e-4  Portlandite
   ISA     0.004
   -water    1 # kg

SURFACE 1
   Z_sOH     0.01     79.2     25 #sites optimized with measured BET
EQUILIBRIUM_PHASES 1
Portlandite 0.0  10
Ca(HIsa)2(cr)  0.0  0

END
```

Model III. SCM with portlandite

```
SELECTED_OUTPUT
   -file              ISA-sorp2.sel
   -totals             Ca  Isa  Ni Z_sOH
   -molalities         Ni(OH)(HIsa) Ni(OH)2(HIsa)-  Ni(OH)3(HIsa)-2 Z_sOHHIsa- Z_sOH
   -saturation_indices  Ca(HIsa)2(cr)  Portlandite
SURFACE_MASTER_SPECIES
   Z_s         Z_sOH
SURFACE_SPECIES
Z_sOH = Z_sOH
log_k 0.0

Z_sOH + HIsa-=Z_sOHHIsa-
   log_k    5.0 #K optimized with measured BET and Langmuir sites
END
SOLUTION 1
   temp     25
   pH       12.5
   pe       4
   redox    pe
   units    mol/kgw
   density  1
   #Ni      3e-07 Ni(OH)2(s)
Ca 7e-4  Portlandite
   ISA     0.004
   -water   1 # kg

SURFACE 1
   Z_sOH     0.01     79.2     25 #optimized with measured BET
EQUILIBRIUM_PHASES 1
Portlandite 0.0 10
Ca(HIsa)2(cr)  0.0  0

END
```

Model A21, incorporating sorption of ISA and of 63Ni. Note that the equilibrium reaction notations have been simplified

```
SELECTED_OUTPUT
  -file             ISA-Ni-sorp.sel
  -totals            Ca  Isa  Ni Z_sOH
  -molalities        Ni(OH)(Isa)  Ni(OH)2(Isa)-  Ni(OH)3(Isa)-2 Z_sOHIsa- Z_sOH
  -saturation_indices  Ca(Isa)2(cr)  Portlandite
SURFACE_MASTER_SPECIES
  Z_s        Z_sOH
SURFACE_SPECIES
Z_sOH = Z_sOH
log_k 0.0

Z_sOH + Isa-= Z_sOHIsa-
  log_k    5.0 #K optimizada con BET real y sites 0.01  mol/L don

Z_sOH + Ni(OH)2 = Z_sOHNi(OH)2
                  log_k   3.6
END
SOLUTION 24
  temp     25
  pH       12.5
  pe       4
  redox    pe
  units    mol/kgw
  density  1
  Ni       2.8e-10
Ca 7e-4  Portlandite
  ISA      0.00001
  -water   1 # kg

SURFACE 24
  Z_sOH     0.01     79.2     25 #Los sites están optimizados con BET real y log_k 5.0
EQUILIBRIUM_PHASES 24
Portlandite 0.0  10
Ca(Isa)2(cr)  0.0  0

END
```

Arkitektkopia AB, Bromma, 2018

SKB is responsible for managing spent nuclear fuel and radioactive waste produced by the Swedish nuclear power plants such that man and the environment are protected in the near and distant future.

skb.se